MAX-PLANCK-INSTITUT
FÜR METEOROLOGIE

Boundary Layer Wind Balances and their Influence on Equatorial Sea Surface Temperatures

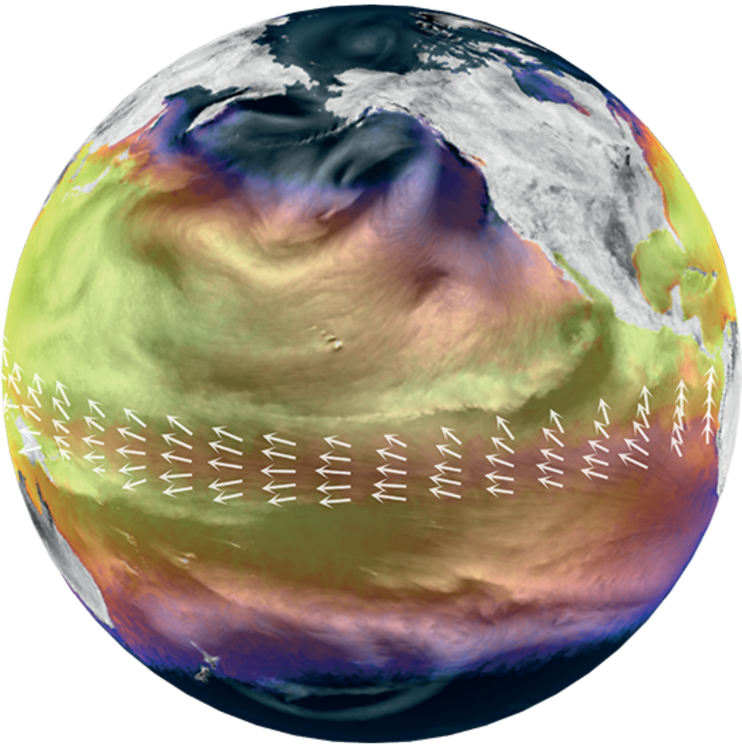

Marius Winkler

Hamburg 2025

Berichte zur Erdsystemforschung
Reports on Earth System Science

288
2025

Hinweis

Die Berichte zur Erdsystemforschung werden vom Max-Planck-Institut für Meteorologie in Hamburg in unregelmäßiger Abfolge herausgegeben.

Sie enthalten wissenschaftliche und technische Beiträge, inklusive Dissertationen.

Die Beiträge geben nicht notwendigerweise die Auffassung des Instituts wieder.

Die "Berichte zur Erdsystemforschung" führen die vorherigen Reihen "Reports" und "Examensarbeiten" weiter.

Notice

The Reports on Earth System Science are published by the Max Planck Institute for Meteorology in Hamburg. They appear in irregular intervals.

They contain scientific and technical contributions, including PhD theses.

The Reports do not necessarily reflect the opinion of the Institute.

The "Reports on Earth System Science" continue the former "Reports" and "Examensarbeiten" of the Max Planck Institute.

Anschrift / Address

Max-Planck-Institut für Meteorologie
Bundesstrasse 53
20146 Hamburg
Deutschland

Tel./Phone: +49 (0)40 4 11 73 - 0
Fax: +49 (0)40 4 11 73 - 298

name.surname@mpimet.mpg.de
www.mpimet.mpg.de

Layout

Bettina Diallo and Norbert P. Noreiks
Communication

Copyright

Boundary Layer Wind Balances
and their Influence
on Equatorial Sea Surface Temperatures

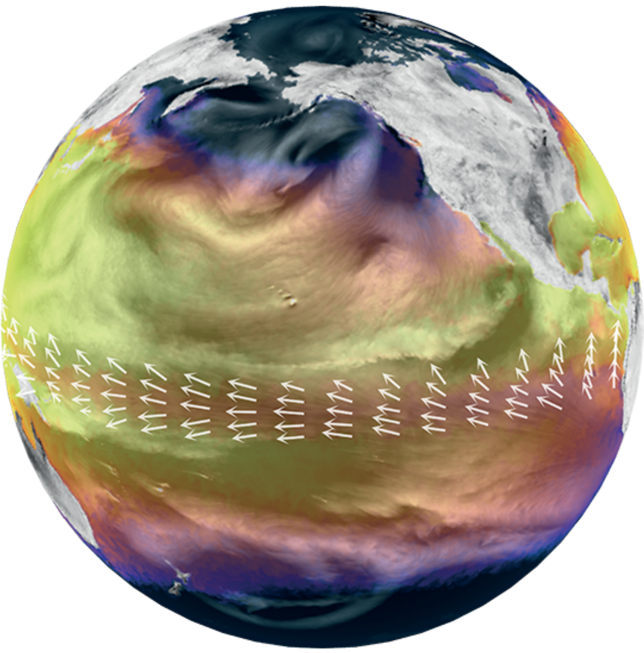

Marius Winkler

Hamburg 2025

Marius Winkler
aus Freiburg im Breisgau, Deutschland

Max-Planck-Institut für Meteorologie
The International Max Planck Research School on Earth System Modelling (IMPRS-ESM)
Bundesstrasse 53
20146 Hamburg

Tag der Disputation: 14. Februar 2025
Folgende Gutachter empfehlen die Annahme der Dissertation:
Prof. Dr. Bjorn Stevens
Prof. Dr. Juan Pedro Mellado

Vorsitzender des Promotionsausschusses:
Prof. Dr. Hermann Held

Dekan der MIN-Fakultät:
Prof. Dr.-Ing. Norbert Ritter

Titelgrafik: *Surface winds (frosting of the earth or gray shading) interact dynamically with the Earth's surface—over land, they reveal orographic features, while over the ocean, they actively shape ocean dynamics. Sea surface temperature (color-coded) reaches a local minimum in the equatorial cold tongue regions, a signature of air-sea interaction. Credit by the author*

Berichte zur Erdsystemforschung / Max-Planck-Institut für Meteorologie 288
Reports on Earth System Science / Max Planck Institute for Meteorology 2025

ISSN 1614-1199 - doi: 10.17617/2.3639124

Abstract

Boundary Layer Wind Balances and their Influence on Equatorial Sea Surface Temperatures

by Marius Winkler

Equatorial boundary layer winds over the ocean: why should we care? Ocean surface winds sit at the nexus of oceanic and atmospheric processes and drive air-sea interaction. They extract vast heat reserves from the equatorial ocean, mix them into the air, and fuel atmospheric dynamics, influencing surface temperatures, humidity profiles, and boundary layer stability. Understanding boundary layer winds is key to uncovering air-sea interaction in tropical regions.

Although SST-driven pressure gradients are known to set the equatorial boundary layer wind direction, a thorough quantification of the boundary layer momentum defining wind velocity and direction remains lacking. Climate models poorly represent air-sea interaction in low wind regimes, relying on simplified parameterizations and struggling to sustain surface pressure distributions. The complex interplay between momentum, energy, and moisture exchange at the air-sea interface shapes both boundary layer dynamics and surface pressure patterns, but its broader implications for wind evolution remain insufficiently understood.

In this dissertation I aim to determine how interactions between the atmosphere and ocean shape equatorial boundary layer winds and surface pressure. First, I quantify the contributions of horizontal and vertical momentum transport to boundary layer winds using the storm-resolving ICON model in a coupled atmosphere-ocean-land configuration at 5 km horizontal resolution. Horizontal and vertical momentum appear to be of the same order of magnitude as the pressure gradient force. I identify two persistent wind patterns—zonal and meridional— which are driven by pressure gradients and transport processes, leading me to the development of a wind model incorporating these driving forces.

Building on this, I examine the role of winds in shaping surface pressure and explore their relationship with surface fluxes. Using ICON in an atmosphere-land-only configuration at 10 km horizontal resolution, I increased surface heat fluxes under low-wind conditions. I use ERA5 reanalysis data to compare my results and demonstrate strengthened pressure gradients and deeper atmospheric convection, revealing how small-scale surface processes drive large-scale atmospheric dynamics in the tropics. This highlights the intricate relationship between air-sea interaction and atmospheric processes.

My results contribute to a more holistic view of boundary layer winds, as mediators between the ocean and atmosphere. They are driven by processes at the ocean surface and free troposphere but also contribute to shaping these systems. I reassess the partitioning of wind-driving momentum and emphasize the role of the surface pressure distribution. I uncover processes that not only influence the boundary layer but also shape vertical profiles of density and convection through the troposphere. Nonetheless, the drivers of the underlying sea surface temperature, which forms the lower boundary condition for these dynamics, remain an open and challenging question for future research.

Zusammenfassung

Windgleichgewichte in der Grenzschicht und ihr Einfluss auf die äquatorialen Meeresoberflächentemperaturen

von Marius Winkler

Was machen äquatoriale Oberflächenwinde über dem Ozean so besonders – und warum verdienen sie unsere Aufmerksamkeit? Diese Oberflächenwinde wirken als Teil der Schnittstelle zwischen Ozean und Atmosphäre sowohl an ozeanischen als auch atmosphärischen Prozessen mit. Sie entziehen dem Ozean Wärme, übertragen diese in die darüberliegende Atmosphäre und treiben damit atmosphärische Dynamiken an, indem sie Oberflächentemperaturen, Feuchtigkeitsprofile und die Stabilität der Grenzschicht beeinflussen. Das Verständnis der Oberflächenwinde ist für Mechanismen des Energie-, Feuchtigkeits- und Impulsaustauschs in tropischen Regionen elementar.

Obwohl bekannt ist, dass temperaturbedingte Druckgradienten die Windrichtung in der äquatorialen Grenzschicht vorgeben, fehlt es an einer gründlichen Quantifizierung des Impulses in der Grenzschicht, der Windgeschwindigkeit und -richtung bestimmt. Klimamodelle beruhen oft auf einer vereinfachten Annahme bei der Parametrisierung der Oberflächenaustauschkoeffiziente für Regime mit niedrigen Windgeschwindigkeiten, wodurch Prozesse gefördert werden sollen, die nur schwer aufzulösen sind. Der Austausch von Energie, Feuchtigkeit und Impuls zwischen Atmosphäre und Ozean beeinflusst die Oberflächendruckverteilung, aber das Verständnis der Oberflächendruckmuster bleibt unvollständig.

Ich untersuche in dieser Dissertation, wie die Wechselwirkungen zwischen Atmosphäre und Ozean die äquatorialen Winde in der Grenzschicht und den Oberflächendruck beeinflussen. Zunächst quantifiziere ich die Beiträge des horizontalen und vertikalen Impulstransports zu den Grenzschichtwinden mit Hilfe des sturmauflösenden ICON-Modells in einer gekoppelten Atmosphäre-Ozean-Land-Konfiguration mit einer horizontalen Auflösung von 5 km quantifiziert. Es wird gezeigt, dass der horizontale und vertikale Impuls in der gleichen Größenordnung vorliegt wie die Druckgradientenkraft. Ich identifiziere zwei anhaltende Windmuster - zonal und meridional -, die durch Oberflächentemperaturen-Gradienten und Impulsprozesse angetrieben werden, was mich zur Entwicklung eines Windmodells führt, das diese Antriebskräfte widerspiegelt.

Darauf aufbauend untersuche ich die Rolle der Winde bei der Gestaltung des Oberflächendrucks und untersuche ihre Beziehung zu den Oberflächenaustauschkoeffizienten. Unter Verwendung von ICON in einer reinen Atmosphären-Land-Konfiguration mit 10 km horizontaler Auflösung habe ich die Oberflächenaustauschkoeffizienten für schwache Windbedingungen erhöht. Ich verwende ERA5 Reanalysedaten, um meine Ergebnisse zu vergleichen und stelle verstärkte Druckgradienten und tiefere atmosphärische Konvektion fest. Dadurch wird deutlich, wie kleinskalige Oberflächenprozesse die großskalige atmosphärische Dynamik antreiben können.

Meine Ergebnisse tragen zu einer ganzheitlicheren Betrachtung der Grenzschichtwinde als Vermittler zwischen dem Ozean und der Atmosphäre bei. Sie werden durch Prozesse an der Meeresoberfläche und in der freien Troposphäre angetrie-

ben, tragen aber auch zur Gestaltung dieser Systeme bei. Ich bewerte die Aufteilung des windgetriebenen Impulses neu und betone die Rolle der Oberflächendruckverteilung. Ich decke Prozesse auf, die nicht nur die Grenzschicht beeinflussen, sondern auch vertikale Profile der Dichte und Konvektion in der Troposphäre formen. Dennoch bleiben die treibenden Kräfte der zugrundeliegenden Meeresoberflächentemperatur, die die untere Randbedingung für die Grenzschicht darstellt, eine offene und herausfordernde Frage für zukünftige Forschung.

PUBLICATIONS RELATED TO THIS DISSERTATION

The following two studies are part of this dissertation and included in Appendix A and B.

Winkler, M., Koelling, T., Mellado, J.P., Stevens, B. (2024a): "Uncovering the Drivers of the Equatorial Ocean Surface Winds", In: *review at Quarterly Journal of the Royal Meteorological Society*

Winkler, M., Mellado, J.P., Stevens, B. (2024b): "On the Role of the Surface Flux Parametrization in Tropical Convection under Low Wind Speed Regimes", In: *preparation for submission to Geophysical Research Letters*

As a PhD student I have contributed to the following projects:

Hohenegger C., **Winkler, M.**, et al. (2023): "ICON-Sapphire: simulating the components of the Earth system and their interactions at kilometer and subkilometer scales", In: *Geoscientific Model Development*, 16 (2), 779–811. Doi: 10.5194/gmd-16-779-2023

Segura H., **Winkler, M.**, et al. (2024a): "Global Storm-Resolving Models and the Double ITCZ Bias: Air-Surface Interaction Role for Convection in Light Wind Regimes", In: *preparation for submission to Journal of Advances in Modeling Earth Systems*

Segura H., **Winkler, M.**, et al. (2024b): "NextGEMS: Entering the Era of Kilometre-Scale Earth System Modelling", In: *preparation for submission to Geoscientific Model Development*

Segura H., **Winkler, M.**, et al. (2024c): "Precipitation Accelerating Ocean Currents in a km-Scale Earth System Model", In: *preparation for submission to Geophysical Research Letters*

Having had the opportunity to participate in the ORCESTRA field campaign and oversee the radiosonde mission at the Barbados Cloud Observatory, I am currently preparing the following publication:

Winkler, M., et al. (2025): "Atmospheric Radiosoundings from Ship and Island Platforms during the 2024 ORCESTRA Field Campaign", In: *preparation for submission to Earth System Science Data*

ACKNOWLEDGEMENTS

I am deeply grateful to my two supervisors, Bjorn and Juan Pedro. Bjorn's thought-provoking questions and constructive feedback distilled the essence of this dissertation. Juan Pedro provided enduring support and first-class input, in regular meetings ensuring I kept sight of the horizon.

My heartfelt thanks go to the Atmospheric Turbulence and Boundary Layers group at the University of Hamburg for their valuable feedback during countless talks. Discussions with Tobias, Lukas, and Hans were always enlightening, and I am grateful to Kalle, René, and Monika for their indispensable ICON-related support. Divya, Luca, Moritz G., Mia-Sophie, and Henning offered valuable feedback on an early draft of this dissertation, for which I am truly thankful.

I was fortunate to share an office with Moritz G. and Yuting, whose cheerful conversations brightened my days. For countless uplifting moments, both in Hamburg and during the ORCESTRA field campaign, I thank Hernan, Luca, Divya, Arim, Abisha, Angel, Clara, Henning, Arjun, Moritz E., and Marius Rixen.

Finally, I extend my gratitude to those behind the scenes—Angela, Sebastian Rast, Antje, Connie, Michaela, Florian, and my panel chair Johann—for fostering an environment at MPI where PhD students can thrive.

Größter Dank gilt meiner Familie: meine Mutter Helga küsse ich für die Versorgung mit 20 Schnitzeln vor Abgabe dieser Arbeit – aber vor allem für ihren ständigen Rückhalt. Meinem Vater Frank danke ich dafür, dass er mir durch sein Vorleben gezeigt hat, keine Angst vor der nächsten großen Herausforderung zu haben. Meine Schwester Caro ist seit vielen Jahren eine mentale Stütze und meine liebste Mitbewohnerin in Berlin und Hamburg. Meine Brüder Falk, Claudi und Robi umarme ich für gemeinsame ausgleichende Momente – ob auf dem Fahrrad, beim Skifahren, Kitesurfen oder in der Sauna.

Ich danke Onkel Tommes für inspirierende Gespräche über Musik, Philospohie und Wissenschaft, die mich früh der akademischen Welt näherbrachten.

Meinem Lehrmeister Hans-Joachim Vauk bin ich zutiefst dankbar für seinen bedingungslosen Glauben an meine Fähigkeiten.

Besonderer Dank gilt meinem Kommilitonen Johannes, der mir die ersten Python-Lektionen erteilte und mit dem ich seit Unitagen einen ähnlichen Lebensweg teile.

Patrick und Jasper, dem Klub der Denker, schulde ich grenzenlosen Dank für ihre langjährige Freundschaft. Von Lernwochenenden zu Schulzeiten zu anspruchsvollen Gesprächen unter Planen im Regen auf dem Folkeboot mit Portwein und Erbsensuppe zwischen Dänemark und Schweden - Sapere aude!

Infinite thanks go to my partner Nina for her open ear, encouraging words, scientific exchange at all hours, and unshakable optimism. Without you, this work would not be what it is.

Ich danke Euch

-

Mit einem Handschlag, Euer Marius

CONTENTS

Part I

UNIFYING ESSAY

1 MOTIVATION

Herr: es ist Zeit. Der Sommer war sehr groß.
Leg deinen Schatten auf die Sonnenuhren,
und auf den Fluren laß die Winde los.
[. . .]

— *Herbsttag, (Rilke, 1902)*

Rainer Maria Rilke's lines evoke the subtle transition from warmth to coolness, mirroring the delicate balance that drives atmospheric movement. Just like the winds in the corridors are shaped by the effects of light and shadow, winds in the atmosphere are driven by pressure differences based on thermal contrasts. Surface winds form circulations, distribute energy within the atmosphere, and act as interpreters at the nexus between atmosphere and ocean. Boundary layer winds and their connections to oceanic and tropospheric processes remain incompletely understood.

From Ekman's early work on wind-driven ocean currents (Ekman, 1905) to the studies of Riehl et al. (1951) and Malkus (1956) progress has been made in understanding atmospheric and oceanic interactions. These foundational works show how vertical mixing processes stabilize and sustain the trade wind system. Later, Lindzen and Nigam (1987), Wallace et al. (1989) and Deser (1993) revealed how friction, the Coriolis force, and the pressure gradient force drive the boundary layer winds. Stevens et al. (2002) added the influence of the free troposphere. While early studies rested upon observational data or coarse-resolution models, more recent work, such as Stevens et al. (2020), underscore the value of large-eddy simulations (LES) and storm-resolving models at kilometer scale, such as ICON (Hohenegger et al., 2023), in capturing atmospheric dynamics at finer scales.

However, the boundary layer wind momentum has not yet been thoroughly quantified. Well-established is the strong influence of sea surface temperature (SST) on the formation of boundary layer pressure gradients, which play a key role in driving winds. Still, it remains unclear how the SST shapes the absolute pressure distribution at the air-sea interface and the specific contribution of surface fluxes to this process. Due to the new developments in global climate models, towards ICON, I now have the possibility to access temporally and spatially high-resolution model output. This allows me to conduct both a detailed analysis of the tropical boundary layer momentum embedded in its large scale environment, while also evaluating the influence of small scale surface fluxes, which leads us to the guiding research question of this thesis:

How do Interactions between Atmosphere and Ocean Influence Boundary Layer Dynamics?

2 BACKGROUND

Some say that what is called air,
when it is in motion and flows,
is wind,
[...]

— *Meteorology*, (Aristotle, 350 B.C.E)

2.1 WINDS

Winds are essential in mediating exchange of momentum, matter, and energy. They modulate ocean circulation, drive surface-air fluxes, accompany convection, and shape circulation patterns. Understanding winds is crucial for predicting both the present and the future as a key component of weather and climate. Let us take a step back and look at horizontal winds in a broader context. I will start by establishing the horizontal force balance:

$$\begin{aligned} \frac{\partial u}{\partial t} &= -\frac{1}{\rho}\frac{\partial p}{\partial x} + fv - \frac{\partial uu}{\partial x} - \frac{\partial uv}{\partial y} - \frac{\partial uw}{\partial z}, \\ \frac{\partial v}{\partial t} &= -\frac{1}{\rho}\frac{\partial p}{\partial y} - fu - \frac{\partial vu}{\partial x} - \frac{\partial vv}{\partial y} - \frac{\partial vw}{\partial z}. \end{aligned} \tag{1}$$

The six terms from left to right are: the tendency, the pressure gradient force, the Coriolis force, and three contributions to the zonal and meridional advection forces. The zonal u and the meridional component v together form the horizontal wind. The terms on the right-hand side of Equation (1) represent the factors that define the two components u and v. This applies to the Earth's atmosphere and beyond. Winds are not unique to our planet but occur across the solar system.

2.1.1 *Differential Heating and Planetary Rotation*

Winds, the movement of gases, can be generated on any planet with an atmosphere that is exposed to differential heating. Planets of our solar system with an atmosphere, that receive sunlight on one side fall into this category. The ideal gas equation helps to understand how differential heating can cause movement within their atmosphere:

$$p = \rho R T, \tag{2}$$

with the pressure p, the density ρ, the ideal gas constant R, and the temperature T. The sunlit areas of the planet are heated differently based on the angle at which solar radiation strikes the surface. As temperature T increases in these sunlit areas, the air expands, and the density ρ decreases. Consequently, warmer regions have lower density compared to cooler, non-sunlit regions, which have higher density. Air pressure, defined as force per unit area, results from the weight of the air column above each point on the surface. These density variations lead to differences in mass, creating pressure differences across the atmosphere. Such pressure differences are represented by the pressure gradient force in the wind momentum Equation (1), driving the movement of air masses.

In addition to differential heating, the rotation rate of a planet is also a driving force behind winds. The Coriolis frequency f, appearing in the third term from the left in Equation (1), is dependent on both the sine of the latitude and the rotation rate:

$$f = 2\Omega \sin\phi, \tag{3}$$

where Ω is the rotation rate and ϕ the latitude. For example, on the gas giant Jupiter, a sidereal day lasts only about 10 hours, resulting in a Coriolis frequency f that is 2.4 times greater than on Earth. This contributes to intense winds on Jupiter, reaching speeds of up to $140\,\mathrm{m\,s^{-1}}$ (Hueso et al., 2023).

The rotating Earth is exposed to solar radiation during the day. The night side facing away from the sun loses energy into space and cools through outgoing longwave radiation. This creates temperature differences between the day side and night side. Between the equator and the poles, temperature differences occur by different angles of incidence of the solar radiation. Together, these temperature differences and the Earth's rotation set the stage for the winds on our planet.

2.1.2 *Winds on Earth*

The solar radiation reaching the Earth's surface interacts with areas of varying albedo—a measure of reflectivity—as well as materials with different heat capacities and conductivities. For example, water, with its low albedo and higher heat capacity compared to minerals on land, requires more energy to increase its temperature. At the same time, the conductivity of water is greater than that of rocks and soil. For land areas, this leads to a greater dependence on the daily cycle, as the heat remains stored on the surface, where it can easily radiate back into space, and does not penetrate into the depths, where it would be stored more efficiently. In the oceans, the heat generated at the surface can be conducted more efficiently into the depths, where it is distributed over a larger volume and increases the temperature more moderately. Earth's versatile surface, divided into land and ocean with varying albedo, introduces multifaceted heating patterns that give rise to temperature-driven density differences and associated pressure gradients that drive the winds.

In the polar regions, steady easterly winds prevail, flowing from the poles toward the mid-latitudes. These winds reinforce temperature contrasts between polar and temperate zones. Moving toward the mid-latitudes, between approximately 30° and 60° latitude, we encounter the westerlies, which flow from west to east. These winds dominate the mid-latitude regions, driving the development of baroclinic waves and extratropical cyclones. From 30° latitude towards the equator, we find the trade winds, which blow from the northeast in the Northern Hemisphere and from the southeast in the Southern Hemisphere. These trade winds from both hemispheres converge in the tropical regions, forming the Intertropical Convergence Zone (ITCZ) (Windmiller and Stevens, 2024), where warm, moist air rises and drives the formation of the large-scale Hadley cell. A feature of the trade wind region are the doldrums, a belt of light, often calm winds near the equator (Klocke et al., 2017; Windmiller, 2024). Higher in the atmosphere, the air masses move poleward, cool, and eventually descend around 30°N and 30°S. Seasonal monsoon winds and variations, such as the Madden-Julian Oscillation (Madden and Julian, 1994), further contribute to the shifting patterns of tropical winds, highlighting the diverse nature of wind dynamics in this region.

These global wind patterns, shaped by large-scale processes, transition into more localized and intricate dynamics within the boundary layer, where interactions with the Earth's surface influence wind behavior over both land and ocean.

2.1.3 *Winds in the Boundary Layer*

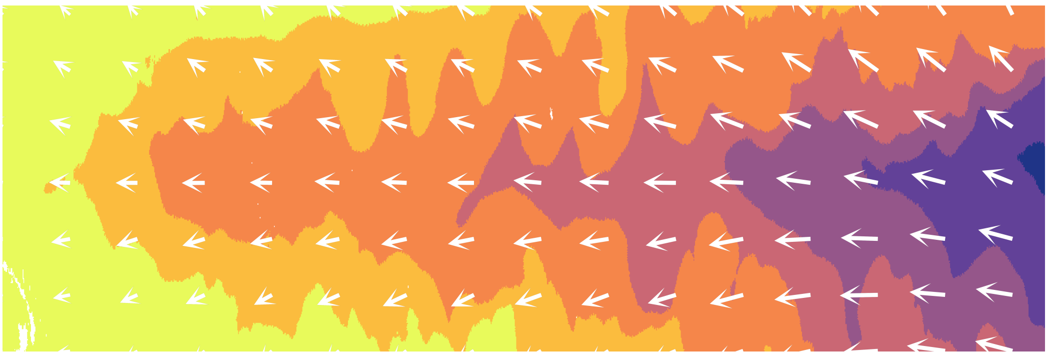

Figure 1: **Equatorial Wind-SST-Interaction.** Equatorial ocean winds overlaid on sea surface temperature (SST). Darker colors represent cooler SSTs, while lighter colors indicate warmer SSTs. White arrows show wind direction, with arrow size reflecting wind strength. Cooler SSTs tend to correspond with higher pressure, and warmer SSTs with lower pressure. Output originates from an ocean-atmosphere-land coupled ICON simulation.

Boundary layer winds over land are strongly influenced by diurnal cycles and surface friction. During the day, solar heating causes variations in wind speed and direction, with winds often becoming stronger as the ground warms and generates turbulence. At night, radiative cooling reduces wind speeds as stability increases near the surface. Later we will see that the last term of the equation (1) in an integral form of the means in time gives the divergence of the horizontal momentum flux, which can be interpreted as surface drag τ_0 at the interface, $z = 0$. Higher surface drag over land decelerates winds stronger compared to winds over the ocean, creating a more variable and localized wind profile shaped by terrain and vegetation.

Boundary layer winds over the ocean drive air-sea interactions. The bidirectional relationship of surface winds between the atmosphere and ocean is illustrated by the surface drag: on the one hand, the drag of the ocean surface decelerates the surface winds; on the other hand, surface drag can also be interpreted as surface stress, a transfer of momentum from the atmosphere to the ocean, which causes the surface current velocity to increase. In some areas along the equator, a positive feedback cycle provides a compelling example: surface wind stress drives equatorial upwelling, bringing cold water masses from deeper layers to the surface. These cold water masses lower the surface air temperature, affecting both the density and surface pressure. Pressure gradients reinforce the surface winds, which in turn drive equatorial upwelling. Figure 1 illustrates such a region over the equator. Here, with the Coriolis force being negligibly small, surface winds flow across the isobars and blow down the pressure gradient from areas of low SST (high surface pressure) to areas of high SST (low surface pressure). Surface winds drive ocean flow, while being shaped by the boundary layer pressure gradient created through thermal exchange at the ocean surface.

Boundary layer winds regulate the exchange of energy and moisture and influence large-scale patterns like the trade winds, monsoons (Neelin et al., 1987; Emanuel, 1987; Richter et al., 2017) and impact the global heat redistribution (Held and Hou, 1980; Hou and Lindzen, 1992). Understanding boundary layer winds is vital for the research of weather patterns, extreme events, and climate, especially over tropical oceans where a large portion of Earth's available energy is stored in the form of heat.

2.2 From Halley's Map to Modern Models: Exploring Equatorial Boundary Layer Winds

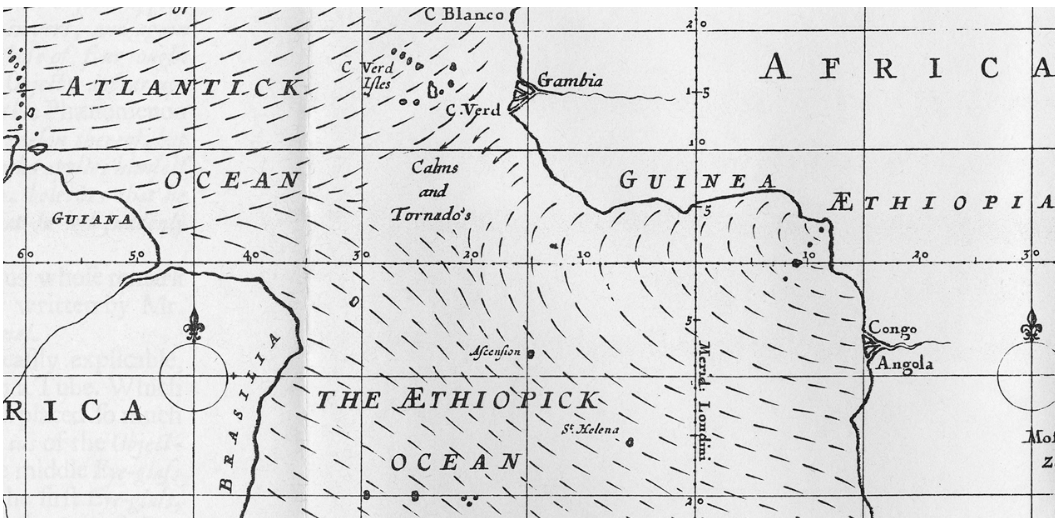

Figure 2: **Atlantic Trade Winds.** Section of the tropical Atlantic on the map of the trade winds by Halley (1686).

Equatorial boundary layer winds over the oceans have long been of central importance to maritime trade. Figure 2 shows one of the earliest maps of the trade winds created by Halley in the 17th century (Halley, 1686), highlighting a region in the equatorial Atlantic marked by "Calms and Tornados"—a testament to the challenges faced by sailors navigating this unpredictable zone. The oceans along the equator are characterized by shifting wind patterns, sudden squalls, and heavy rainfall, posed risks for sailing ships and their crews. While the advent of steamships reduced reliance on the trade winds for commerce, the equatorial region remains a site of dynamic interactions between the ocean and atmosphere. Phenomena such as the Doldrums, the tropical rain belt, and the Intertropical Convergence Zone (ITCZ) define this region, where pressure gradients, convective processes, and surface fluxes interplay in ways that are still not fully understood.

One of the first systematic studies of Pacific trade winds was conducted by Riehl et al. (1951), who highlighted the crucial role these winds play in maintaining large-scale tropical circulation patterns. Monin and Obukhov (1954) introduced turbulent mixing theory in the surface layer, providing the foundational framework for understanding how variations in fluxes drive changes in wind velocity and temperature profiles. Building on this, Malkus (1956) further explored the structure of the trade wind boundary layer, revealing how its vertical profile fluctuates due to diurnal heating and turbulence. Malkus identified turbulence and vertical mixing as key factors influencing wind speed variability near the surface, where frictional forces slow down the winds. These foundational studies demonstrate that while trade winds are steady at large scales, they exhibit variability within the well mixed boundary layer due to the intricate interplay of ocean surface and atmospheric processes.

Large-scale observational campaigns, such as BOMEX (*Barbados Oceanographic and Meteorological Experiment*, Holland and Rasmusson (1973), Nitta and Esbensen (1974), and Siebesma (1998)), ATEX (*Atlantic Trade Wind Experiment*, Augstein et al. (1973), Augstein et al. (1974), and Stevens et al. (2001)) in the late 1960s, and TOGA COARE (*Tropical Ocean-Global Atmosphere Coupled Ocean Atmosphere Response Experiment*, Webster and Lukas (1992)) in the early 1990s, were landmark efforts to deepen our understanding of atmosphere-ocean interactions, especially in tropical regions. BOMEX and ATEX revealed vertical boundary layer profiles, showing reduced wind speeds near the surface due to friction, increasing with altitude as surface drag vanishes. TOGA COARE, focused on the convective western Pacific, provided unprecedented data on heat, moisture, and momentum transfer under varying convective conditions. Insights gained from field campaigns like those mentioned above laid the groundwork for understanding tropical dynamics, paving the way for the development of global circulation models in the early 1960s and their continual refinement.

In the 1980s, Lindzen and Nigam (1987) explored how SST-induced pressure gradients help drive surface winds, particularly the trade winds. Their foundational work, along with subsequent studies by Wallace et al. (1989), incorporated modeling efforts to examine how large-scale SST patterns influence wind structures. This era saw a shift towards understanding how the broader trade wind systems interact with boundary layer dynamics. At the same time, mechanisms like the Wind-Induced Surface Heat Exchange (WISHE) introduced by Emanuel (1987) gained prominence. Emanuel (1987) showed how surface winds enhance surface heat fluxes, intensifying atmospheric convection. This feedback loop demonstrates how surface-atmosphere interactions operate, with wind speeds regulating energy transfer across the air-sea interface, while the ocean surface itself—through sea surface temperature—sets the stage for the development of boundary layer winds.

Coupled ocean-atmosphere models have enabled deeper investigation into the mechanisms that shape equatorial boundary layer winds. Xie and Philander (1994) used a 2-dimensional model to show that surface latent heat fluxes modulate wind patterns and that wind-induced SST variability can create asymmetries even under symmetric solar forcing. However, the small-scale turbulent nature of these phenomena created the urge for high-resolution but realistic models. Using field campaign data from ATEX and BOMEX Stevens et al. (2001) initialized large-eddy simulations (LES) with observational data to study the finer scales. These simulations revealed that trade wind cumulus clouds actively modulate turbulence and vertical mixing, influencing wind structures within the boundary layer. Further work by Stevens (2005) explored the complexity of cloud-topped boundary layers, demonstrating the intertwined nature of turbulence, clouds, and entrainment processes in shaping boundary layer wind speeds.

Despite the advancements brought by LES, these simulations remain limited to specific domain sizes and often rely on prescribed SST. They use periodic boundary conditions, which introduce an element of artificiality and limit their ability to fully capture real-world atmospheric dynamics. To evaluate the contributions of fine-scale turbulence, as well as small-scale interactions at the air-sea interface within the large-scale context, coupled storm-resolving models with kilometer-scale resolution are essential. As we will see, advection forces (terms four, five, and six in Equation (1)) emerge as key drivers but remain underexplored due to the spatial and temporal limitations of previous climate models, leaving boundary layer momentum analysis incomplete.

Therefore, with the recently available global, coupled storm-resolving model ICON, I refine the guiding research question from Chapter 1 into two focused research questions, the first being:

What Drives Equatorial Boundary Layer Winds ?

I will show that ICON has limitations in parameterizing winds in low wind speed regimes. These low-wind regimes are often found in regions where surface fluxes have decisive influence on the surface pressure distribution. Current parameterizations are based on Monin-Obukhov similarity theory (Monin and Obukhov, 1954), which provides the theoretical basis for parameters used in the bulk formula. Kitamura and Ito (2016) revisited bulk surface flux calculations in

LESs and found that velocity adjustments are needed under free convective conditions. Against the background of atmosphere-land-only simulations using the storm-resolving model ICON with ideal, prescribed SST distributions, I introduce the second research question of this thesis:

How Do Surface Heat Fluxes Drive Surface Pressure and Boundary Layer Winds?

I will address both research questions sequentially in Chapter 3 and Chapter 4, before concluding in Chapter 5 whether I achieved my intended goals.

2.3 OUTPUT AND DATA

Within this thesis I utilize simulation output from both atmosphere-ocean-land-coupled and atmosphere-land-only configurations of the ICOsahedral Nonhydrostatic (ICON) Earth-system model. The storm-resolving model ICON at kilometer-scale, described by Hohenegger et al. (2023), follows the DYAMOND2 protocol (Stevens et al., 2019) as part of the collaborative European project NextGEMS (Next Generation Earth Modelling Systems, https://nextgems-h2020.eu/). The coupled configuration used for Chapter 3 and referred to as G_AO_5km in Hohenegger et al. (2023), employs a grid spacing of 5 km with 90 vertical atmospheric levels, 128 ocean levels, and five horizontal soil layers. This simulation is initialized with Integrated Forecasting System (IFS) analysis from January 20, 2020, and runs until February 28, 2022.

The atmosphere-land-only ICON simulation output I utilize within Chapter 4, employs a grid spacing of 10 km and 90 vertical levels (reduced to 26 for focused analysis of the lower atmosphere). This configuration is initialized using a prescribed ocean temperature aligned with IFS analysis starting from January 1, 1979, and running through March 31, 1979. The different time span is due to changes in the work flow within our institute.

To further support my analyses, I compare my results with data from ERA5 (Hersbach et al., 2020), provided by the European Centre for Medium-Range Weather Forecasts (ECMWF) and accessed via the Copernicus Climate Change Service (C3S) Climate Data Store. The ERA5 data used here has a spatial resolution of $0.25° \times 0.25°$.

From both ICON and ERA5 datasets, I extract key atmospheric and oceanic variables, including pressure p, zonal and meridional wind components u and v, air temperature T, and density ρ. For the coupled ICON configuration, additional variables such as sea surface temperature T_{SST}, surface drag $\tau(0)$, and specific humidity q are included. The three-dimensional fields p, ρ, T, u, v, and q are available as six-hourly snapshots, while T_{SST} and $\tau(0)$ are provided at hourly and 30-minute intervals, respectively, in the coupled simulation. In the atmosphere-land-only configuration, fields are available as daily snapshots.

3 UNCOVERING THE DRIVERS OF THE EQUATORIAL OCEAN SURFACE WINDS

In this chapter I start by analyzing the wind patterns present at the equator. Afterwards, I will introduce a definition of the the boundary layer height, followed by an exploration of the boundary layer wind momentum and the contributions of atmospheric forces, including pressure gradients, turbulent fluxes, and advection. I aim to provide a deeper understanding of the interactions between the sea surface and the atmosphere that shape boundary layer dynamics, which is needed to answer the first of the two central research question that I introduced in Section 2.2:

What Drives Equatorial Boundary Layer Winds?

The following sections outline the core insights from the study, which is thoroughly presented in Appendix A.

3.1 EQUATORIAL BOUNDARY LAYER WIND PATTERNS

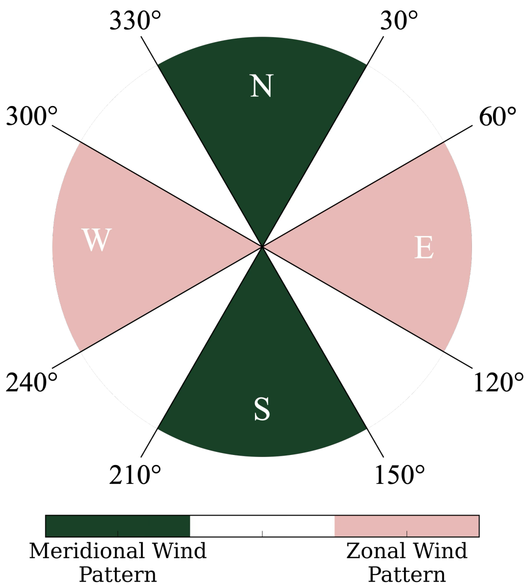

Figure 3: **Classification of Wind Patterns.** Depending on the segment in which a wind vector lies, it is either assigned to the Meridional Wind Pattern, the Zonal Wind Pattern or the transient area in between. I do not differentiate between different signs. Easterlies and Westerlies, as well as Northerlies and Southerlies are assigned to the same wind pattern as long as they appear in the corresponding segment.

Categorizing equatorial wind patterns allows for a structured understanding of the boundary layer dynamics. One might expect these winds to be relatively uni-

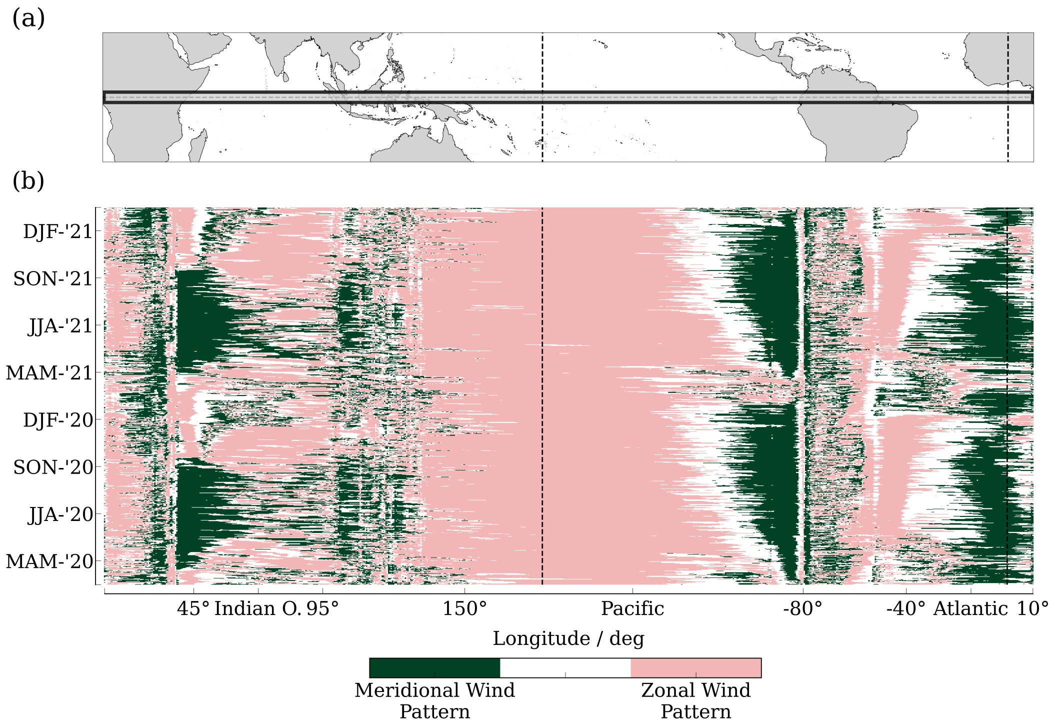

Figure 4: **Wind Patterns along the Equator.** (a) Region of interest. (b) Daily mean wind patterns averaged meridionally between $-2°$ and $2°$ latitude, including land areas, based on a two-year ICON simulation. The Meridional Wind Pattern is shown in green, while the Zonal Wind Pattern is displayed in pink, with white indicating the transition between the two regimes.

form due to the weak Coriolis force at the equator. However, my study reveals two distinct patterns that dominate equatorial surface winds: the Zonal Wind Pattern and the Meridional Wind Pattern. Figure 3 illustrates how I assign a wind vector to one of two wind patterns: based on the direction of the wind vector at the corresponding geographical location, I assign it to a segment. Rather than considering the sign, I focus solely on whether the winds are parallel or perpendicular to the equator. The Zonal Wind Pattern resembles the well-known trade winds, flowing primarily parallel to the equator, driven by the zonal pressure gradient force. The Zonal Wind Pattern is reinforced by vertical momentum transport from the free troposphere, creating a strong flow that affects large-scale ocean currents. In contrast, the Meridional Wind Pattern features winds crossing the equator is driven primarily by the meridional pressure gradient. This pattern exhibits a distinct seasonal cycle and is most pronounced in the Atlantic, eastern Pacific, and Indian Ocean.

In Figure 4, the wind variability across the globe is visualized as a meridional mean of daily wind output between $-2°$ and $2°$ latitude. Figure 4 highlights the spatial distribution of the Zonal and Meridional Wind Patterns over the equatorial oceans and landmasses. Over the open ocean, persistent wind regimes emerge, with the Zonal Wind Pattern prevailing in the western and central Pacific, while the Atlantic and eastern Pacific are dominated by the Meridional Wind Pattern.

The Indian Ocean with the Zonal Wind Pattern peaking during DJF and the Meridional Wind Pattern during JJA exhibits strong seasonal contrasts. In contrast, land areas show highly variable wind patterns, with no clear dominance of either regime. In the following sections, I will define the boundary layer height, followed by an examination of the inner structure of the two previously mentioned boundary layer wind patterns over the ocean.

3.2 DEFINITION OF THE ATMOSPHERIC BOUNDARY LAYER HEIGHT

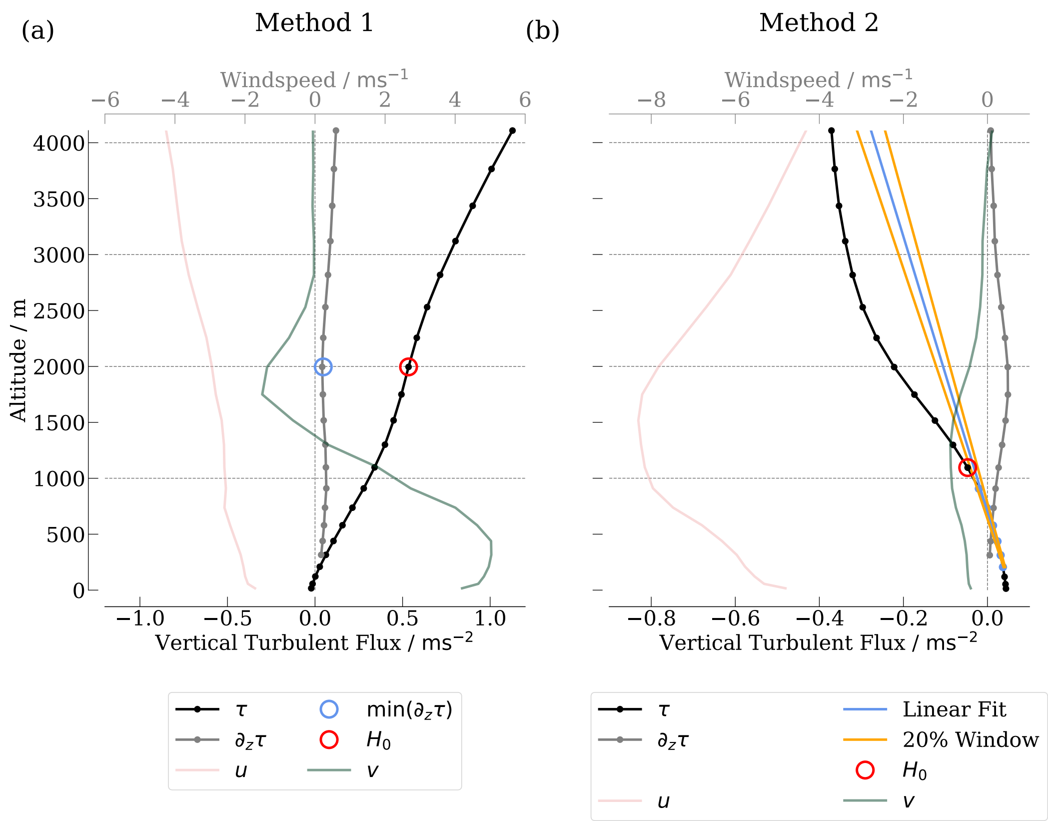

Figure 5: **Determination of ABL Height.** Vertical profiles of the turbulent flux τ and its vertical gradient $\partial_z\tau$. (a) In cases where a clear local minimum of $\partial_z\tau$ is observed, the ABL height is marked by a red circle, as shown for the Atlantic (SON, 2020). (b) In the absence of a clear minimum, such as in the western Pacific (MAM, 2020), a linear fit is applied, with the ABL height defined as the first point where the flux deviates outside a $\pm 10\,\%$ tolerance window. I have added a second x-axis above both panels and adjusted the transparency of the underlying vertical wind components using an alpha value.

Defining the atmospheric boundary layer (ABL) height is essential for accurate momentum analyses within the boundary layer, as it marks the transition between surface-driven turbulent flow and more stable winds aloft in the free troposphere. The ABL height controls how much momentum is transferred from higher atmospheric layers to the surface, making it a decisive definition for studies of near-surface winds and surface-atmosphere interactions. There are several approaches to defining the ABL height: Nuijens et al. (2014) use temperature and humidity measurements at the Barbados Cloud Observatory (Stevens et al., 2016) in the North Atlantic trade winds and relate the cloud-base heights close to the lifting condensation level at 700 m ± 150 m. Albright et al. (2023) use the virtual potential temperature to estimate the mean subcloud-layer height, at 708 m which coincides with the mean lifting condensation level in their analysis. However, I have developed an alternative method based on the vertical turbulent flux. This approach aims to clearly distinguish the well-mixed, turbulent boundary layer from the less turbulent free troposphere, trying to make the momentum within the boundary layer explicitly available. I calculate the vertical turbulent flux as the residual of the integral of the momentum equation.

I integrate the momentum Equation (1) from the air-sea interface ($z = 0$) to a vertical height level (z_i). The linearity of the integrals preserves the balance such that I can require the right-hand side of the equations to be closed in themselves. In doing so, I rearrange as follows:

$$\begin{aligned} 0 &= \int_0^{z_i} dz \left[-\frac{1}{\rho}\frac{\partial \overline{p}}{\partial x} + f\overline{v} - \frac{\partial \overline{u}}{\partial t} - \frac{\partial \overline{uu}}{\partial x} - \frac{\partial \overline{uv}}{\partial y} \right] + \tau_u(z_i) - \tau_u(0), \\ 0 &= \int_0^{z_i} dz \left[-\frac{1}{\rho}\frac{\partial \overline{p}}{\partial y} - f\overline{u} - \frac{\partial \overline{v}}{\partial t} - \frac{\partial \overline{vu}}{\partial x} - \frac{\partial \overline{vv}}{\partial y} \right] + \tau_v(z_i) - \tau_v(0). \end{aligned} \tag{4}$$

The overbars denote three-month seasonal time means. Due to the different magnitude of vertical winds w compared to the horizontal winds u, v, I assumed already that $\overline{uw} = \overline{u'w'} + \overline{u}\ \overline{w} \approx \overline{u'w'}$, so that $\overline{u}\ \overline{w}$ with the time mean of the vertical wind is negligible, hence $w \ll u, v$. The same applies to $\overline{vw} \approx \overline{v'w'}$. I identify the prime terms as the turbulent momentum terms and define: $(\tau_u, \tau_v) = -(\overline{u'w'}, \overline{v'w'})$, which denote the surface drag $\tau_{u,v}(0)$ at $z = 0$ and the vertical turbulent flux $\tau_{u,v}(H_0)$ at $z = H_0$, the top of the boundary layer H_0. If I apply this to Equation (1), I obtain $\partial_z(\tau_u, \tau_v)$, which results in the two terms on the right hand side of Equation (4), one denoting the divergence of the horizontal momentum flux at z_i and the other at the surface. The latter denotes the surface drag $\tau_{u,v}(0)$, the former the vertical turbulent flux $\tau_{u,v}(z_i)$.

To compute the equatorial ABL height H_0, I evaluate the integral of Equation (4) for each atmospheric layer, beginning at the air-sea interface working upwards. I expect the ABL to end below 4000 m, so I limit the calculation to that height (Albright et al., 2023; Nuijens et al., 2022). By cumulatively integrating the momentum for each layer, I obtain the vertical turbulent flux τ as a residual from the momentum balance. Next, I calculate the contribution of the vertical turbulent flux for each equatorial ocean basin, averaging the data spatially. I identify the local minimum along the vertical profile of the vertical turbulent flux:

$$\min\left(\frac{\partial \tau}{\partial z}\right) \Rightarrow z = H_0 \tag{5}$$

This local minimum $z = H_0$ marks the height where the vertical momentum exchange is minimal, indicating the decoupling between the boundary layer and the free troposphere.

However, not all profiles show a clear local minimum, so I employ a secondary method in case the first approach fails. This alternative method involves skipping the first three surface levels of the profile and performing a linear fit over the next five layers. A tolerance window of $\pm 10\,\%$ is then applied to the linear fit, and the boundary layer height is defined as the point where the first value deviates outside this window.

Figure 5 shows the resulting vertical profiles of the vertical turbulent flux τ, the vertical gradient of the vertical turbulent flux $\partial_z \tau$ and the vertical profiles of the horizontal wind components u and v. In Figure 5 (a), I illustrate the first method, where I identify the ABL height as the local minimum of the vertical turbulent flux gradient $\partial_z \tau$, indicated by the light blue circle $z = H_0(z) = H_0$. This case corresponds to the Meridional Wind Pattern, characterized by a dominant meridional wind component and greater wind speeds within the boundary layer compared to the free troposphere above. In Figure 5 (b), I illustrate the second method I use when a clear minimum is not detectable. In this approach, the ABL height, indicated by a red circle, represents the first value outside the tolerance window. This case features the Zonal Wind Pattern, with a dominant zonal wind component peaking above the boundary layer.

The first method is more physically grounded since it directly relates the ABL top to the height at which vertical momentum exchange diminishes. However, given the challenges in identifying this point consistently, I use the second method as a statistical fallback to ensure I can proceed with the analysis even when the physical criteria are unclear. This dual approach allows me to balance physical insight with practical adaptability.

3.3 THE INTERPLAY OF SEA SURFACE TEMPERATURE AND FREE TROPOSPHERE: MOMENTUM TRANSFER SHAPES SURFACE WINDS

In this section, I will take a closer look at two representative momentum balances for the Zonal Wind Pattern and the Meridional Wind Pattern. As an example, I will choose the three-month average March, April, May (MAM), 2020 of the western Pacific for the Zonal Wind Pattern and the three-month average September, October, November (SON), 2020 of the Atlantic for the Meridional Wind Pattern.

The top row of Figure 6 (panel (a) and (b)) show the momentum balance for the Zonal Wind Pattern in the western Pacific during MAM 2020 and reveal distinct dynamics between zonal and meridional momentum. The average wind speed for the zonal component is $5\,\mathrm{m\,s^{-1}}$, while the meridional wind speed is notably lower, remaining below $1.7\,\mathrm{m\,s^{-1}}$, roughly a third of the zonal speed.

In contrast to the meridional momentum (b), where the sign of individual terms changes between the hemispheres, the zonal momentum (a) retains consistent signs, contributing to the persistence of the Zonal Wind Pattern across both hemispheres. The largest contributions come from zonal and meridional advection of zonal momentum and the zonal vertical turbulent flux at the top of the ABL. The

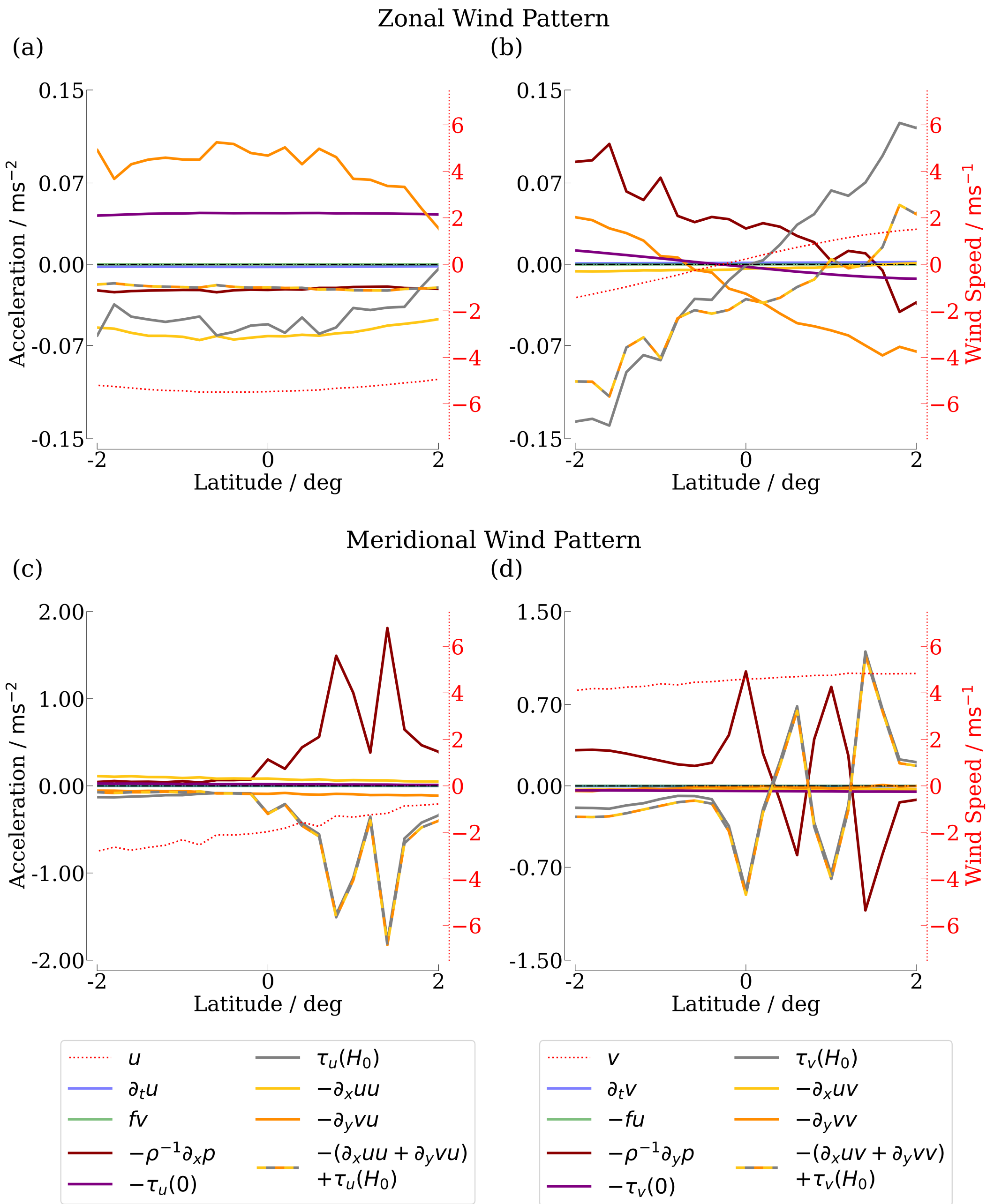

Figure 6: **Zonal Mean of Momentum Balances.** (a) zonal and meridional (b) momentum for the Zonal Wind Pattern in the western Pacific, MAM, 2020; (c), (d) for the Meridional Wind Pattern in the Atlantic, SON, 2020. The yellow-gray-orange zebra lines represent the sum of the horizontal advection forces and vertical turbulent flux at the top of the ABL. The left and right y-axes show different units: the left, solid y-axes represent the range of values of the solid lines of the momentum terms, the right, dotted y-axes refer to the zonal mean wind speed, shown as a red dotted line. Panel (a) and (c) share the left legend and panel (b) and (d) the right legend.

direction and acceleration of the wind are driven by the zonal pressure gradient force, with the opposing horizontal advection forces largely balancing each other out. The combined influence of horizontal advection and the zonal vertical turbulent flux reinforces the pressure gradient force, while the zonal surface drag and meridional advection of zonal momentum act against it. The contributions from the zonal Coriolis force and tendency are minimal and can be neglected.

The meridional momentum (Figure 6 , panel (b)) shows greater variability across latitudes, with the vertical turbulent flux playing a dominant role in driving the meridional wind on both hemispheres. Here, the pressure gradient force and the sum of horizontal advection and meridional vertical turbulent flux counteract one another, almost canceling out. Unlike the zonal component (a), the pressure gradient for the meridional wind (b) is not aligned with the wind direction, indicating that the weaker meridional component is primarily driven by the vertical turbulent flux in the Zonal Wind Pattern.

The momentum balance for the Meridional Wind Pattern in the Atlantic during SON 2020, presented in Figure 6 (c) and (d), also reveals distinct dynamics for the zonal and meridional components. Both components exhibit variations across latitudes. The meridional wind shows an average speed of $5\,\mathrm{m\,s^{-1}}$, while the zonal component reaches a maximum of $2\,\mathrm{m\,s^{-1}}$. The dominant factor in the Meridional Wind Pattern is the meridional momentum (Figure 6 , panel (d)). The largest contributions come from the meridional vertical turbulent flux and the meridional pressure gradient at the top of the ABL. As in the Zonal Wind Pattern, the meridional Coriolis force and tendency are minimal and can be neglected. The meridional pressure gradient force accelerates the wind, with the vertical turbulent flux, surface drag, and a small contribution from horizontal advection acting to balance this driving force. Together, the meridional vertical turbulent flux, surface drag, and horizontal advection slow the wind down. In contrast to the meridional wind (d), the pressure gradient is not aligned with the wind direction for the zonal wind (c), indicating that in the Meridional Wind Pattern, the zonal component, is less dominant and arises mainly in response to other forces.

My momentum analysis of the prevailing wind patterns is shown here through representative examples from two ocean basins and seasons. These results build upon earlier works, such as those by Lindzen and Nigam (1987) and Deser (1993), which identified sea surface temperature gradients as critical to surface wind dynamics. My analysis builds on the work of Stevens et al. (2002), who acknowledged the importance of free tropospheric influences, by quantifying the contributions of vertical turbulent fluxes and horizontal advection in the free troposphere. I show that these terms are as relevant as the pressure gradient force in shaping wind patterns and offer a more detailed momentum budget assessment. As such, my results address a key gap in understanding the interplay between SST gradients and momentum exchange from the free troposphere in shaping equatorial boundary layer winds.

3.4 FROM RAYLEIGH FRICTION TO A REVISED WIND MODEL: LINKING SEA SURFACE TEMPERATURE WITH FREE TROPOSPHERE DYNAMICS

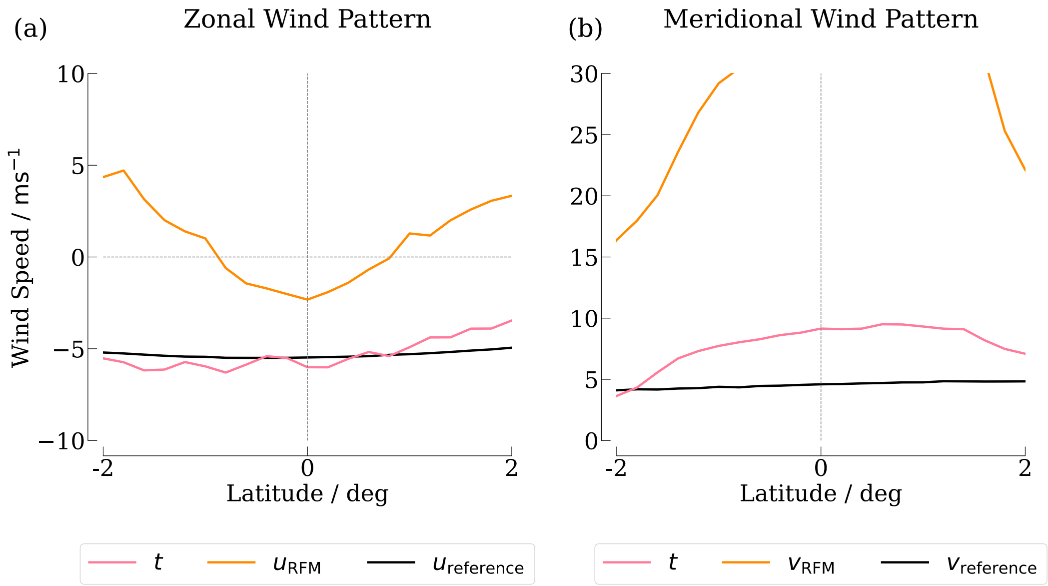

Figure 7: **Zonal Mean of the Equatorial Wind Patterns over the Ocean.** (a) Zonal winds of the Zonal Wind Pattern in the western Pacific (MAM, 2020) and (b) meridional winds of the Meridional Wind Pattern in the Atlantic (SON, 2020) are displayed. The black lines represent the reference winds from the ICON output, while the orange lines correspond to the RFM. The light red lines show the results of the revised model for tangential velocities (Equation (10)). The top of the ABL for (a) is at $H_0 = 1096\,\mathrm{m}$ and for (b) at $H_0 = 1993\,\mathrm{m}$.

A key outcome of my study is the development of a revised wind model. The Rayleigh Friction Model (RFM) has historically been used for modeling equatorial ocean winds. It bases on the pressure gradient force, the Coriolis force, and the surface drag while neglecting horizontal and vertical advection. Consequently, it is limited in representing the multilayered dynamics that govern wind patterns at the equator. In this section I will show that accounting for the essential roles of vertical and horizontal transport terms is vital for accurately modeling winds near the equator. The equatorial region presents unique challenges due to the weak influence of the Coriolis force and the contributions from momentum transport through the ABL.

Building on the momentum balance analysis I discuss in Section 3.3, I identify two main insights essential to understanding equatorial wind formation. First, I recognize the surface pressure distribution—and thus the pressure gradient force—as a critical driver of both equatorial wind patterns. To determine the influence of the sea surface temperature (SST) on surface pressure and boundary layer winds, I compute the pressure distribution from the SST, extending the framework established by Lindzen and Nigam (1987) and later studies. Second, by incorporating both horizontal and vertical momentum transport, I capture the contributions of advection and turbulent fluxes that are absent in the RFM. I begin by considering the general form of the momentum equation and integrating it over the depth of the ABL (Equation (4)), taking into account the surface drag and turbulent fluxes at the top of the boundary layer.

Through this integration, I express the momentum balance for the boundary layer winds in terms of the vertical turbulent flux at the top of the ABL, $\tau_{U,V}(H_0)$, and the surface drag, $\tau_{U,V}(0)$. This yields the following form for the zonal and meridional components of the momentum balance, with the horizontal and vertical transport terms denoted by $\overline{\mathcal{T}}_{U,V}$. Note that I choose capital letters for the vertical integral within the ABL:

$$\tau_U(0) = -\overline{\mathcal{T}_U} - \frac{1}{\rho}\frac{\partial \overline{P}}{\partial x}, \quad \tau_V(0) = -\overline{\mathcal{T}_V} - \frac{1}{\rho}\frac{\partial \overline{P}}{\partial y}, \tag{6}$$

where overbars denote seasonal time means.

Given the importance of the pressure gradient force in driving the leading wind component, I now focus on modeling the tangential wind t, which flows along the pressure gradient direction. To simplify this, I transform the coordinate system to align with the pressure gradient, introducing tangential (x_t) and normal (x_n) coordinates. In this transformed system, the pressure gradient along the isobars vanishes, simplifying the momentum equations. The key drivers of the tangential wind t are the pressure gradient and the transport terms, while the normal component is primarily influenced by the transport terms alone. Thus, the momentum balance for the tangential wind component becomes:

$$\tau_t(0) = -\overline{\mathcal{T}_t} - \frac{1}{\rho}\frac{\partial \overline{P}}{\partial x_t}, \quad \tau_n(0) = -\overline{\mathcal{T}_n}. \tag{7}$$

Recognizing that the surface drag $\tau_t(0)$ is proportional to the tangential wind speed, I apply a parameterization similar to that used in the RFM:

$$\tau_t(0) = \frac{\widehat{C}_d t}{H_0} \cdot t, \tag{8}$$

where $\widehat{C}_d$ is the rescaled drag coefficient, adjusted to account for the mean wind speed within the ABL.

Finally, substituting the parameterization of the surface drag into the momentum equation for the tangential wind, I arrive at the following relationship:

$$\frac{\widehat{C}_d t}{H_0} \cdot t = -\frac{1}{\rho}\left(\overline{\mathcal{T}_t} + \frac{\partial \overline{P}}{\partial x_t}\right). \tag{9}$$

To solve for the tangential wind t, I isolate t and take into account the sign of the pressure gradient force. This leads to the final equation for the tangential wind component:

$$t = \operatorname{sgn}\left(-\frac{\partial \overline{P}}{\partial x_t}\right) \cdot \sqrt{\left|-\eta\left(\overline{\mathcal{T}_t} + \frac{\partial \overline{P}}{\partial x_t}\right)\right|}, \tag{10}$$

where $\eta = H_0/\widehat{C}_d\rho$. The radicand is not defined for negative values, so I insert absolute values. However, this causes the sign to be lost, which defines the wind direction. Therefore, I apply the sign function to the pressure gradient force in front of the square root. Finally, Equation (10) encapsulates the balance of forces driving the tangential wind, accounting for both the pressure gradient and the transport terms.

Figure 7 shows the comparison between the revised wind model and the RFM. Panel (a) depicts the Zonal Wind Pattern and panel (b) the Meridional Wind Pattern. The components representing the RFM fail to match the magnitude and even the sign of the reference winds from the ICON output. In contrast, the revised model for the tangential wind component (Equation (10)) aligns closely with the reference winds, accurately capturing both the tangential component of the Zonal and Meridional Wind Pattern. Small deviations are present which are likely due to SST variations affecting the SST-based surface pressure field or my assumption of a constant ABL height within each basin, neglecting its potential latitude dependence.

Nevertheless, the revised model successfully incorporates the critical transport terms—absent in the RFM—resulting in a more accurate representation of the winds, particularly in regions where the pressure gradient force drives the dominant wind component.

In this chapter I uncover the key mechanisms driving equatorial boundary layer winds. It turned out that besides the pressure gradient, horizontal advection and vertical turbulent flux define the boundary layer wind as well. I defined wind patterns, established a method for determining the ABL height, and developed a revised wind model that incorporates the relevant transport terms, achieving better agreement with reference data. These findings bridge the gap between models based solely on SST-driven surface pressure gradients and a more comprehensive understanding of boundary layer winds as an integral part of the lower atmosphere, interacting with the troposphere above.

4

ON THE ROLE OF THE SURFACE FLUX PARAMETRIZATION IN TROPICAL CONVECTION UNDER LOW WIND SPEED REGIMES

This chapter explores how surface flux parameterization impacts surface pressure distribution, boundary layer winds, and broader tropical atmospheric dynamics under low wind speed regimes. I begin by comparing surface pressure fields and wind patterns in the Control simulation to ERA5 reanalysis, focusing on discrepancies in pressure gradients and their effect on wind velocities. Afterwards, I will focus on heat and momentum exchange at the ocean-atmosphere interface by incorporating insights from a standalone surface flux algorithm (COARE3.6) and I will evaluate the adjustments of a new experiment called OptiFlux. By investigating how enhanced heat transfer influences surface pressure and wind patterns, I aim with this chapter to clarify the feedbacks driving atmospheric circulation. This brings me to the second of the two central research question that I introduced in Section 2.2:

How Do Surface Heat Fluxes Drive Surface Pressure and Boundary Layer Winds?

The following sections outline the core insights from the study, which is thoroughly presented in Appendix B.

4.1 WHAT DRIVES THE SURFACE PRESSURE DISTRIBUTION?

Figure 8 compares surface pressure fields from an ICON atmosphere-land-only simulation (Control) with ERA5 reanalysis for March 1979. Both datasets reveal a pressure gradient towards the equator, yet the Control simulation exhibits a notably weaker zonal pressure gradient than ERA5, with fewer contour lines appearing within the black boxes. Although the Control simulation shows an almost identical sea surface temperature distribution to ERA5, the surface pressure patterns differ especially along the equator. This contradicts my expectations, which are based on the Lindzen and Nigam (1987) framework, where the SST distribution is expected to imprint directly onto the surface pressure. This raises an open question: do these differences stem from limitations at the air-sea interface, where surface fluxes drive energy exchange, or from processes within the atmospheric model itself?

Before I answer this question, I look into how weaker pressure gradients impact surface winds, as illustrated in Figure 9. This figure presents a probability density function (PDF) of surface wind speed (panel (a)), the meridional pressure profiles (panel (b)) and the corresponding pressure gradients (panel (c)). The Control simulation shows a higher frequency of lower wind speeds than ERA5, with wind speeds below $5\,\mathrm{m\,s^{-1}}$ occurring more frequently. Panel (b) highlights

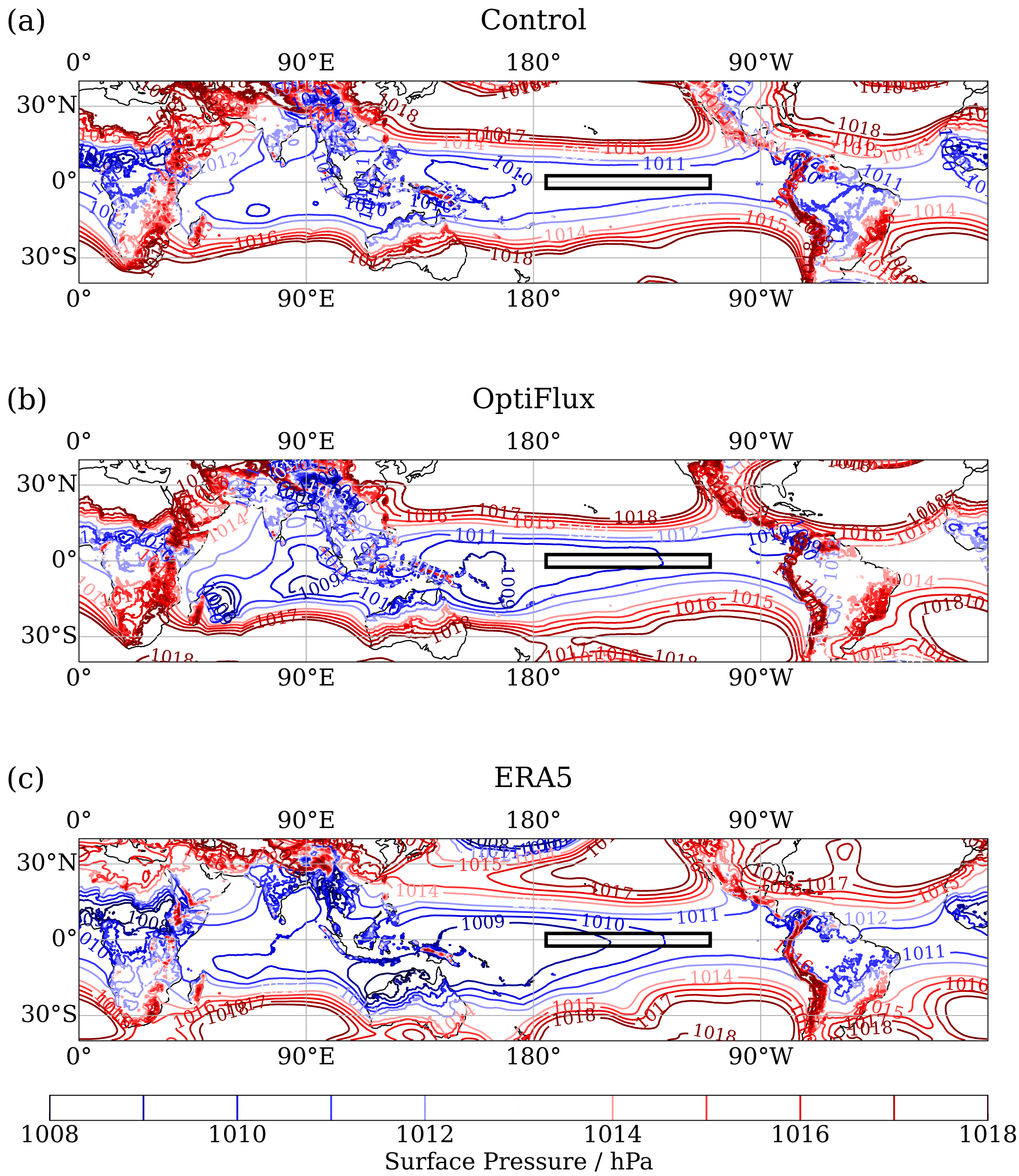

Figure 8: **Tropical Surface Pressure.** Surface pressure for March 1979 shown as contour lines from the ICON atmosphere-land-only (a) Control simulation, (b) OptiFlux simulation, and (c) ERA5 reanalysis. The black boxes frame a region of interest for further analysis in Figure 9.

the meridional mean pressure profiles, showing that while the Control simulation exhibits higher surface pressures along longitudes than ERA5. Additionally, the zonal pressure gradient in the Control simulation, shown in Figure 9 (c), is $3.5\times$ smaller than in ERA5. This suggests that the weaker pressure gradients in the Control run contribute to reduced wind velocities, as indicated by the mean values of the different PDFs. In contrast, ERA5 has a stronger wind regime, with higher wind speeds occurring more often.

To revisit my initial question on the origins of the weak surface pressure gradients in Control, I propose two hypotheses: first, that weak air-sea coupling in Control limits the SST-driven development of pressure gradients; and second, that weak pressure gradients arise from limited convectively driven density gradients in the free troposphere, leading to a muted surface pressure response.

To test these hypotheses, I produced Figure 10 which shows vertical density and temperature profiles across the western and eastern Pacific. Panel (b) presents the vertical profiles of density differences between the western and eastern Pacific, highlighting how Control's boundary layer exhibits a stronger east-west density gradient than ERA5 up to around 2000 m. This structure indicates that Control effectively captures the SST-driven density profile within the boundary layer, suggesting that SST variations influence Control's density field at lower altitudes. ERA5, in contrast, shows a more uniform density profile in the boundary layer, which suggests a reduced direct sensitivity to SST gradients within this layer. According to the approach by Lindzen and Nigam (1987), this pronounced boundary layer gradient in Control would theoretically support SST-driven pressure gradients. However, the overall surface pressure gradient in Control remains weaker than in ERA5 (c.f. Figure 9 (b)), implying that the SST alone cannot account for a realistic surface pressure distribution.

The profiles in panel (c) and (d) of Figure 10 reveal that Control is consistently colder than ERA5 across both regions, indicating that the strong density difference in the boundary layer does not stem from Control being warmer over warm ocean areas (e.g., the western Pacific) and cooler over cold areas (e.g., the eastern Pacific). This clarifies that the boundary layer density gradient observed in Control is not due to an SST-induced temperature bias.

From this, I observe that density differences above the boundary layer are essential for strengthening surface pressure gradients and thereby confirm the second hypothesis introduced earlier. ERA5, with its convective parameterization, maintains density differences well above the boundary layer deep into the free troposphere, where gravity waves help redistribute mass and energy, enabling a greater zonal pressure gradient at the surface. In contrast, Control lacks this vertical density structure, which restrains density contrasts largely to the boundary layer and results in weaker surface pressure gradients. Although Control's boundary layer density structure appears promising and aligns with SST-driven gradients, the absence of convectively driven density gradients above the boundary layer suggests that processes at the air-sea interface may need further examination.

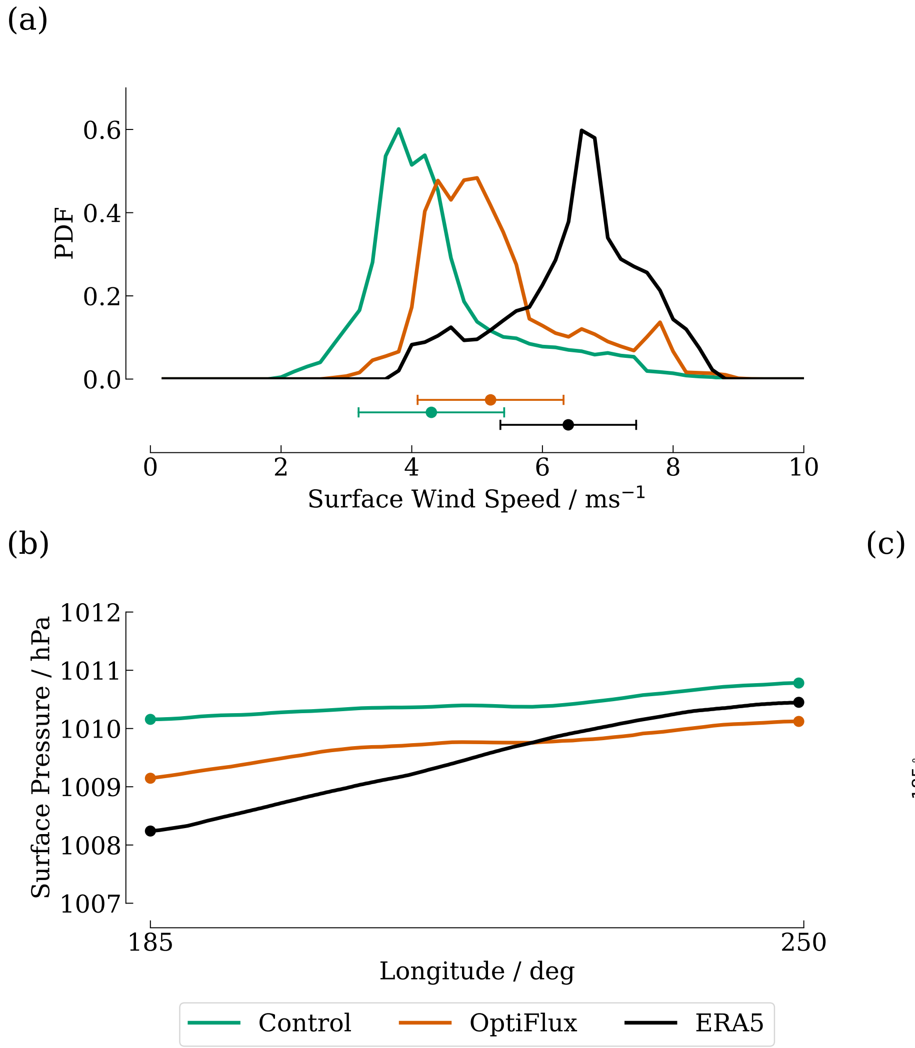

Figure 9: **Winds, Pressure and Pressure Gradient.** Comparison of Control, OptiFlux, and ERA5 data for (a) PDF of spatial mean surface wind speed together with the mean value and the corresponding standard deviation below each distribution, (b) meridional mean of surface pressure, and (c) zonal pressure gradients along 5°S to 5°N, and 185°E to 250°E indicated by the black box in Figure 8 for March 1979.

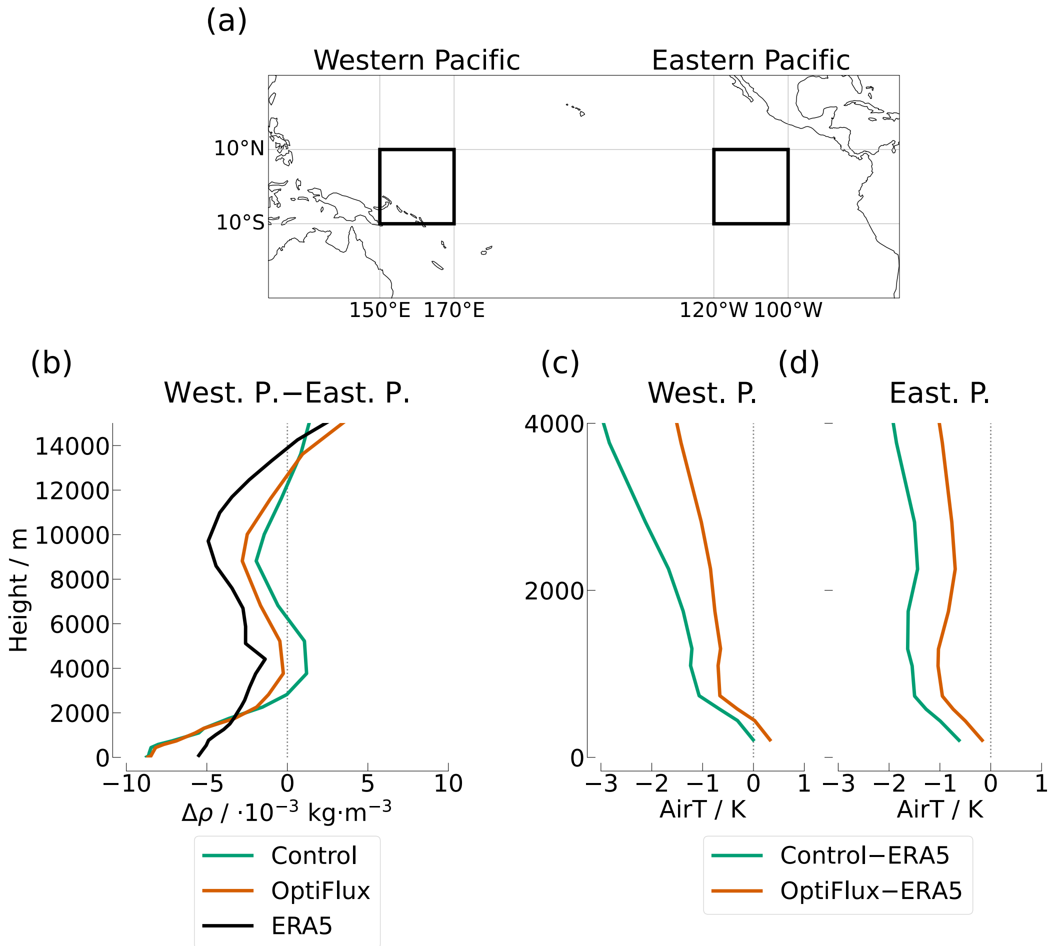

Figure 10: **Vertical Structure of Density and Temperature.** Comparison of Control, OptiFlux, and ERA5 data for (a) western and eastern Pacific regions, (b) vertical profile showing density differences between the western and eastern Pacific, and (c) and (d) vertical profiles over the lower 4000 m displaying the differences between Control and OptiFlux relative to ERA5 for the western Pacific (c) and eastern Pacific (d) in March 1979.

To influence surface pressure gradients, the overlying atmosphere must reflect these gradients in its density differences. While these differences are partly driven by SST, I have shown that deeper density contrasts are vital, as the vertical density profile ultimately determines the surface pressure. I have already shown this relationship in Subsection 2.1.1. Emanuel (1987) introduced the concept of Wind-Induced Surface Heat Exchange (WISHE), a feedback mechanism in which surface winds enhance atmospheric convection by increasing heat and moisture fluxes at the ocean interface. Faster winds intensify this exchange, fueling deeper convection. This is an elementary feedback cycle for tropical cyclones. Building on this concept, I examined how surface heat exchange warms the atmosphere, increasing its capacity to hold moisture, which then rises as warm, moist air. This understanding leads me to investigate the surface flux formulation in ICON, exploring its potential for improvement.

4.2 IMPROVING THE SURFACE FLUX FORMULATION

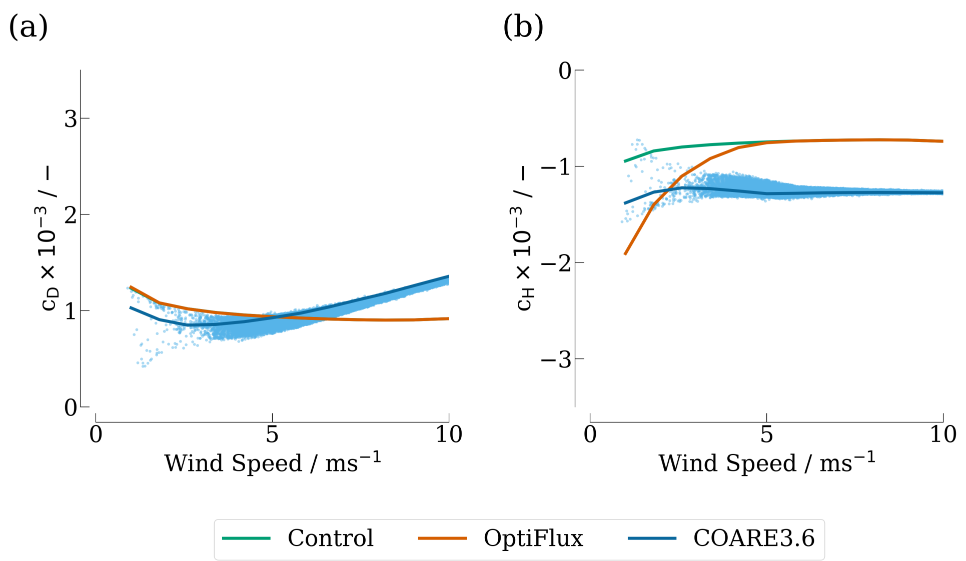

Figure 11: **Momentum and Heat Exchange Coefficients.** Comparison of drag exchange coefficient c_D in panel (a) and heat exchange coefficient c_H in panel (b) against wind speed from Control, OptiFlux, and the COARE algorithm. In (a), Control and OptiFlux are exactly on top of each other.

I revisit TOGA COARE (Tropical Ocean Global Atmosphere - Coupled Ocean-Atmosphere Response Experiment), a major international campaign conducted between November 1992 and February 1993, which was instrumental in advancing our understanding of air-sea interactions in the western Pacific warm pool (Webster and Lukas, 1992). This large-scale effort provided valuable insights into the exchanges of momentum, heat, and moisture at the ocean-atmosphere interface. From this, the COARE3.6 algorithm (hereafter COARE) was developed, becoming one of the most trusted tools for accurately representing surface fluxes, particularly in tropical regions (Fairall et al., 1996a; Fairall et al., 1996c; Fairall et al., 1997; Fairall et al., 2003; Fairall et al., 2011; Edson et al., 2013). While COARE is not currently implemented in the ICON model, I initialize COARE using ICON output to evaluate how this could improve ICON and help identify current limitations.

Figure 11 compares in panel (a) the drag coefficient (c_D) of the Control simulation with the COARE algorithm. Around $5\,\mathrm{m\,s^{-1}}$ wind speed, Control and COARE agree. For lower speeds, Control assumes too high values for the drag coefficient and for speeds greater than $5\,\mathrm{m\,s^{-1}}$, Control assumes too low values. Panel (b) reveals a about 50 % greater heat exchange coefficient (c_H) in COARE compared to the Control simulation which confirms my first hypothesis raised in Section 4.1. This underestimation of c_H limits heat transfer between the ocean and atmosphere, resulting in weaker pressure gradients and therefore surface winds. This explains why, despite nearly identical SSTs in the Control simulation and ERA5, the surface pressure gradients are not maintained. In the following, I will focus on the underestimation of c_H and not on c_D, as the weak zonal surface pressure gradients appear to stem from a thermodynamic issue.

To address this limitation in surface heat flux, I introduce an experimental setup called OptiFlux, which amplifies c_H by up to three times for wind speeds below $6\,\mathrm{m\,s^{-1}}$, while leaving c_D unchanged. This modification is designed to enhance heat transfer between the ocean and atmosphere, particularly under low-wind conditions typical of the tropical Pacific. Using COARE as a benchmark, I evaluate OptiFlux's performance relative to both the Control simulation and COARE itself.

The results, illustrated in Figure 11, show that OptiFlux improves c_H, bringing it closer to COARE's estimates for wind speeds below $6\,\mathrm{m\,s^{-1}}$. Here, I accept that the qualitative trajectory of the OptiFlux curve in panel (b) deviates from COARE curve due to my changes. The trajectory of Control is qualitatively closer to that of COARE, but I aim to increase the surface heat exchange in the low-wind regimes. Therefore, I will evaluate the influence of these changes on boundary layer winds and atmospheric dynamics in the following section.

4.3 Impact of enhanced heat exchange on atmospheric circulation

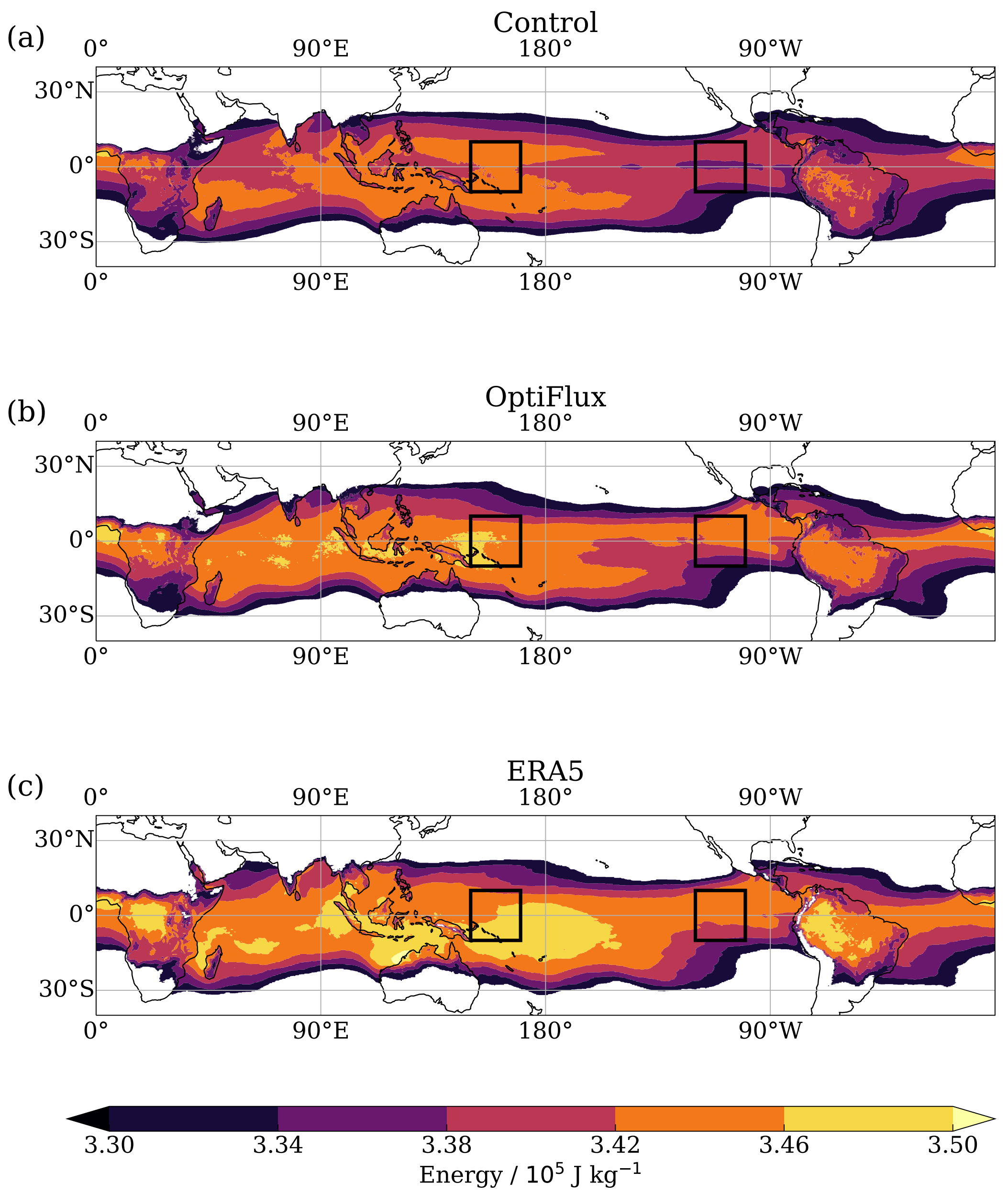

Figure 12: **Tropical Surface Moist Static Energy.** Spatial distribution of surface moist static energy for March 1979, comparing (a) Control, (b) OptiFlux, and (c) ERA5 of the tropics. The black boxes highlight the same regions of interest as in Figure 10 for further analysis in Figure 13.

The increased heat exchange coefficient (c_H) in OptiFlux has a profound impact on both boundary layer winds and the broader atmospheric circulation. I shown in Figure 12 (b), the enhanced heat transfer results in higher surface moist static energy, particularly in the western Pacific. This rise in moist static energy (h) drives more vigorous convection, which efficiently redistributes energy vertically.

OptiFlux brings moist static energy values closer to ERA5, indicating that convection is more effectively triggered than in the Control simulation. Figure 13 shows, that OptiFlux not only raises moist static energy (panels (a), (b)) throughout the atmospheric column but also drives stronger vertical (panels (c), (d)) and zonal wind speeds (panels (e), (f)) in the lower troposphere. In the western Pacific, OptiFlux nearly doubles the zonal wind speed below 7500 m compared to the Control run, as seen in panel (e), and even surpasses ERA5 in some lower layers. These enhanced easterlies, resulting from increased surface heat fluxes, reinforce the dynamic coupling between surface and atmospheric processes.

Further up in the atmosphere, the impact of OptiFlux becomes more pronounced. In panel (f), the zonal winds above 7500 m are stronger in OptiFlux than in Control, with a clear transition to westerlies aloft, aligning closely with ERA5. In contrast, the winds in Control nearly disappear at higher altitudes. This indicates that OptiFlux strengthens the easterlies in the boundary layer while supporting stronger westerly winds in the higher troposphere, creating a more dynamic overturning circulation that is essential for maintaining large-scale atmospheric balance.

These changes in wind patterns extend across the entire Pacific basin. Coming back to Figure 10, I learn from panel (b) that the gradient between eastern and western Pacific in the vertical density profile for OptiFlux has increased towards ERA5. This enhanced density gradient translates into a stronger east-west pressure gradient, as seen in Figure 13 (g), which intensifies the easterlies in the lower troposphere. OptiFlux indicates that the improvement in the pressure gradient is directly tied to the adjustments made to c_H emphasizing the tight connection between surface fluxes and both local and large-scale wind patterns.

In conclusion, my adjustments to c_H in OptiFlux demonstrate how small-scale changes at the air-sea interface can enhance both boundary layer dynamics and larger-scale circulation. Drawing on the WISHE concept of Emanuel (1987), I showed that an increased surface heat flux sustains density gradients deeper into the atmosphere. In convective areas, air density is generally lower than in non-convective areas at the same altitude. On the one hand, this occurs because latent heat released during condensation warms the air, reducing its density. On the other hand, warmer air at the surface is able to absorb more moisture, promoting upward motion. The lower density of water vapor compared to dry air further drives buoyancy, sustaining convection. In contrast, non-convective areas, lacking these processes, typically exhibit higher density at similar altitudes. Gravity waves generated by convection redistribute mass and energy in the free troposphere, reducing thermodynamic differences but creating stronger pressure gradients between convective and non-convective areas. Ultimately, this translates into more robust surface winds driven by the pressure gradient force. With this, I draw attention to how surface heat flux parameterization is key to driving surface pressure and surface winds as part of tropical atmospheric dynamics in climate models.

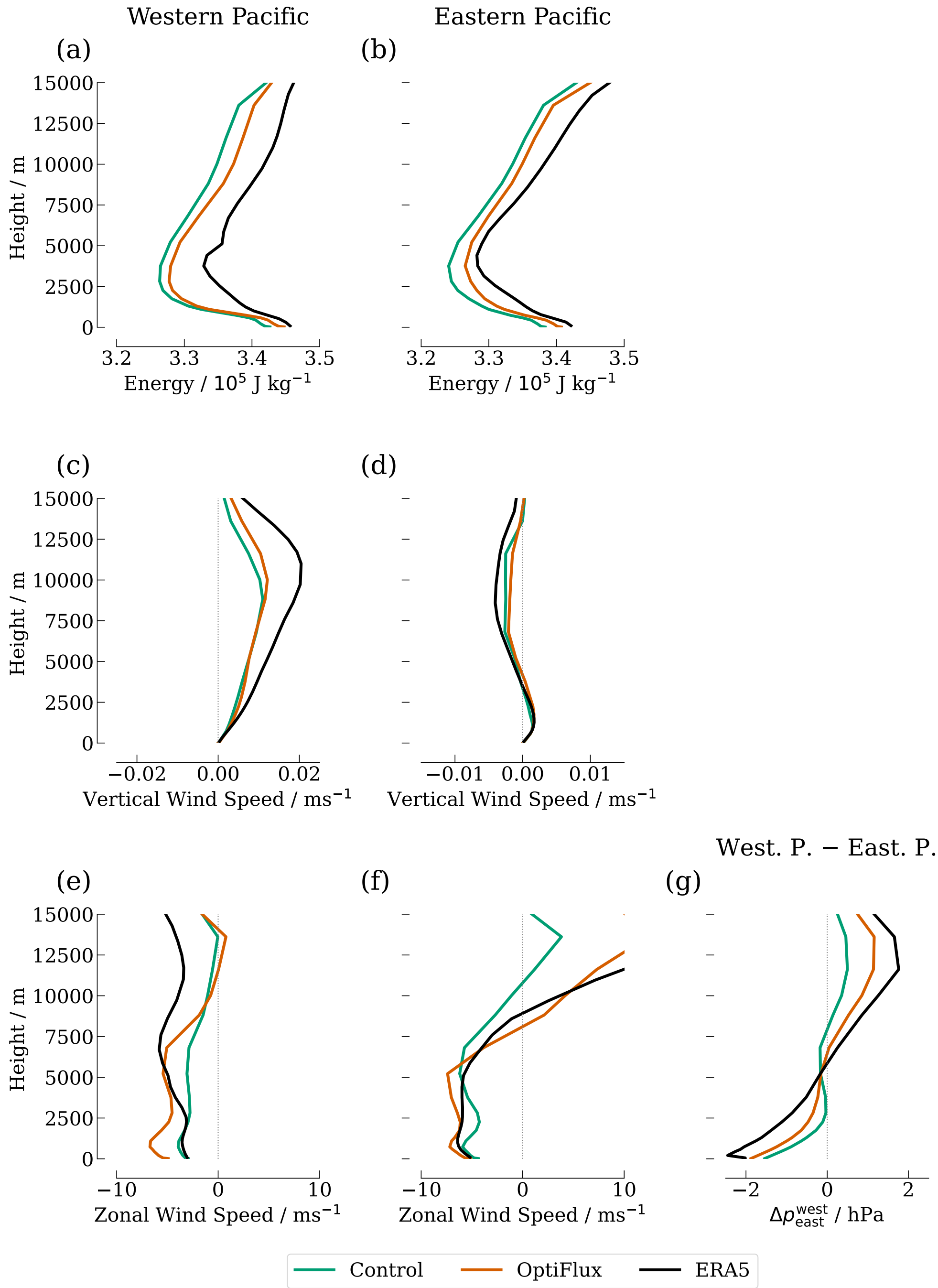

Figure 13: **Vertical Profiles.** March 1979, comparing (a) and (b) moist static energy, (c) and (d) vertical wind speed (note the different x-axis limits), (e) and (f) zonal wind speed, and (g) the pressure difference between the spatial mean pressure of the western and eastern Pacific. The left column presents profiles from the western Pacific, and the center column from the eastern Pacific, as outlined by the black boxes in Figure 12.

5 CONCLUSIONS

While the overarching question posed in the motivation (c.f. Chapter 1) "How do interactions between the atmosphere and ocean influence boundary layer dynamics?" is too broad to claim a complete answer, I was able to address the two sub-questions with greater precision.

5.1 DID I ANSWER THE RESEARCH QUESTIONS?

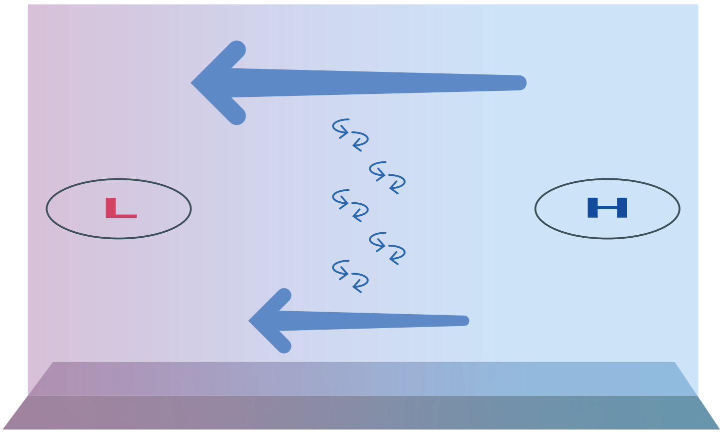

Figure 14: **Drivers of the Boundary Layer Winds.** SST imprints its temperature distribution on the boundary layer, creating low pressure ("L") over warm SST and high pressure ("H") over cooler areas. The pressure gradient force drives winds (bold, straight arrows) from high to low pressure, while horizontal and vertical momentum transport (small, curly arrows) help maintain the wind balance.

What Drives Equatorial Boundary Layer Winds?

Equatorial boundary layer winds are driven by a combination of sea surface temperature (SST)-induced pressure gradients, free tropospheric influence, and horizontal and vertical momentum transport within the boundary layer, as schematically illustrated in Figure 14. My study builds upon foundational research, particularly the work by Lindzen and Nigam (1987), which introduced the relationship between SST gradients and surface pressure variations, by Deser (1993), which refined the Rayleigh Friction Model (RFM) to better capture ocean surface winds, and by Stevens et al. (2002) , which highlighted the role of free tropospheric winds in influencing surface dynamics. My work extends the understanding of boundary layer winds by conducting a rigorous momentum budget analysis of the boundary layer using the storm-resolving model ICON at kilometer-scale. This approach quantifies the key processes shaping boundary layer winds forming the equatorial wind patterns, including a precise definition of boundary layer height based on vertical turbulent fluxes—an advancement not previously achieved. Additionally, I employed the Lindzen and Nigam (1987) approach to compute boundary layer winds from SST-driven surface pressure, demonstrating its effectiveness in reproducing the defined wind patterns. My analysis creates a bridge between the Lindzen and Nigam (1987) ansatz, which established the SST-driven pressure mechanism, and the findings of Stevens et al. (2002), who highlighted the role of free tropospheric winds in defining boundary layer dynamics. I confirm the importance of free tropospheric influence and, using the Lindzen and Nigam (1987) framework, propose an improved wind equation that extends beyond the RFM by incorporating the pressure gradient force along with horizontal and vertical transport terms. Finally, I answered the first research question by offering a structured, quantitative perspective on the forces driving equatorial boundary layer winds.

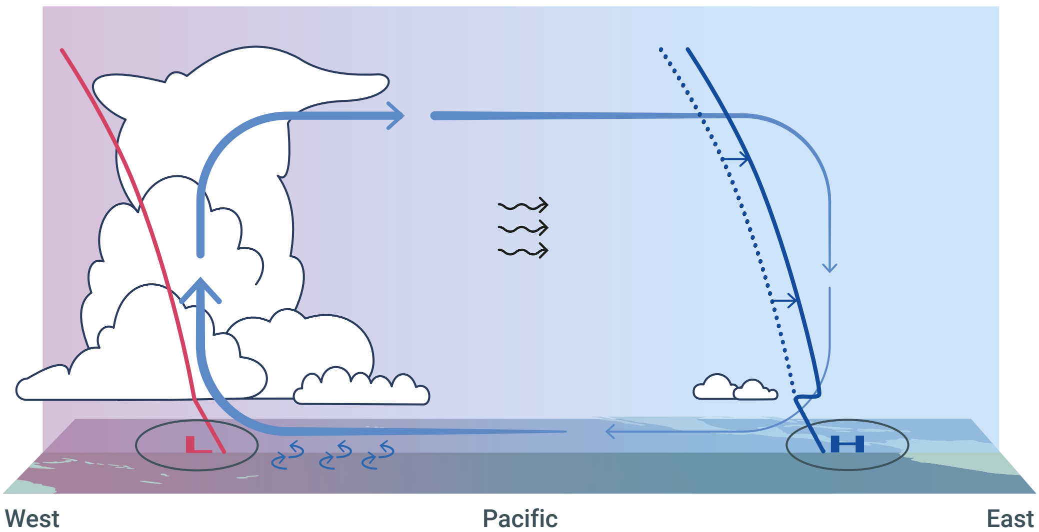

Figure 15: **Surface Heat Flux Revives the Surface Pressure: An Example.** Surface heat exchange (small, curly arrows, lower left) triggers convection, shifting the vertical temperature profile (red) toward higher temperatures and lowering the surface pressure ("L"). Gravity waves (black, curly arrows) redistribute mass and energy across the free troposphere, altering temperature profiles (blue) over non-convective areas and reinforcing higher surface pressure ("H") over already cold regions. This process ultimately supports stronger surface winds by enhancing the circulation pattern (blue arrows circularly arranged).

How Do Surface Heat Fluxes Drive Surface Pressure and Boundary Layer Winds?

Surface heat fluxes drive surface pressure gradients and boundary layer winds by modulating moist static energy, triggering convection, and influencing vertical coupling with the free troposphere, as schematically illustrated in Figure 15. Accurately capturing these dynamics, however, remains a challenge in climate models, particularly in low wind regimes over warm oceans with weak temperature and pressure gradients. Kitamura and Ito (2016) highlights these challenges, noting that in low wind scenarios dominated by convection, conventional bulk heat flux relations often fail to consistently capture the nuances of surface fluxes.

From my first research question, I understand that pressure gradients are central among the multiple key drivers of surface winds. But an equally critical question arises: what drives these surface pressure gradients? My findings indicate that surface heat fluxes play a foundational role in shaping these gradients and are misrepresented in ICON's parameterizations. I unravel a discrepancy between ICON's fluxes compared to those generated by the standalone COARE3.6 algorithm (Fairall et al., 1996a), developed in the wake of the TOGA COARE field campaign (Webster and Lukas, 1992) to improve accuracy in such low-wind regimes. Recognizing these limitations, I was inspired by the Emanuel (1987) concept of Wind-Induced Surface Heat Exchange (WISHE), which highlights the physical interplay between surface heat fluxes and wind dynamics. Using WISHE as a guiding principle, I develop and test the OptiFlux simulation, enhancing ICON's representation of surface heat fluxes. With this adjustment I increase moist static energy not only at the surface but throughout the vertical column, initiating more vigorous convection and triggering a circulation that redistributes surface pressures, thereby strengthens boundary layer winds. I answer the second research question by demonstrating that surface pressure distribution is not solely driven by SST, as suggested by the Lindzen and Nigam (1987) framework, but also by temperature and density differences in the free troposphere, which are shaped by surface heat fluxes. These fluxes influence air mass distribution aloft, ultimately determining surface pressure gradients and driving boundary layer winds.

5.2 IS THE FUTURE STORM-RESOLVING?

Storm-resolving models of kilometer scale have become increasingly relevant in climate science, addressing the limitations of traditional coarse-resolution models, especially in representing oceanic, atmospheric, and terrestrial interactions. As Randall et al. (2003) highlight, the persistent challenges in parameterizing processes like convection, turbulence, and cloud formation introduce uncertainties that can hinder accurate simulations. Ultimately, models with finer spatial scales directly resolve these fine-scale dynamics—eliminating the need for many parameterizations and allowing for explicit representation of processes critical to boundary layer winds and surface fluxes.

In Chapter 3, I use output with high spatial detail capturing vertical and horizontal advection—key drivers of boundary layer winds that could not be resolved at coarser scales. This study would have been infeasible without this capability, as it enables me to uncover momentum exchanges that traditional models could not capture. Previous studies, based on their model resolution, were unable to resolve the small-scale contribution of advection. In contrast, the ICON model reveals that this previously unresolved advection is a wind-driving force of the same order of magnitude as the pressure gradient, crucial for understanding the mechanisms driving equatorial winds. This level of detail underscores the vital role of kilometer-scale modeling in advancing the analysis of momentum dynamics in boundary layer winds.

In Chapter 4, I highlight the necessity of using fine resolution to accurately capture surface fluxes—momentum and heat exchanges critical for atmospheric stability. Observational data, such as from a single ocean buoy, cannot provide both high spatial and temporal resolution simultaneously, making detailed modeling essential for broader coverage. This level of resolution is crucial for examining how variations in surface fluxes impact convection and pressure distribution, emphasizing that fine-scale modeling is pivotal for uncovering the underlying dynamics.

However, kilometer-scale storm-resolving models come with their own set of challenges. The computational demands are large, often requiring high-performance computing (HPC) platforms to operate effectively, which limits accessibility to well-resourced research groups. Both Rackow et al. (2024) and Hohenegger et al. (2023) note that these models necessitate enormous data storage and processing capacities, complicating long-term and multi-decadal climate projections. Ironically, the energy-intensive nature of HPC systems, sometimes even dependent on non-renewable sources, contrasts with their purpose of addressing climate change. This paradox reinforces the need for more scalable, energy-efficient solutions to make high-resolution modeling sustainable and accessible to a broader community.

In conclusion, while storm-resolving models of kilometer scale represent a promising future for climate science, their effectiveness hinges on accessibility and usability. For these models to become a standard tool, they must be made available to a broader spectrum of researchers, supported by improvements in user interfaces and computational efficiency (Stevens et al., 2024). Further advancements in spatial and temporal precision are pivotal; studies like mine demonstrate the scientific value of these capabilities. Reducing computational costs would also be possible with increased investment in developer support, energy-efficient hardware, and wider access to GPU-based systems already in use for other high-priority applications. Addressing climate change requires societal backing to channel resources into refining storm-resolving models of kilometer scale for precise, scalable forecasting, allowing this technology to reach its full potential in climate science.

5.3 OUTLOOK AND OPEN QUESTIONS

5.3.1 *Low-Hanging Fruit 1: Comparison with Observational Data*

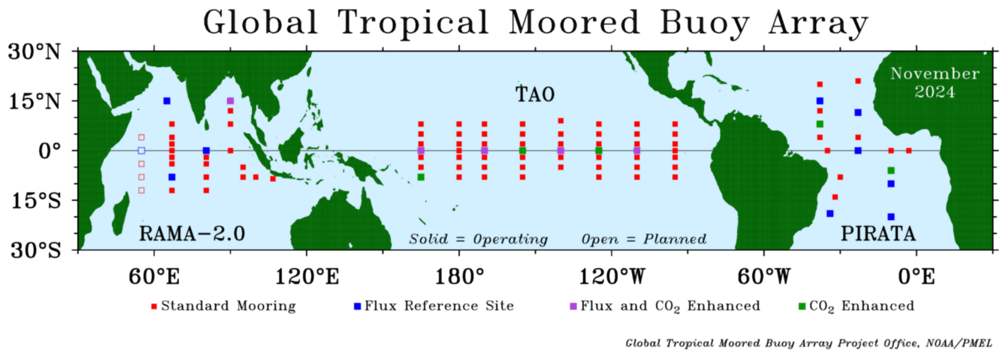

Figure 16: **Global Tropical Moored Buoy Array.** The tropical moored buoy system's distribution across the ocean basins, with different colors representing various mooring types equipped with distinct measuring devices. (Source: http://www.pmel.noaa.gov/tao/oceansites/images/map_lg.gif)

An accessible next step building on my dissertation is the comparison with observational data. Data from buoy arrays along the equatorial oceans as illustrated in Figure 16, such as TAO/TRITON (*Tropical Atmosphere Ocean/Triangle Trans-Ocean Buoy Network*, McPhaden et al. (2010)), PIRATA (Prediction and Research Moored Array in the Tropical Atlantic, Bourlès et al. (2008) and Bourlès et al. (2019)), and RAMA (*Research Moored Array for African-Asian-Australian Monsoon Analysis and Prediction*, (McPhaden et al., 2009)), provide a valuable opportunity for such comparisons. Additionally, the 811 radiosondes launched during EUREC^{4}A in boreal winter 2020 (Stephan et al., 2021), and another 621 during ORCESTRA in boreal summer 2024 (Winkler et al, 2025, *in preparation*) from Barbados and the tropical Atlantic, offer a rich sounding dataset. Radiosondes, which can travel up to 94 km (Stephan et al., 2021) depending on wind conditions, measure pressure, temperature, humidity, wind speed, and wind direction during both ascent and descent. By combining surface temperature and pressure data from their trajectories, it would be possible to test whether the much-mentioned Lindzen and Nigam (1987) ansatz for surface wind prediction can be validated using observational data.

5.3.2 *Low-Hanging Fruit 2: Coupled vs. Atmosphere-only*

Figure 17 reproduces panel (a) from Figure 9 and includes the PDF of the spatial mean surface wind of the respective area from an ocean-atmosphere-land coupled ICON simulation ("Coupled"). The PDF for the Coupled simulation is much flatter and it achieves higher wind speeds comparable to those of ERA5. The mean surface wind across the equatorial area is higher than both the Control and the tuned OptiFlux experiments. The zonal surface pressure gradient (not shown

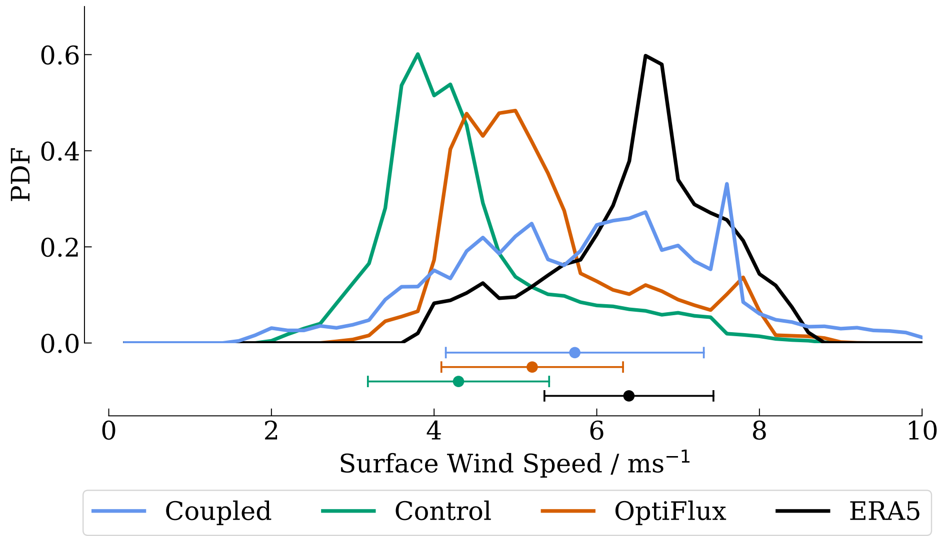

Figure 17: **PDF of Equatorial Winds.** Comparison of a Coupled ICON simulation to Control, OptiFlux, and ERA5 data for the PDF of spatial mean surface wind speed together with the mean value and the corresponding standard deviation below each distribution along 5°S to 5°N, and 185°E to 250°E indicated by the black box in Figure 8.

here) is greater in Coupled than in Control or OptiFlux, despite the atmosphere-land configuration being identical to that of the Control simulation. This suggests that the dynamically interacting ocean in the Coupled simulation partially compensates for the weak zonal surface pressure gradient, enabling stronger surface winds. It is essential in climate modeling to ensure that each component of an Earth system model (ocean, land, atmosphere) is independently realistic. Comparative experiments between coupled and non-coupled simulations, including adjustments to surface flux parameterizations, offer valuable insights into the interplay of the Earth system components towards improving the reliability of Earth system models.

5.3.3 *A Tough Nut: Decoding the SST Distribution*

In this dissertation, I explored the challenging dynamics of equatorial boundary layer winds. Yet, throughout all chapters, the question of what controls the surface pressure distribution has been a constant theme, serving as one centerpiece of the second research question in Chapter 4. The ocean imprints its sea surface temperature (SST) distribution onto the atmosphere aloft, manifesting as surface pressure patterns. Studies such as Lindzen and Nigam (1987), Stevens et al. (2002), Back and Bretherton (2009), Seager et al. (2019), and Williams et al. (2023) have directly linked SST distribution to atmospheric responses, influencing surface winds, convergence, greenhouse gas concentrations, and overturning circulations. My analysis demonstrate that atmospheric pressure gradients, shaped by SST-driven surface pressure distributions, control both horizontal and vertical winds. Examining the four terms on the right-hand side of the wind momentum Equation (1), reveals that the pressure gradient appears either explicitly or implicitly in the wind components u, v, and w, all of which are influenced by the pressure gradient force. The SST strongly affects the overlying atmosphere and I treated them as a given boundary condition in this dissertation. Overall, this raises another fundamental question: What drives the tropical sea surface temperature?

The equatorial air-sea interface is especially powerful: here, wind stress and the Earth's rotation generate equatorial upwelling (Hidaka, 1937). In case of a shallow thermocline the rise of cool, subsurface water becomes very efficient (Wang et al., 2017; Ford et al., 2012). These cool water masses sustain the east-west temperature gradient that shapes the equatorial cold tongue (Bjerknes, 1966), an elementary component linking oceanic and atmospheric dynamics in the equatorial zone. The Zebiak-Cane ocean-atmosphere model (Zebiak and Cane, 1987) offers a simple yet powerful framework to explore these interactions and could serve as a baseline of our understanding of air-sea coupling at the equator in sophisticated global coupled storm-resolving models.

Climate change has the potential to weaken these east-west SST gradients, which would disrupt the Walker circulation—a fundamental component in driving equatorial upwelling and sustaining the cold tongue in the eastern Pacific. Kang et al. (2023) show that warming in the Southern Ocean, coupled with changes in atmospheric CO_2, reduces the zonal temperature gradient, shifting the Pacific towards an El Niño–like state with weakened upwelling. Watanabe et al. (2024) explain how altered SST patterns and feedbacks could amplify variability in future projections. Currently, climate models fail to predict the observed changes in equatorial SST (Wills et al., 2022), which undermines the confidence in much needed climate projections for the Pacific region and beyond.

Given these points and the findings of my dissertation, the equatorial SST distribution and its impact on surface pressure and boundary layer winds reveal a multifaceted and intricate relationship. In the context of climate change, climate models demand rigorous refinement and careful scrutiny, with the integration of high-quality observational data playing a key role in improving model accuracy. At the equator, as a sensitive and critical zone in Earth's climate system, air-sea interaction demands continued attention.

5.4 final remarks

Herr: es ist Zeit. Der Sommer war sehr groß.
Leg deinen Schatten auf die Sonnenuhren,
und auf den Fluren laß die Winde los.

Befiehl den letzten Früchten voll zu sein;
gieb ihnen noch zwei südlichere Tage,
dränge sie zur Vollendung hin und jage
die letzte Süße in den schweren Wein.

Wer jetzt kein Haus hat, baut sich keines mehr.
Wer jetzt allein ist, wird es lange bleiben,
wird wachen, lesen, lange Briefe schreiben
und wird in den Alleen hin und her
unruhig wandern, wenn die Blätter treiben.

— *Herbsttag, (Rilke, 1902)*

As Rilke's *Herbsttag* brings forth the image of seasons ripening to their close, this dissertation, too, brings a stage of growth in our understanding of boundary layer winds. Just as the poem urges the last sweetness into the wine, my research has aimed to "ripen" knowledge of how ocean-atmosphere surface interactions contribute to wind dynamics, adding depth to an evolving field. Yet, like the restless wanderer, I conclude with the recognition that much remains to be discovered. This work is but a step along a path that continues to unfold, inviting further exploration into the intricate processes that shape our atmosphere.

Part II

APPENDIX

A
UNCOVERING THE DRIVERS OF THE EQUATORIAL OCEAN SURFACE WINDS

The work in this appendix has been submitted as:

Winkler, M., Koelling, T., Mellado, J.P., Stevens, B. (2024a): "Uncovering the Drivers of the Equatorial Ocean Surface Winds", In: *review at Quarterly Journal of the Royal Meteorological Society*

A.1 ABSTRACT

Uncovering the Drivers of the Equatorial Ocean Surface Winds

Marius Winkler[1,2], Tobias Koelling[1], Juan Pedro Mellado[3], Bjorn Stevens[1]

[1]Max-Planck-Institut für Meteorologie, Hamburg, Germany
[2]International Max Planck Research School on Earth System Modelling, Max-Planck-Institut für Meteorologie, Hamburg, Germany
[3]Universität Hamburg, Meteorologisches Institut, Hamburg, Germany

A.1 ABSTRACT

We investigate the prevailing equatorial ocean surface winds and their underlying mechanisms using data from the coupled storm-resolving ICON model at 5 km horizontal grid spacing. We identify and analyze two distinct wind patterns: the Zonal Wind Pattern, characterized by trade-wind-like winds parallel to the equator, and the Meridional Wind Pattern, with winds perpendicular to the equator. An analysis of the boundary layer momentum budget demonstrates that both wind patterns are driven by either the zonal or meridional pressure gradient force. While the Meridional Wind Pattern is weakened, the Zonal Wind Pattern is reinforced by vertical turbulent flux and horizontal transport of momentum.

Differing from prior studies, we develop a wind model tailored to the two prevailing equatorial wind patterns, which interact with the sea surface temperature. We introduce a scaling factor for the proportionality between the sum of the horizontal advection force with the vertical turbulent flux and the pressure gradient force, which yields correspondence with the ICON reference winds.

The equatorial surface wind patterns are coupled to the equatorial sea surface temperature gradient. We illuminate this coupling and derive the hydrostatic atmospheric surface pressure using a SST driven parameterization for the temperature profiles. We use this hydrostatically calculated surface pressure derived from sea surface temperature for the developed wind model developed in this study and establish a direct link between sea surface temperature and surface winds.

KEYWORDS

Equatorial Ocean Surface Winds, Momentum Analysis, Air Sea Interaction, Atmospheric Boundary Layer, Global Storm-Resolving Models

A.2 INTRODUCTION

Surface winds are a complex phenomenon and are essential in mediating exchange of momentum, matter, and energy at Earth's surface. At the nexus between the atmosphere and the ocean they drive ocean currents, the distribution of energy, influence weather patterns, and thereby profoundly impact the planet's climate system. Determining their main controlling factor has a long history, here we revisit this question using newly available information from coupled km-scale global climate simulations.

At the equator over the ocean, surface winds are closely coupled to the distribution of mass and energy in the atmosphere, and the temperature structure of the ocean (Xie, 2004). The zonal component of the surface winds is the cause of a zonal transport of water masses from east to west. The surface winds affect the temperature distribution of the sea surface and the depth of the thermocline (Richter and Doi, 2019), which is deeper in the western part of the ocean basin and shallower in the eastern part (Fahrbach and Bauerfeind, 1982; Yang and Wang, 2009). Another effect of the zonal momentum exchange from surface winds to surface current is equatorial upwelling (Hidaka, 1937). On the equator, surface winds drive upwelling to balance off-equatorial Ekman transport. As a result, colder deeper water is drawn to the surface. Effects of this upwelling, for instance on the thermal structure or nutrient provision of the upper ocean, are enhanced in the eastern ocean basin by the shallow thermocline. Both processes, the transport of warm water from east to west and the increased equatorial upwelling in the east are driven by surface winds and result in an east-west gradient of sea surface temperature (SST) within the Pacific and the Atlantic (Cromwell, 1953; Wyrtki, 1981; Chun, 1902; Molinari et al., 1986).

Lindzen and Nigam (1987), hereafter LN, propose that surface winds are primarily driven by atmospheric boundary layer (ABL) pressure gradients, and hence the atmospheric mass field, which is imprinted by the SST. Assuming that surface temperature differences are confined to a shallow boundary layer, LN proposed a model of a three-dimensional pressure field based on SST, from which they subsequently derived a wind equation that balanced the Coriolis force, pressure gradient force, and parameterized surface drag. This wind model is named Rayleigh Friction Model (RFM), since the force balance is related to the wind by parameterizing surface drag as proportional to the wind, which is called Rayleigh drag. Wallace et al. (1989) and Deser (1993) use the RFM for wind fields in the tropical Pacific. Based on observational data, Deser (1993) introduced an adhoc change to the RFM to allow for an anisotropic RFM, namely by allowing the Rayleigh friction term, ϵ, to vary with the direction of the wind. Stevens et al. (2002) argued that this unphysical aspect of the RFM is needed to compensate for missing terms in the momentum budget. By including vertical momentum mixing in a bulk model they were able to better, and more physically describe the pattern of near surface winds (Stevens et al., 2002; Richter et al., 2014). Subsequent work, e.g. by Okumura and Xie (2004) extended this approach by accounting for meridional advection of zonal winds. These analyses suggest that horizontal and vertical transport of momentum are crucial for maintaining surface winds at the equator. A comprehensive analysis of the force balance governing the boundary layer winds, however, remains lacking.

We focus on the equatorial ocean surface winds starting from a momentum analysis (Helfer et al., 2021; Nuijens et al., 2022). We approach this question by adopting the MLM framework used by Stevens et al. (2002), as it links the mean force balance in the atmospheric boundary layer to the wind, by parameterizing the surface drag in terms of the ABL (or bulk) wind. The ABL is bounded by the ocean from below and the free troposphere from above, which act as boundary conditions on the atmospheric dynamics within the ABL. By assuming that the mean wind is proportional to the surface drag, we can calculate the momentum

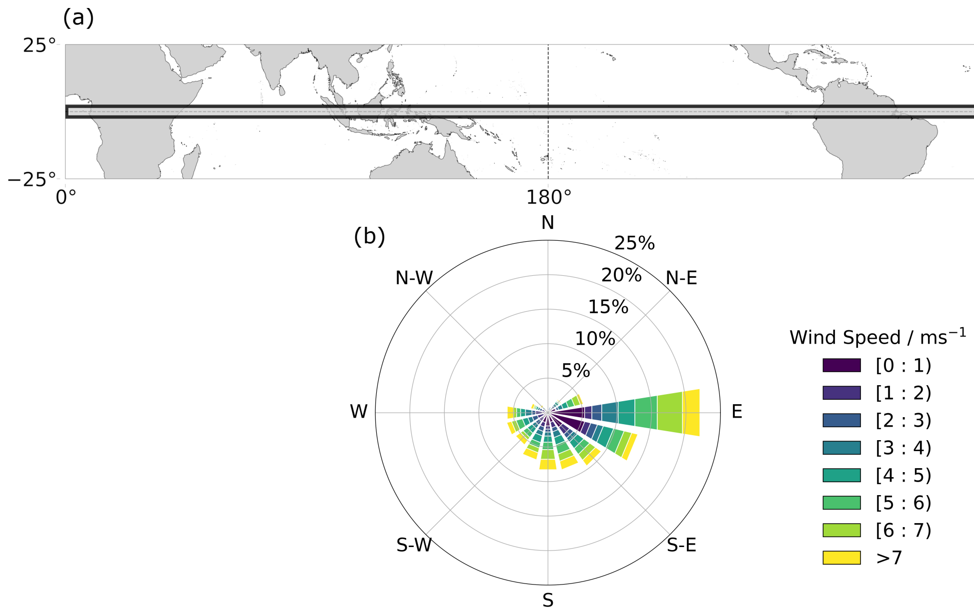

Figure A.1: **Equatorial Ocean Winds.** The box in panel a, outlined in black indicates the equatorial region across the globe that we consider in a first step. We highlight the global surface winds within an equatorial band from $-2°$ - $2°$ latitude. The wind rose (b), shows the monthly means over a two-year period of the surface winds.

balance within the ABL for a region of interest and identify the components that make up the winds for the corresponding region and time window. This study takes advantage of newly available km-scale global ocean-atmosphere coupled models, which allow us to resolve the wind fields and force balances along the equator, even if vertical momentum transport in the boundary layer remains parameterized in such models (Hohenegger et al., 2023). The simulations capture the small scale imprint of low-pressure systems on surface fluxes, the breaking of tropical instability waves with the development of secondary SST fronts and lead to a more realistic representation of atmospheric transport processes.

In this study, we introduce the coupled storm-resolving simulations in Section A.3, which we use for our analysis. Then, we take a step back and examine the prevailing equatorial wind regimes in Section A.4. We identify two different wind regimes that prevail at the equatorial ocean surfaces. We separately apply a detailed momentum analysis to these two wind regimes in Section A.5. Based on this, we can venture into an approach in Section A.6 to calculate the surface pressure from the SST. In Section A.7 we review the theoretical implications of the equatorial force balance and the reasons behind the failure of the RFM. Conclusions from our study are presented in Section A.8.

A.3 DATA DESCRIPTION

We analyze simulations from a atmosphere-ocean-coupled ICON (ICOsahedral Nonhydrostatic) configuration. The ICON Earth-system model is described by Hohenegger et al. (2023) and the simulations we analyze employ a grid spacing of 5 km (G_AO_5km configuration) and 90 vertical levels in the atmosphere, 128 levels in the ocean and five horizontal soil layers. The simulation is started using the Integrated Forecasting System analysis from 20 January 2020, and is run until 28 February 2022. ICON follows the DYAMOND2 protocol (Stevens et al., 2019) as applied during the collaborative European project NextGEMS (Next Generation Earth Modelling Systems, https://nextgems-h2020.eu/).

We extract from the ICON output the pressure, p, the zonal and meridional wind, u and v, the surface drag, $\tau(0)$, the density of the air, ρ, the air temperature, T, and the SST, T_{SST}. The three-dimensional fields of p, ρ, T, u and v are available as snapshots with a 6 h temporal resolution. The two-dimensional fields T_{SST} and $\tau(0)$ are available as snapshots in $\Delta t = 1$ h and $\Delta t = 30$ min, respectively. For the following calculations, we take different time averages for different purposes. We compute monthly means of the wind fields u and v to study equatorial wind patterns and the seasonal momentum budget is calculated from the high-frequency state variables and its mean balance is analyzed.

A.4 EQUATORIAL WIND REGIMES

In a first step, we characterize equatorial wind regimes in the simulation, to define major wind regimes. For this purpose, we focus on the equatorial region within a latitude band from $-2°$ - $2°$ latitude shown in Figure A.1a. Within this region containing land and ocean, we calculate monthly means over a two-year period of the zonal and meridional wind components, compute the corresponding wind vectors, and plot them within a wind rose in Figure A.1b.

About two thirds of the time (63 %) the dominant component of the wind is zonal, 37 % of the time the dominant component is meridional. The wind rose (Figure A.1b) indicates that the largest fraction of the winds are easterlies, which are blowing trade wind-like parallel to the equator but also that winds blow from west to east as westerlies, opposite to the dominant easterlies. Wind reversals appear in the equatorial east Atlantic (Schott and McCreary, 2001) and in the equatorial Indian Ocean where they are a signature of monsoon circulations. We note that southward winds make up the smallest fraction of the total wind, and that northward winds are more likely to cross the equator. This can be related to the Inter-Tropical Convergence Zone (ITCZ) tending to lie north of the equator (Riehl, 1954; Philander et al., 1996).

In addition to the monthly means, we look into daily variability of the surface winds. Therefore, we assess surface wind regimes in the global equatorial window by calculating daily wind vectors. Based on its direction, we assign the wind direction to one of 8 sectors. We distinguish between the east-west, *Zonal Wind Pattern* and the north-south, *Meridional Wind Pattern*. Where the east-west window is divided into two segments respectively from $240° - 300°$ and from $60° - 120°$, and the north-south window is divided into two segments ranging from $330° - 30°$ and $150° - 210°$. To provide a clearer signal, we exclude a total of four $30°$ segments between the aforementioned windows, which serve as transitional areas and are not considered in more detail in the following analysis. We assign each direction vector obtained per grid cell in the corresponding ocean basin to either the east-west (Zonal Wind Pattern) or north-south (Meridional Wind Pattern) win-

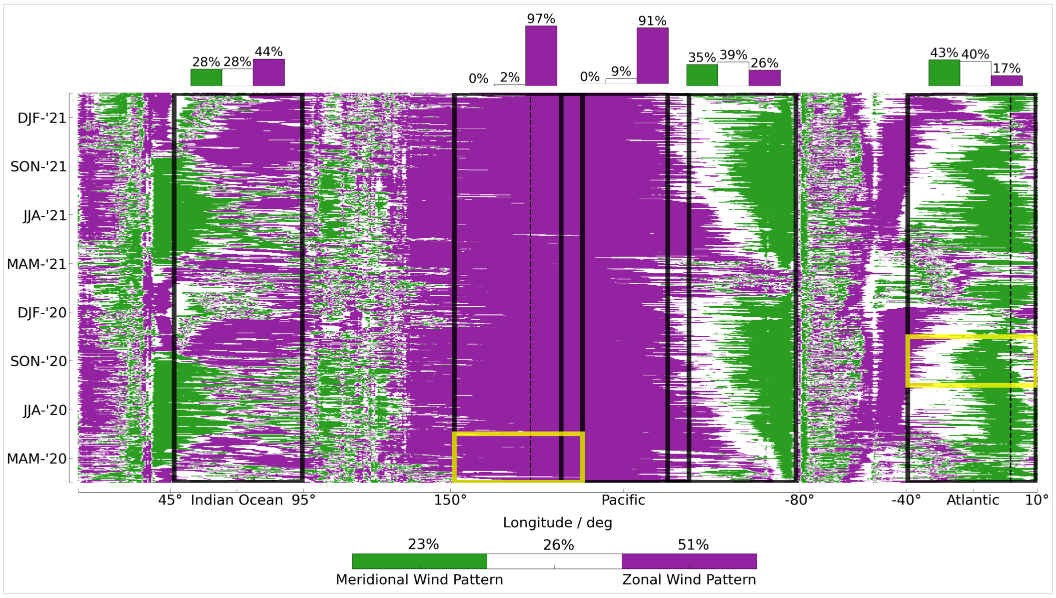

Figure A.2: **Wind Patterns along the Equator.** Shown are daily mean wind patterns along the globe as a meridional mean along $-2°$ - $2°$ latitude, land cells included, from a two-year ICON simulation. Five ocean basins are shown in black. Yellow boxes outline the seasons and ocean basins, which are explored in more detail in the further analysis. Green represents the Meridional Wind Pattern, purple the Zonal Wind Pattern. The transition from one regime to the other is shown in white. On top of the colorbar at the bottom of the plot, the global percentages of the respective wind regime are given. On top of each ocean basin, framed in black boxes, we show histograms showing the distribution of wind regimes for the corresponding ocean basin.

dow and calculate the corresponding distribution to determine the wind regime. Figure A.2 shows the wind patterns along the globe as a meridional mean along $-2°$ to $2°$. This analysis shows that the equatorial winds over the open ocean can be characterized as falling into one of two persistent patterns. Over land we see areas of highly variable coloration. The Zonal Wind Pattern dominates in the western and central Pacific, the Atlantic is predominantly subject to the Meridional Wind Pattern. In the eastern Pacific we observe a split between the Meridional Wind Pattern in the eastern part of the basin and the Zonal Wind Pattern in the western part of the basin. The strongest seasonality is evident over the Indian Ocean with the Zonal Wind Pattern (purple) peaking during DJF and the Meridional Wind Pattern (green) peaking during JJA.

We exclude land areas in the upcoming analysis and focus on the five selected ocean basins of $50°$ longitudinal extent from the global equatorial band spanning $\pm 2°$ on either side of the equator. The basins are defined to contain as few land cells as possible. Thus, the Atlantic Ocean extends from $-40°$ to $10°$, the Indian Ocean from $45°$ to $95°$, the western Pacific from $150°$ to $-160°$, the central Pacific from $-170°$ to $-120°$, and the eastern Pacific from $-130°$ to $-80°$. The ocean basins in the Pacific overlap each other by $10°$. These basins are delineated by the black vertical lines in Figure A.2.

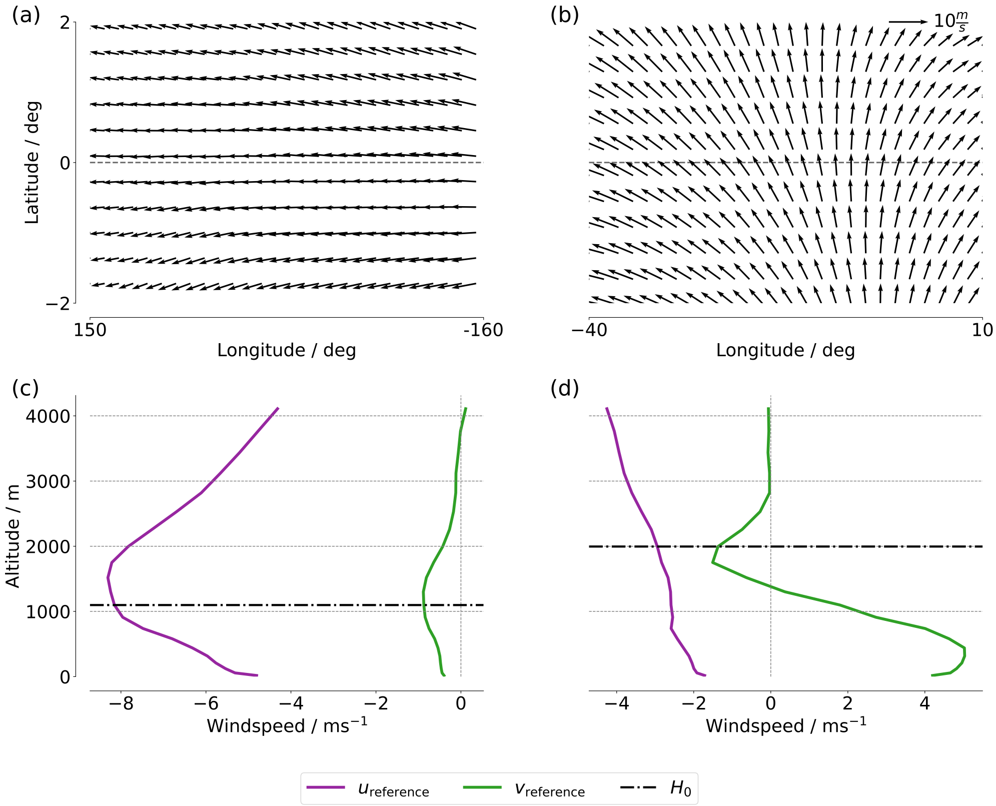

Figure A.3: **Wind Patterns and Profiles over the Equatorial Oceans.** Shown are the surface winds and the vertical wind profiles of the yellow boxes outlined in Figure A.2. The Zonal Wind Pattern in the western Pacific, MAM, 2020 (panel a & c) and the Meridional Wind Pattern in the Atlantic, SON, 2020 (panel b & d). The Zonal Wind Pattern is characterized by a strong zonal flow, which runs almost parallel to the equator. The vertical profile (c) indicates strongest zonal winds just aloft of the ABL (H_0). The Meridional Wind Pattern (b) shows dominant meridional winds crossing the equator. The vertical profile (d) indicates strongest meridional flow within the boundary layer, below the top of the ABL (H_0).

The yellow boxes in Figure A.2 are chosen for more detailed analysis, as they highlight contrasting wind regimes. One box lies in the western Pacific and spans the months of March, April, May (MAM, 2020). The other box lies in the Atlantic and spans the months of September, October, and November (SON, 2020). The box in the western Pacific is 93 % subject to the Zonal Wind Pattern and the box in the Atlantic is 42 % subject to the Meridional Wind Pattern and only 7 % subject to the Zonal Wind Pattern. We compute three-month time means of the surface winds per ocean basin and season and display them in Figure A.3. Subsequent reference to the *Zonal Wind Pattern* refers to the MAM winds of the western Pacific, and reference to the *Meridional Wind Pattern* refers to the SON winds over the Atlantic. Figure A.3 (panel a & c) shows the Zonal Wind Pattern for the western Pacific at the surface (a) and its spatial mean vertical wind profile (c). The Zonal Wind Pattern is defined by a predominantly zonal component. The vertical profile indicates strongest zonal wind just aloft of the ABL (H_0). Figure A.3 (panel b & d) shows an example of the Meridional Wind Pattern in the Atlantic, which is characterized by a dominant meridional wind, which crosses the equator. In the center of the respective ocean basin the wind vectors cross the equator almost perpendicularly. The vertical wind profile (d) illustrates a wall-jet-like meridional flow, which is strongest within the boundary layer, below the top of the ABL.

A.5 MOMENTUM BALANCE IN THE ATMOSPHERIC BOUNDARY LAYER

The analysis of the momentum balance equation allows us to look at the separate terms defining and driving the wind (Stevens et al., 2002; Deser, 1993). Thus, we are able to make a statement about the balance of the corresponding contributions to the wind patterns. In an Eulerian frame of reference the horizontal force balance can be expressed as follows:

$$\begin{aligned}\frac{\partial \overline{u}}{\partial t} &= -\frac{\partial \overline{uu}}{\partial x} - \frac{\partial \overline{uv}}{\partial y} - \frac{\partial \overline{uw}}{\partial z} + f\overline{v} - \frac{1}{\rho}\frac{\partial \overline{p}}{\partial x},\\ \frac{\partial \overline{v}}{\partial t} &= -\frac{\partial \overline{vu}}{\partial x} - \frac{\partial \overline{vv}}{\partial y} - \frac{\partial \overline{vw}}{\partial z} - f\overline{u} - \frac{1}{\rho}\frac{\partial \overline{p}}{\partial y}.\end{aligned} \tag{A.1}$$

The overbars denote three-month seasonal time means. The six terms from left to right are: the tendency, three contributions to the zonal and meridional advection forces, the Coriolis force and the pressure gradient force.

After establishing the momentum equation (Equation (A.1)), we can integrate the momentum equation from the air-sea interface ($z = 0$) to the top of the ABL ($z = H_0$) to obtain the ABL momentum balance. The linearity of the integrals preserves the balance so that we can require that the right-hand side of the equations must be closed in themselves. In doing so, we rearrange as follows:

$$\begin{aligned}0 &= \int_0^{H_0} dz\left[-\frac{\partial \overline{u}}{\partial t} - \frac{\partial \overline{uu}}{\partial x} - \frac{\partial \overline{uv}}{\partial y} + f\overline{v} - \frac{1}{\rho}\frac{\partial \overline{p}}{\partial x}\right] + \tau_u(H_0) - \tau_u(0),\\ 0 &= \int_0^{H_0} dz\left[-\frac{\partial \overline{v}}{\partial t} - \frac{\partial \overline{vu}}{\partial x} - \frac{\partial \overline{vv}}{\partial y} - f\overline{u} - \frac{1}{\rho}\frac{\partial \overline{p}}{\partial y}\right] + \tau_v(H_0) - \tau_v(0).\end{aligned} \tag{A.2}$$

Due to the different magnitude of vertical winds w compared to the horizontal winds u, v we assume that $\overline{uw} = \overline{u'w'} + \overline{u}\;\overline{w} \approx \overline{u'w'}$, so that $\overline{u}\;\overline{w}$ with the time mean of the vertical wind being negligible, hence $w \ll u, v$. The same applies to $\overline{vw} \approx \overline{v'w'}$. We identify the prime terms as the turbulent momentum terms and define: $(\tau_u, \tau_v) = -(\overline{u'w'}, \overline{v'w'})$. If we apply this to Equation (A.1), we obtain $\partial_z(\tau_u, \tau_v)$, which results in the two terms on the right hand side of Equation (A.2), one denoting the divergence of the horizontal momentum flux at H_0 and the other at the surface. The latter denotes the surface drag $\tau_{u,v}(0)$, the former the vertical turbulent flux $\tau_{u,v}(H_0)$, which was the focus of the study by Stevens et al. (2002). We compute the vertical turbulent flux as a residual of Equation (A.1). The surface drag $\tau_{u,v}(0)$ describes the slowing down of the wind through the influence of the water surface. It is the momentum that the atmosphere loses to the ocean. The stronger the wind, the higher the friction and therefore the surface drag.

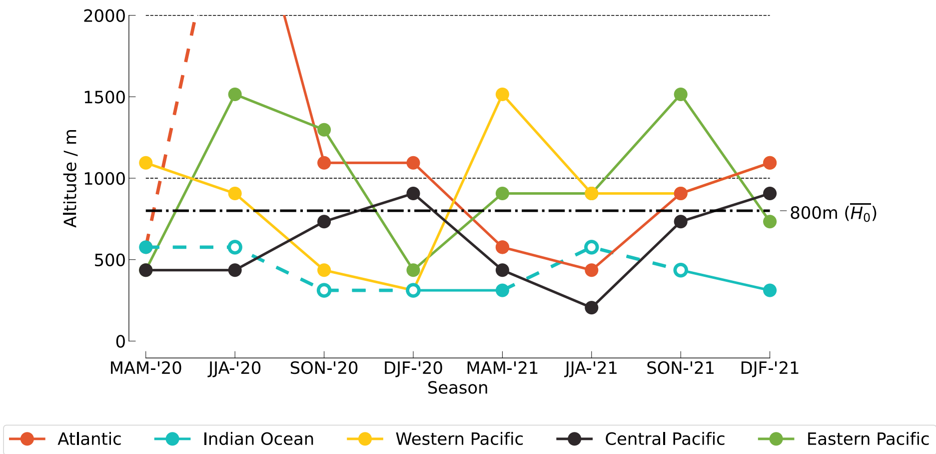

Figure A.4: **Seasonality of the Atmospheric Boundary Layer Height.** We determine the seasonality of the top of the atmospheric boundary layer for the different ocean basins. Solid lines and fully colored dots represent the ABL heights determined via the method described in the text. Dashed lines and white colored dots represent ABL heights that were determined using a different method: we defined an acceptance window of 20 % using a fit along the vertical turbulent flux data and registered the first deviation measured from the sea surface as top of the ABL. The mean ABL height $\overline{H_0}$ over all oceans and seasons is 800 m. 78 % of the determined seasonal ABL heights lie below 1000 m, 22 % lie above.

A.5.1 *Determination of Atmospheric Boundary Layer Height*

Surface winds result from the momentum available within the ABL. Lindzen and Nigam (1987, LN) assume for their work a boundary layer height of 3000 m, so that they can assume a negligible horizontal temperature variability and that the vertical turbulent flux $\tau(h)$ vanishes, which is intended to decouple the free troposphere from the ABL in terms of momentum. However, we do not decouple the free troposphere from the ABL in terms of momentum because we include the vertical turbulent flux as a source or sink of momentum for the surface winds within the ABL.

We define the ABL height as the altitude, at which the vertical turbulent flux up to the next higher model level has changed the least. Therefore, we estimate that the top of the ABL (H_0) lies where the vertical exchange of momentum reaches a minimum. That is equivalent to:

$$\min\left(\frac{\partial\tau}{\partial z}\right) \Rightarrow z = H_0 \tag{A.3}$$

Thus, we aim to separate the well-mixed, convective boundary layer from the overlying free troposphere. We integrate the divergence of the vertical turbulent flux for every grid point from the sea surface to each model level of the ICON simulation and take the horizontal mean. Figure A.4 shows the seasonal behavior of the height of the ABL. We averaged over seasonal time windows and the entire spatial respective ocean basin. The mean ABL height over all oceans and seasons is 800 m with a standard deviation of 340 m. Nuijens et al. (2014) find

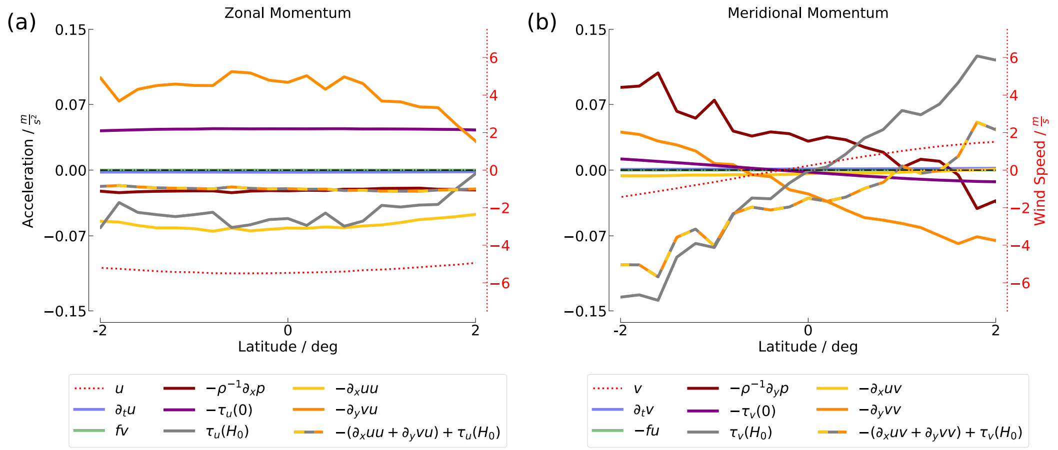

Figure A.5: **Zonal Mean of Momentum Balance, Western Pacific, MAM, 2020.** Shown are the zonal means of the individual terms of Equation (A.2). The yellow-gray-orange zebra lines represent the sum of the horizontal advection forces and vertical turbulent flux at the top of the ABL. The left and right y-axis show different units: the left, solid y-axis represents the range of values of the solid lines of the momentum terms, the right, dotted y-axis refers to the wind speed of the wind field, which is shown dotted in red.

most cloud-base heights close to the lifting condensation level, estimated to be at 700 m ± 150 m, from temperature and humidity measurements at the Barbados Cloud Observatory (BCO) in the North Atlantic trade winds. Albright et al. (2022) use the virtual potential temperature to estimate the mean subcloud-layer height, at 708 m which coincides with the mean lifting condensation level in their analysis. Assuming that the lifting condensation level coincides with the top of the convective boundary layer, we obtain substantial agreement of the averaged ABL heights compared to observational data. Comparing to LN we find that even our highest value (excluding the outlier Atlantic, JJA, 2020) for the ABL height is less than half the 3000 m assumed by LN in their work for the depth of the ABL. LN had to assume an about three times higher ABL to compensate for the missing terms of the momentum balance, which we incorporate in our analysis.

A.5.2 *Atmospheric Boundary Layer Momentum Balance*

We calculate the integral of the individual terms of the momentum equation Equation (A.2) along the respective ABL height, i.e. $H_0 = 1096$ m in both cases. We take the zonal mean along $-2°$ to $2°$ and plot the individual terms of the momentum balance separately to identify the dominant force balances. Below, in the following three paragraphs, we first examine the force balance for the different wind components within the Zonal Wind Pattern (Figure A.5), then for the Meridional Wind Pattern (Figure A.6), followed by a discussion of commonalities and differences.

The momentum balance for the Zonal Wind Pattern in the western Pacific, MAM, 2020, shown in Figure A.5 based on ICON output, demonstrates that the zonal and meridional momentum are subject to a different balance. We observe a mean wind speed of $5\,\mathrm{m\,s^{-1}}$ for the zonal component of the wind field. The meridional wind speed ($< 1.7\,\mathrm{m\,s^{-1}}$) is about a factor of three smaller. While the

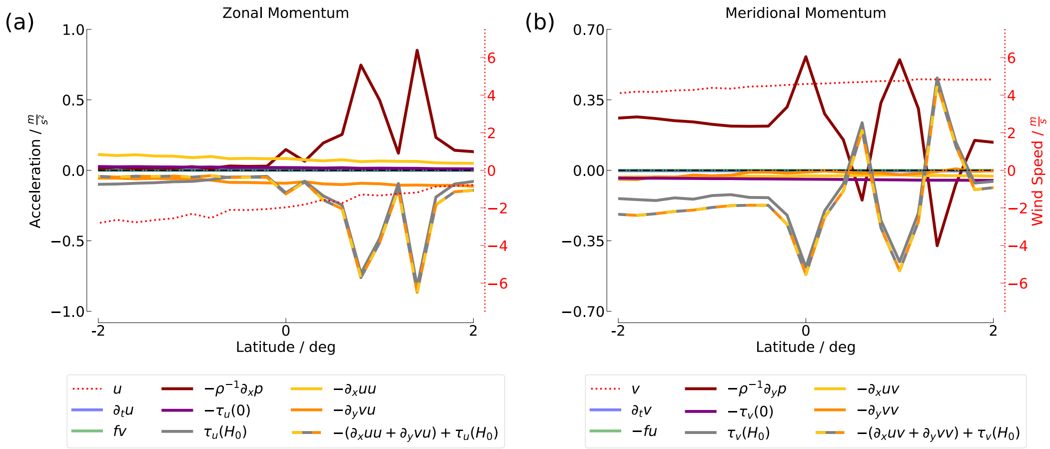

Figure A.6: **Zonal Mean of Momentum Balance, Atlantic, SON, 2020.** Shown are the zonal means of the individual terms of Equation (A.2). The yellow-gray-orange zebra lines represent the sum of the horizontal advection forces and vertical turbulent flux at the top of the ABL. The left and right y-axis show different units: the left, solid y-axis represents the range of values of the solid lines of the momentum terms, the right, dotted y-axis refers to the wind speed of the wind field, which is shown dotted in red.

values of the individual terms of the meridional momentum (b) change sign from southern to northern hemisphere, the values of the zonal momentum (a) retain their sign resulting in the Zonal Wind Pattern on both hemispheres. The zonal, meridional advection of zonal momentum and the zonal vertical turbulent flux at the top of the ABL take the largest values. The zonal pressure gradient force defines the wind direction and accelerates the wind. The horizontal advection forces are in opposition to each other. However, the sum of the horizontal advection forces and the zonal vertical turbulent flux (yellow-gray-orange zebra line) reinforce the pressure gradient force. The zonal surface drag and the meridional advection of zonal momentum oppose the pressure gradient force. The zonal Coriolis force and tendency take very small values and are therefore negligible. The meridional momentum (Figure A.5b) is characterized by larger variations of the individual terms along the latitude. The meridional component of the wind is driven by the vertical turbulent flux on both hemispheres. The pressure gradient force and the sum of horizontal advection forces and meridional vertical turbulent flux (yellow-gray-orange zebra line) have different signs and almost cancel each other out. Unlike for the case of the zonal wind (a), for the meridional wind (b) the pressure gradient is not oriented with the wind, suggesting that in the Zonal Wind Pattern the minor (meridional) component is predominantly arising in response to the vertical turbulent flux. This is consistent with wind jets forming at the top of the ABL (A.3c) for both the zonal and the meridional component.

The momentum balance for the Meridional Wind Pattern in the Atlantic, SON, 2020, shown in Figure A.6 uncovers a different momentum balance for the zonal and meridional component. For both components we obtain variations along latitudes. We observe a mean wind speed of $5\,\mathrm{m\,s^{-1}}$ for the meridional component of the wind field. For the zonal component we only measure mean wind speeds of up to $2\,\mathrm{m\,s^{-1}}$. The meridional momentum (Figure A.6b) of the Meridional

Wind Pattern takes the leading role. The meridional vertical turbulent flux and the meridional pressure gradient at the top of the ABL take the largest values. Here again, meridional Coriolis force and tendency take very small values and are therefore negligible. The meridional component of the wind is accelerated by the meridional pressure gradient force. This driving force is balanced by the meridional vertical turbulent flux, the meridional surface drag and by a slight contribution of the horizontal advection in the leading meridional momentum balance. The meridional vertical turbulent flux, the meridional surface drag and the horizontal advection of meridional momentum tend to slow down the wind. Unlike for the case of the meridional wind (b), for the zonal wind (a) the pressure gradient is not oriented parallel to the wind, suggesting that in the Meridional Wind Pattern the minor (zonal) component is predominantly arising in response to other forces.

Using a momentum analysis, we confirm the expectation that the tendency and the Coriolis terms are negligible throughout our equatorial basins. On the one hand we reveal that the dominant winds for both wind regimes are in the sense of the pressure gradient force while the horizontal and vertical transport terms are of the same order of magnitude. The Zonal Wind Pattern is supported by the zonal vertical turbulent flux and the zonal advection of zonal momentum at the top of the ABL play a key role, emphasizing its importance in the tropical circulation system and the air-sea coupling. On the other hand we show, that transport terms are leading order for the minor winds in both wind regimes. Consistent with what was assumed by Stevens et al. (2002) vertical transport of momentum is important for both wind components, and acts as a good first approximation for the minor winds which are given by the vertical turbulent flux (grey lines in Figure A.5 and Figure A.6).

A.5.3 *The Story of the Zonal Equatorial Surface Winds*

Figure A.7 shows two years of ICON simulation where we observe a seasonality in the Meridional Wind Pattern (b) and almost no seasonality in the Zonal Wind Pattern, which is consistent with the wind patterns shown in Figure A.2. While the Zonal Wind Pattern (a, red dotted line) decreases only slightly during MAM and increases towards JJA and SON, the Meridional Wind Pattern (b, red dotted line) collapses towards MAM and peaks in JJA.

The solid, dark red line represents the pressure gradient force. The pressure gradient force in both wind regimes has the same sign as the actual wind shown in red, dotted. An air parcel is transported in the direction indicated by the sign of the pressure gradient force. Blue dashed lines in Figure A.7 show the evolution of the zonal (a) and meridional (b) SST gradients along the vertical time axis. For both regimes, the SST gradient has the same sign as the pressure gradient force. We therefore deduce from both subplots in Figure A.7 that the pressure gradient force is dominated by the corresponding SST gradient and that the SST-driven pressure gradient force defines the wind direction.

For the Meridional Wind Pattern in the Atlantic in Figure A.7 (green regions in Figure A.2), we observe that if there is no SST gradient such as in MAM 2020 & 2021, we do not observe a pressure gradient force, which can set winds in motion.

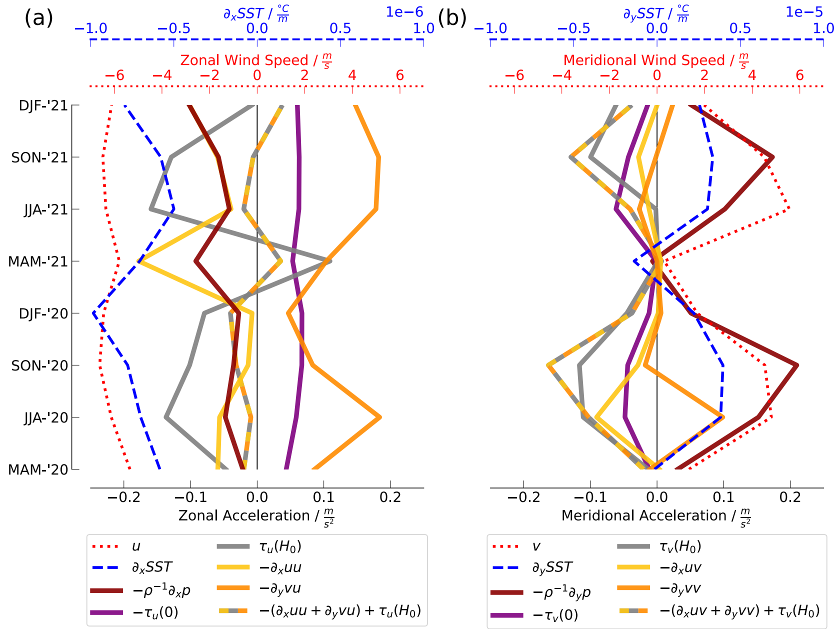

Figure A.7: **Seasonality of the Drivers of the Two Wind Regimes.** Shown are spatial means of the time development along the vertical time axis. Solid lines show the individual terms of the spatial mean of the momentum equation for the leading zonal momentum of the Zonal Wind Pattern (a) dominant in the western Pacific and for the leading meridional momentum of the Meridional Wind Pattern (b) dominant in the Atlantic. The Coriolis force as well as the tendency are not shown, since they are negligible. Dotted lines in red depict the zonal wind component (a) and the meridional wind component (b). Dashed in blue shows the zonal SST gradient (a) and the meridional SST gradient (b). In both wind regimes the SST defines the sign of the pressure gradient force, which sets both wind patterns in motion.

All other forces also come to a standstill. The weak winds are potentially linked to the doldrums that can form near the equator and correlate with the absence of ABL pressure gradients. However, if there is wind, like in all other seasons except during MAM, an existing meridional SST gradient drives the meridional pressure gradient and keeps the Meridional Wind Pattern alive. The meridional vertical turbulent flux, the meridional surface drag and the zonal advection of meridional momentum try to slow down the northward winds. The vertical wind profile of the meridional wind in Figure A.3d shows a wall-jet-like wind within the ABL. Above the ABL, in the free troposphere we observe weaker meridional winds, which support the decelerating effect of the vertical turbulent flux onto the ABL winds. The Meridional Wind Pattern is mainly driven by the meridional pressure gradient force and opposed by the vertical turbulent flux. The ABL seems to disconnect from the momentum of the free troposphere resulting in a surface amplified Meridional Wind Pattern.

For the trade-wind-like Zonal Wind Pattern in Figure A.7 (purple regions in Figure A.2) we note, the zonal vertical turbulent flux and the zonal advection of zonal momentum help to support the zonal pressure gradient force (except for MAM, 2021) by balancing the meridional advection of zonal momentum and the

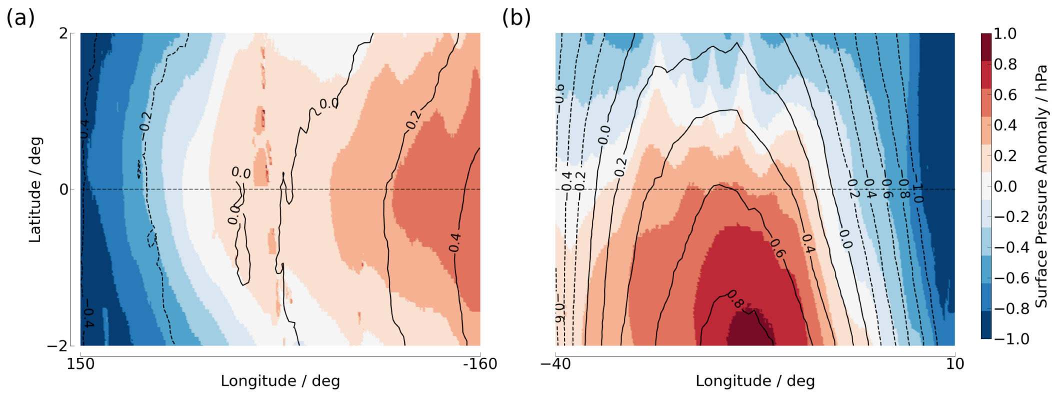

Figure A.8: **Surface Pressure Anomalies.** Shown are the surface pressure anomalies for the western Pacific, MAM, 2020 (a) and the Atlantic, SON, 2020 (b). Displayed are the hydrostatic surface pressure derived from the underlying SST distribution (color coded) and the hydrostatic surface pressure calculated by integration along the vertical density column using the three-dimensional ICON output (contour lines). For the anomaly, we subtract the spatial mean from each value in space for the two compared hydrostatic surface pressure values individually.

surface drag. The vertical wind profile of the zonal wind in Figure A.3c shows a wind profile strongest just aloft the ABL suggesting that the pressure gradients reach deeper into the troposphere. The Zonal Wind Pattern is mainly driven by the zonal pressure gradient and the vertical turbulent flux. The strong winds in the free troposphere increase the momentum accelerating the winds within the ABL via the vertical turbulent flux resulting in an upward amplified Zonal Wind Pattern.

A.6 FROM SEA SURFACE TEMPERATURE TO SURFACE PRESSURE

How much can we learn about the winds by just knowing the SST? To answer this, we adapt the LN paradigm for the ABL pressure and study the influence of the SST on the surface winds. On the one hand, the equatorial zonal surface winds drive the equatorial upwelling and influence the SST (Wyrtki, 1981; Xie and Hsieh, 1995). On the other hand, the SST affects the surface pressure distribution and the pressure gradient force is a substantial component of the driving forces of the surface wind. Therefore, the relationship between SST and the surface winds is close and we establish a model to test how well we can predict the surface winds based on the SST distribution and its spatial variability.

We design a vertical temperature profile starting from the SST. We correct the SST by 0.5 K to compensate for the offset to the surface air temperature (Stevens et al., 2021) and select a dry adiabatic lapse rate for the vertical temperature profile, hence:

$$T(x, y, z) = T_{SST}(x, y) - 0.5 - \frac{g}{c_p} z \tag{A.4}$$

With Equation (A.4) we realize a temperature profile, which guarantees the influence of the SST on the ABL and neglect influences from the overlying free troposphere. We insert this vertical temperature profile into the hydrostatic equation, which we have rewritten using the ideal gas equation and obtain the following differential equation for the pressure p:

$$\frac{dp}{dz} = -\frac{g}{R(x,y,z)} \frac{p(z)}{\left(T_{SST}(x,y) - 0.5 - \frac{g}{c_p} z\right)}, \tag{A.5}$$

with g the gravitational constant, $R(x, y, z)$ the three dimensional profile of the gas constant and $c_p = 1005\,\mathrm{J\,g^{-1}\,K^{-1}}$ (Siebesma et al., 2020). We extract the two-dimensional SST field $T_{SST}(x, y)$ from the ICON output and solve Equation (A.5) by numerical integration from the top of the ABL H_0 to the air-sea interface at $z = 0$ together with the initial value $p_0 = \overline{p}(z = H_0)$, which we also extract from the ICON output.

All together, we obtain the hydrostatic surface pressure based on the influence of the SST spatial variations. Since we take as initial pressure value the spatial mean of the pressure at the top of the ABL from the ICON output, as well as the spatial means of the vertical profile of the water vapor and the vertical temperature profile from the ICON output, we neglect the influence of the overlying free troposphere on the pressure variability within the ABL. Figure A.8 shows the calculated SST-based hydrostatic surface pressure anomaly via Equation (A.5) as color code and the reference hydrostatic surface pressure anomaly calculated by integration along the vertical density column using the three-dimensional ICON output as contour lines.

In Figure A.8a we show the comparison between the hydrostatic surface pressure anomalies underlying the Zonal Wind Pattern. Qualitatively, the shape of the shaded map follows the contour lines with greater agreement in the western than in the eastern ocean basin. Like an arrowhead, higher pressure extends from east to west along the equator and falls off towards higher latitudes. Quantitatively, in the eastern part of the basin, we obtain an overestimation of the meridional pressure gradient for the SST-based hydrostatic surface pressure compared to the meridional pressure gradient based on the three-dimensional ICON density column integration. The anomaly plot indicates that the zonal surface pressure gradient is well reproduced by our ansatz, which is based on the surface pressure reproduction via the SST.

In Figure A.8b we show the comparison between the hydrostatic surface pressure anomalies underlying the Meridional Wind Pattern. Qualitatively, we observe in both surface pressure fields higher pressure south of the equator and lower pressure north of the equator. Quantitatively, the SST-based hydrostatic surface pressure gradient is weaker than the hydrostatic surface pressure based on the vertical density column using the three-dimensional ICON output. The zero line for the SST-based hydrostatic surface pressure anomaly indicated by the white area in the color code is positioned in the center of the box at about 1°N while the density-based hydrostatic surface pressure anomaly from the ICON output shows higher pressure throughout the meridional axis, centered around 15°W.

Comparing the absolute values of the two surface pressure fields, we observe for the western Pacific values that are $0.4 - 0.7\,\mathrm{hPa}$ higher in the surface pressure field, which is based on the SST than in the reference hydrostatic surface pressure computed from the three-dimensional density profile. For the Atlantic we observe values that are $0.3 - 0.8$ hPa higher. The pressure differences possibly result from our ansatz, which is based solely on the influence of the SST on the ABL. The top of the ABL H_0 does not necessarily lie on an isobar, which means that the influence of the free troposphere is actually not negligible. Literature such as Bao et al. (2022) confirms this picture.

A.7 MODELING EQUATORIAL OCEAN WINDS

Having derived the ABL pressure from the SST, we want to find out how much we can link the winds to the SST. In a first step, we extract the Rayleigh Friction Model (RFM) from LN (Equations (4) & (5)) and adapt the wind equations for the horizontal surface winds. It is based on the 3-way model, which combines momentum of Coriolis force, pressure gradient force, surface drag with each other and neglects the contribution from the vertical momentum flux. For the horizontal surface wind equations, the RFM is represented by the zonal and the meridional pressure gradient ($\partial_x p$ & $\partial_y p$) and they follow the equations:

$$\begin{aligned} u_{\mathrm{RFM}} &= \frac{1}{(f^2 + \epsilon_u^2)} \cdot \left(-\epsilon_u \frac{\partial p}{\partial x} - f \frac{\partial p}{\partial y} \right) \cdot \frac{1}{\rho}, \\ v_{\mathrm{RFM}} &= \frac{1}{(f^2 + \epsilon_v^2)} \cdot \left(f \frac{\partial p}{\partial x} - \epsilon_v \frac{\partial p}{\partial y} \right) \cdot \frac{1}{\rho}. \end{aligned} \tag{A.6}$$

Here, $\epsilon_{u,v}^{-1}$ is the apparent damping time scale of the surface winds:

$$\epsilon_u = \frac{C_{d,u}|V_c|}{H_0}, \quad \epsilon_v = \frac{C_{d,v}|V_c|}{H_0}, \tag{A.7}$$

with $|V_c| = 8\,\mathrm{ms}^{-1}$; a constant typical wind speed in the trade cumulus boundary layer, and H_0 the height of the ABL. We derive the exchange coefficient C_d from the zonal and meridional surface drag respectively, since it is not a stored variable of the ICON output. We know that within the model code the surface drag is parameterized via $\tau_u(0) = C_{d,u}|\mathbf{u}|u_{10}$ and $\tau_v(0) = C_{d,v}|\mathbf{u}|v_{10}$, with u_{10} and v_{10} as the 10 m wind speed. By rearranging, we calculate the C_d value for both the zonal and meridional directions and obtain values in the order of 1×10^{-3}.

Figure A.9 shows the zonal mean of the zonal wind u_{RFM} in the western Pacific, MAM, 2020 (a) and the zonal mean of the meridional wind v_{RFM} in the Atlantic, SON, 2020 (b) as a result of the equations shown in (Equation (A.6)). We have applied the zonal RFM to the dominant zonal wind component of the Zonal Wind Pattern in the western Pacific and the meridional RFM to the dominant meridional component of the Meridional Wind Pattern in the Atlantic. If we look at the orange lines in Figure A.9a&b, we see that the magnitude does not match the reference winds. For the Zonal Wind Pattern, the RFM also does not represent the sign correctly. The RFM leaves out leading terms of the momentum balance and the pre-factors to the meridional pressure gradient are not able to scale its influence correctly. Furthermore, the RFM cannot be improved by tuning or rescaling the parameters because they would only change the magnitude but not reconcile the sign differences. Consequently, the existing RFM is not suitable for predicting and monitoring surface winds and their interaction with the sea surface. Thus,

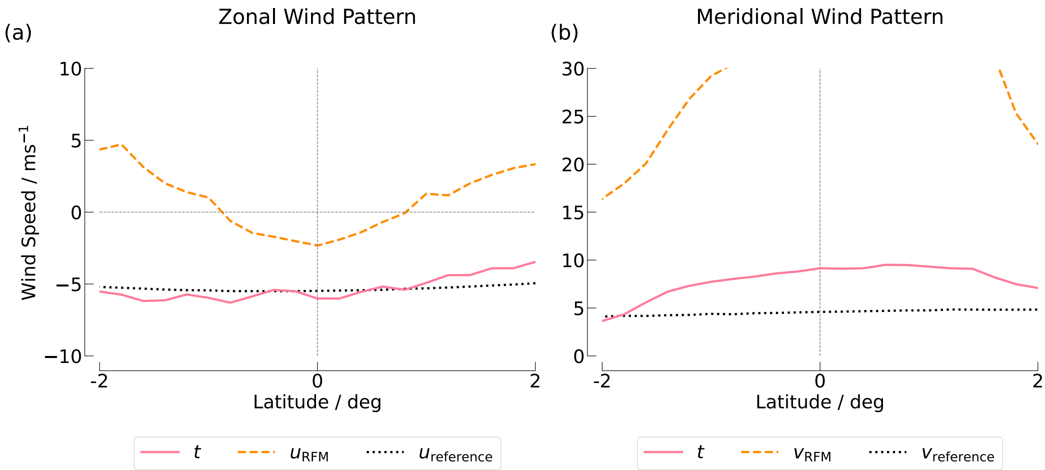

Figure A.9: **Zonal Mean of the Equatorial Wind Patterns.** The zonal winds of the Zonal Wind Pattern in the western Pacific, MAM, 2020 and the meridional winds of the Meridional Wind Pattern in the Atlantic, SON, 2020 are shown. The black dotted lines show the reference winds from the ICON output. The orange dashed lines represent the RFM (Equation (A.6)) and the light red solid line represents the revised model for the tangential velocities (Equation (A.13)). The top of the ABL for (a) is at $H_0 = 1096\,\text{m}$ and for (b) at $H_0 = 1993\,\text{m}$.

we dedicate ourselves to a revised wind model on the basis of our momentum analysis.

A.7.1 *Improving the Equatorial Ocean Wind Model*

We have seen that the conventional RFM is not able to represent the key components of the prevailing equatorial winds in the ICON simulations. The RFM is based on the assumption that the vertical and horizontal transport terms are negligible compared to the other terms of the momentum equation. At the same time, the RFM relies on the Coriolis parameter being able to balance the pressure gradients that are normal to the tangential wind directions. At the equator however, the contribution of the Coriolis parameter is negligible and therefore not able to correct the RFM.

Our analyses show that the equatorial surface winds are composed of a balance between pressure gradient, transport terms (horizontal and vertical) and surface drag what distinguishes us from the RFM that attributes the equatorial wind balance to pressure gradient, Coriolis force and surface drag. The high resolution of our ICON simulations allows us to resolve the near equatorial region well. We learn that vertical and horizontal transport terms are crucial for the surface winds while we confirm with our analyses the small contribution of the Coriolis force and the tendency term to the total equatorial momentum. Therefore, we develop a revised wind model for the leading components of the two equatorial wind patterns and integrate the momentum equations introduced in Section A.5 along the vertical axis through the thickness of the ABL and obtain the vertical turbulent flux $\tau_{U,V}(H_0)$ and the surface drag $\tau_{U,V}(0)$. Note that we choose capital letters for the vertical integral within the ABL:

$$
\begin{aligned}
0 &= -\frac{\partial \overline{UU}}{\partial x} - \frac{\partial \overline{UV}}{\partial y} + \tau_U(H_0) - \tau_U(0) - \frac{1}{\rho}\frac{\partial \overline{P}}{\partial x}, \\
0 &= -\frac{\partial \overline{VU}}{\partial x} - \frac{\partial \overline{VV}}{\partial y} + \tau_V(H_0) - \tau_V(0) - \frac{1}{\rho}\frac{\partial \overline{P}}{\partial y}.
\end{aligned}
\tag{A.8}
$$

Physically, we learn from Figures A.5, A.6 and A.7 that the equatorial ocean surface winds result from a balance between the pressure gradient, the horizontal and vertical advection force such as the surface drag. For our two wind patterns, either the horizontal or the vertical transport term support the pressure gradient force. Hence, we combine the sum of advection forces and the vertical turbulent flux into one transport term $\overline{\mathcal{T}}_{U,V}$ and convert Equation (A.8) to:

$$
\begin{aligned}
\tau_U(0) &= -\overline{\mathcal{T}_U} - \frac{1}{\rho}\frac{\partial \overline{P}}{\partial x}, \\
\tau_V(0) &= -\overline{\mathcal{T}_V} - \frac{1}{\rho}\frac{\partial \overline{P}}{\partial y}.
\end{aligned}
\tag{A.9}
$$

Both wind patterns discussed in section Section A.4 show a leading wind direction, which is driven by the tangential pressure gradient force. From Subsection A.5.2 we learned that the minor wind component which flows along the isobars, is driven by the transport terms. Accordingly, we align the coordinate system along the pressure gradient via the transformation: $x, y, z \mapsto x_t, x_n, z$ where x_t is parallel to the isobars representing the cross-isobaric flow and where x_n runs perpendicular to the isobars. We now distinguish between the flow t, which follows the pressure gradient tangentially, and the flow n, which is normal to the tangential flow. This transformation of the coordinate system causes the pressure gradient parallel to the isobars to vanish, i.e. $\partial_{x_n} p = 0$, resulting in the following relationship:

$$
\begin{aligned}
\tau_t(0) &= -\overline{\mathcal{T}_t} - \frac{1}{\rho}\frac{\partial \overline{P}}{\partial x_t}, \\
\tau_n(0) &= -\overline{\mathcal{T}_n}.
\end{aligned}
\tag{A.10}
$$

Using Equation (A.10), we recognize that the pressure gradient force, which is driving the leading component of the wind field, vanishes for the normal component at the equator. The normal transport terms $\overline{\mathcal{T}_n}$ are responsible for the normal flow, which can be seen from Figure A.5b and Figure A.6a. The tangential flow, however, depends on the tangential transport terms $\overline{\mathcal{T}_t}$ and the tangential pressure gradient $\partial_{x_t}\overline{P}$, which in turn is driven by the SST gradient.

A.7.2 *From Sea Surface Temperature to Ocean Surface Winds*

The leading wind patterns over the equatorial oceans receive their direction and part of their momentum from the pressure gradient force. In Section A.6 we show that the surface pressure can be successfully reproduced by the underlying SST. As an extension, we build on the tangential wind equation (Equation

(A.10)) which includes the transport terms $\overline{\mathcal{T}}$ and investigate how well we can derive the leading wind component from the SST.

We apply a similar parameterization as for $\tau_u(0) = \epsilon_u u$ and $\tau_v(0) = \epsilon_v v$ in the framework of the RFM onto the tangential surface drag, which writes as:

$$\tau_t(0) = \frac{\widehat{C}_d t}{H_0} \cdot t, \tag{A.11}$$

where we take the tangential wind component t for the tangential ϵ_t coefficient instead of $|V_c|$. We have calculated C_d in the RFM from the surface drag, which is related to the 10 m wind speed. However, in Section A.4 and from Figure A.3c, d we have learned that the 10 m wind speed is not representative of the mean ABL wind speed and the exchange coefficient C_d must be corrected in terms of the mean vertical wind profile within the ABL. We therefore scale C_d with the ratio between 10 m wind speed and the vertical mean wind within the ABL and call the rescaled exchange coefficient $\widehat{C}_d$. We plug Equation (A.11) into Equation (A.10) and rewrite the tangential component of Equation (A.10) to:

$$\Leftrightarrow \quad \frac{\widehat{C}_d t}{H_0} \cdot t = -\frac{1}{\rho}\left(\overline{\mathcal{T}_t} + \frac{\partial \overline{P}}{\partial x_t}\right), \tag{A.12}$$

$$\Rightarrow \quad t = \operatorname{sgn}\left(-\frac{\partial \overline{P}}{\partial x_t}\right) \cdot \sqrt{\left|-\eta\left(\overline{\mathcal{T}_t} + \frac{\partial \overline{P}}{\partial x_t}\right)\right|}. \tag{A.13}$$

where $\eta = H_0/\widehat{C}_d \rho$. The radicand is not defined for negative values, so we insert the absolute values. However, this causes the sign to be lost, which defines the wind direction, so we apply the sign function to the pressure gradient force in front of the square root.

We now compare the revised wind model for the tangential wind t (Equation (A.13)) with the RFM (Equation (A.6)) for the Zonal Wind Pattern occurring in the western Pacific and the Meridional Wind Pattern occurring in the Atlantic in Figure A.9. While the RFM disagrees for zonal and meridional wind components at the equator with the ICON reference wind as discussed at the beginning of Section A.7, we obtain greater agreement with the revised tangential wind model. It consistently exhibits the same sign and maps the profile of the zonal and meridional reference winds well. Towards 2° of the Zonal Wind Pattern we observe a slight decrease of wind speed for the revised wind model compared to the reference wind. We also observe a slight shift towards higher wind speeds along the equator for the Meridional Wind Pattern. We attribute these deviations to the SST-based surface pressure field or to the constant ABL height within each basin, neglecting its potential latitude dependence.

At this point, we are not surprised by the differences between the approach via RFM and our revised wind model. The RFM model is fundamentally incapable of representing equatorial winds, as it neglects the transport terms. The RFM incorporates the zonal and meridional pressure gradient force into the zonal and meridional wind equation to compensate for the lack of momentum in the normal wind direction. Furthermore, it overestimates the meridional wind due to the influence of the Coriolis force together with the meridional pressure gradient and underestimates the zonal wind. The Zonal and Meridional Wind Pattern that exist at the equatorial oceans are characterized by a flow, which crosses isobars and does not run parallel to them (c.f. Figure A.3 and Figure A.8). By aligning the coordinate system along the pressure gradient, we learn that the RFM fails to model cross-isobaric winds because Equation (A.6) does not include the vertical and horizontal transport of momentum. However, these transport terms are crucial for the wind fields at the equator. Based on our previous analysis, we can identify the key drivers and determine that within the $-2°$ to $2°$ equatorial window, the Coriolis force has no influence on the surface winds. Therefore, we turn away from the RFM, as its structure cannot be validated by the underlying data. Our revised wind model for the leading tangential wind component is a substantial step forward in the reproduction and understanding of the SST driven surface winds. We obtain a better agreement with the reference winds compared to the RFM both at and off the equator.

A.8 CONCLUSION

We investigate the equatorial ocean surface winds over the western, central, and eastern Pacific, as well as the Atlantic and Indian Ocean using the storm-resolving ICON model. Our analysis focuses on two of these basins, which were selected on the basis of two distinguishable wind patterns: the Zonal Wind Pattern, with a dominant flow parallel to the equator, and the Meridional Wind Pattern, with a dominant flow perpendicular to the equator. In the western and central Pacific, the winds correspond almost exclusively to the Zonal Wind Pattern, which is characterized by upward amplified ABL winds. The free troposphere aloft is faster than the ABL winds and increases the momentum accelerating the winds within the ABL. The eastern Pacific and the eastern Atlantic are subject to the Meridional Wind Pattern all year round. Unlike in the Zonal Wind Pattern, the ABL winds in the Meridional Wind Pattern are surface amplified and the winds in the free troposphere actually oppose the ABL winds. We identify the driving forces of the equatorial winds using a momentum analysis. The high resolution of the model output allows us to resolve the important influence of the horizontal and vertical transport terms, which have been neglected in previous analyses of equatorial winds due to the low resolution of their models.

Surface winds result from the total momentum within the ABL. If we want to understand surface winds on the basis of a momentum analysis, we have to determine the depth of the ABL to perform a momentum analysis along the integral of the ABL. We set the top of the ABL equal to the altitude, at which the vertical exchange of momentum reaches a minimum. The mean ABL height over all oceans and seasons is 800 m with a standard deviation of 340 m which is consistent with observational measurements (Albright et al., 2022; Nuijens et al., 2014). This is much less than the 3000 m assumed by Lindzen and Nigam (1987). They had to assume an about three times higher ABL to obtain appropriate values of the surface wind to compensate for the missing terms of the momentum balance.

We revisit the analysis of the equatorial surface winds on the basis of the 5 km atmosphere-ocean-coupled storm-resolving ICON output. We apply a momentum analysis to the ABL and learn that the transport terms are of leading order in both the leading as well as in the minor wind component of the two wind patterns. Furthermore, we confirm that we can neglect the tendency of the wind and the Coriolis force. For the Zonal Wind Pattern, our analyses show that the zonal and meridional momentum components are subject to different balances. We find that the pressure gradient force and the vertical turbulent flux mainly drive the flow. We learn from the meridional momentum, which dominates the Meridional Wind Pattern that the pressure gradient force drives the wind as well. The minor meridional (zonal) wind component in the Zonal (Meridional) Wind Pattern however, are driven by the transport terms. We conclude that the pressure gradient force is decisive for the surface winds, independent of the wind pattern. However, surface winds are accelerated (decelerated) by the winds aloft of the ABL in the case of the Zonal (Meridional) Wind Pattern communicated by vertical transport of momentum.

We address the question of how strongly the surface pressure is coupled to the SST by following LN. We first assume that the air temperature values at the ocean-air interface are close to the SST. Using the ideal gas equation and the hydrostatic equation, we integrate hydrostatically through the ABL, whose temperature variability is based on the underlying SST variability. We compare the hydrostatic reference surface pressure with the SST-based hydrostatic surface pressure and obtain both qualitative and quantitative good agreement. We note that surface pressure and SST form a close relationship near the equator.

Based on the direct link between surface pressure and SST we design a wind model for the Zonal Wind Pattern and for the Meridional Wind Pattern. Unlike prior studies, which often use a model for the surface wind based on the 3-way balance, we neglect the Coriolis force. Both the role of the vertical turbulent flux and the horizontal advection are neglected in previous works too and therefore are not included in the Rayleigh Friction Model (RFM). The RFM fails to model cross-isobaric winds because it does not include the vertical and horizontal transport of momentum. However, these transport terms are crucial for the cross-isobaric flow. Our revised wind model, however, relies on the findings from the previous momentum analysis. In the leading parts of both wind regimes, the sum of the horizontal advection forces and the vertical turbulent flux are proportional to the pressure gradient force, drive the cross-isobaric flow and are balanced by the surface drag. The revised tangential wind equation incorporates the drivers for the respective wind pattern and shows that the normal component, parallel to the isobars is maintained by horizontal advection forces and the vertical turbulent flux. We establish a relationship, which covers all relevant contributions to the equatorial surface wind regimes and to finally achieve substantial agreement between the revised wind models and the ICON reference winds.

All in all, we find that the direction of the ocean surface winds along the equator is given by the SST gradient and the free tropospheric winds. The zonal and meridional SST gradients are crucial to set the zonal and meridional pressure gradient force in the Zonal Wind Pattern and Meridional Wind Pattern. The vertical transport of momentum supports or opposes the SST driven pressure gradients. The pressure gradient force in turn drives the surface winds in both cases. For the Meridional Wind Pattern, the meridional pressure gradient force drives the flow being counteracted by horizontal advection forces and the vertical turbulent flux. In contrast, the Zonal Wind Pattern exists because momentum from the free troposphere is injected into the ABL by means of vertical turbulent flux. This zonal wind along the equator provides a shallower thermocline in the east compared to the west. Equatorial upwelling is thus favored, which maintains the east-west SST gradient and thus closes the SST-wind-feedback loop.

Our findings could contribute to a corrective mechanism for non-storm-resolving models, in which SST biases in the equatorial cold tongue regions located at the equator are a recurring problem (Misra et al., 2008; Richter and Xie, 2008; Li et al., 2016; Wu et al., 2022). Since we have uncovered how directly SST is coupled to surface winds via surface pressure, it would be conceivable to implement a mechanism that corrects deviations of one of the three variables by a control mechanism over the other two variables. In this way, a continuous local cooling or warming of the SST could be brought back closer to the actual values by a feedback mechanism involving surface wind and surface pressure before it has an impact on the larger scale and fosters the development of biases.

Author Contributions
Marius Winkler: conceptualization, data curation, formal analysis, investigation, methodology, software, validation, visualization, writing – original draft, writing – review and editing. **Tobias Kölling:** data curation, methodology, software. **Juan Pedro Mellado:** conceptualization, investigation, methodology, supervision, validation, writing – review and editing. **Bjorn Stevens:** conceptualization, funding acquisition, investigation, methodology, resources, supervision, validation, writing – review and editing

Acknowledgements
We thank the Max Planck Society, funded predominantly from federal and state sources, for creating a scientific environment in which research at this level can be conducted. We thank the leadership and participation of everyone who brought nextGEMS (https://nextgems-h2020.eu/) & WarmWorld (https://warmworld.de/) to where they are today. Both projects contribute substantially to making coupled storm-resolving global climate simulations usable by a broader scientific community. We would like to thank the German Climate Computing Center DKRZ, on whose supercomputer Levante not only our analyses took place, but also the simulations were generated. We thank Johann Jungclaus for an internal review of the initial manuscript at the Max Planck Institute for Meteorology. In addition, we want to express our gratitude to Raphaela Vogel and Nina Robbins Blanch for many valuable discussions and helpful comments during the early stages of the manuscript.

Conflict of Interest Statement
The authors declare that they have no conflict of interest.

B

ON THE ROLE OF THE SURFACE FLUX PARAMETRIZATION IN TROPICAL CONVECTION UNDER LOW WIND SPEED REGIMES

The work in this appendix is in preparation as:

Winkler, M., Mellado, J.P., Stevens, B. (2024b): "On the Role of the Surface Flux Parametrization in Tropical Convection under Low Wind Speed Regimes", In: *preparation for submission to Geophysical Research Letters*

On the Role of the Surface Flux Parametrization in Tropical Convection under Low Wind Speed Regimes

Marius Winkler[1,2], Juan Pedro Mellado[3], Bjorn Stevens[1]

[1]Max-Planck-Institut für Meteorologie, Hamburg, Germany
[2]International Max Planck Research School on Earth System Modelling, Max-Planck-Institut für Meteorologie, Hamburg, Germany
[3]Universität Hamburg, Meteorologisches Institut, Hamburg, Germany

B.1 abstract

Understanding the driving forces of surface pressure distribution is essential for accurately predicting climate dynamics in tropical regions. Central to this are surface fluxes, which mediate the exchange of momentum, heat, and moisture between the ocean and atmosphere, thereby shaping atmospheric stability, convection, winds, and pressure patterns. However, representing these critical air-sea interactions in global circulation models remains challenging, especially in low wind regimes where high-resolution models struggle with small-scale processes. This study investigates how surface exchange coefficients, specifically the drag coefficient (c_D) and heat exchange coefficient (c_H), influence the pressure distribution and broader atmospheric behavior. By modifying these coefficients a ICON atmosphere-land-only "OptiFlux" setup, we demonstrate how small changes can reinforce convection, enhance surface winds, and align pressure gradients, underscoring the intricate linkage between surface fluxes and large-scale atmospheric dynamics.

plain language summary

Understanding what drives surface pressure patterns is key to accurately predicting climate in tropical areas. At the heart of this are surface fluxes, which control how heat, moisture, and wind are exchanged between the ocean and atmosphere. These exchanges shape the stability of the atmosphere, patterns of convection, wind behavior, and pressure. However, it's challenging to capture these interactions in climate models, especially in low wind areas, where smaller details are difficult to represent. This study looks at how two specific factors—the drag coefficient (c_D) and heat exchange coefficient (c_H)—impact surface pressure and atmospheric behavior. By adjusting these in our ICON "OptiFlux" model, we show that even small tweaks can improve convection, boost surface winds, and better align pressure patterns. These results highlight how surface fluxes play a key role in shaping broader climate dynamics.

keywords

Air-Sea Interaction, Surface Exchange Coefficients, Ocean Surface Winds, Low Wind Speed Regimes, Tropical Convection, Climate Modeling

B.2 INTRODUCTION

Surface pressure gradients shape tropical atmospheric dynamics by controlling the strength and direction of surface winds, which, in turn, influence large-scale circulation patterns. The distribution of surface pressure arises from two primary sources: forces from above, including pressure gradients and temperature variations in the free troposphere, and forces from below, where direct exchanges of momentum, heat, and moisture between the ocean and atmosphere shape the thermodynamic structure of the surface and boundary layer. When variations in surface pressure arise due to conditions aloft—such as changes in tropospheric temperature profiles—these can be indirectly addressed by adjusting surface processes (Bretherton and Smolarkiewicz, 1989). Modifying fluxes at the ocean-atmosphere interface can reshape convection patterns and ultimately influencing pressure distributions across the atmospheric column.

Surface fluxes of momentum, heat, and moisture are therefore crucial in driving air-sea interactions that regulate tropical climate dynamics. In these regions, such interactions are essential for predicting surface winds, convection, and large-scale thermodynamic gradients. However, representing these fluxes accurately in climate models is challenging, particularly under low wind speed conditions (Zeng et al., 2002). Current parameterizations often struggle to capture the small-scale processes at the ocean-atmosphere interface (Kitamura and Ito, 2016; Segura et al., 2024), such as turbulent heat exchanges and momentum transfer, resulting in biases that affect surface pressure gradients, surface winds, and overall atmospheric circulation.

In climate models, surface fluxes—shaping both boundary layer dynamics and large-scale circulation— drive convection, a key process for vertical heat and moisture transport in the atmosphere. Surface winds, driven by sea surface temperature (SST)-induced pressure gradients, are essential components in the climate system (Lindzen and Nigam, 1987; Philander, 1981; Stevens et al., 2002; Winkler et al., 2024, in review), setting up the trade winds and monsoons that fuel global atmospheric circulation (Richter et al., 2014). However, accurately simulating these winds depends on precise surface flux parameterizations. When biases arise in surface wind stress or SST-wind coupling, uncertainties can be introduced into climate models, particularly in the representation of key phenomena like the trade winds and the Intertropical Convergence Zone (ITCZ) (Voldoire et al., 2019; Back and Bretherton, 2009; Xie and Philander, 1994).

To represent surface fluxes in climate models, parameterizations are used to estimate momentum, heat, and moisture exchanges at the ocean-atmosphere interface. Central to these parameterizations are the surface exchange coefficients, such as the drag coefficient c_D and the heat exchange coefficient c_H. Typically derived from Monin-Obukhov similarity theory, these coefficients link turbulent fluxes to the respective mean gradients of wind, temperature, and humidity, while also incorporating atmospheric boundary layer stability. Although widely applied, empirical studies have identified limitations in these parameterizations, especially for accurately capturing small-scale turbulent processes essential to air-sea flux calculations. For example, the Coupled Ocean-Atmosphere Response Experiment COARE3.6 algorithm (Fairall et al., 1996a; Fairall et al., 1996b; Fairall et al., 1997;

Fairall et al., 2003; Fairall et al., 2011; Edson et al., 2013) has highlighted discrepancies in estimating c_D and c_H compared with standard climate model parameterizations.

Despite progress in understanding and improving parameterization techniques, accurately representing surface fluxes in climate models—particularly under low wind speed conditions—remains challenging. Conventional models often overlook multilayered ocean-atmosphere interactions in these low-wind scenarios, leading to biases that propagate through and distort large-scale climate simulations. This study investigates whether increasing the heat exchange coefficient c_H at the surface can effectively enhance atmospheric circulation in tropical regions, specifically by assessing its impact on surface winds, pressure gradients, and overall atmospheric dynamics. Rather than pursuing perfectly tuned parameterizations, this work emphasizes understanding how adjustments in surface fluxes influence the distribution of surface pressure and other atmospheric responses, offering new insights that could improve the accuracy of climate models.

B.3 DATA DESCRIPTION

We analyze simulations from a atmosphere-land-only ICON (ICOsahedral Nonhydrostatic) configuration. The ICON earth-system model, as described by Hohenegger et al. (2023), initially runs on a grid spacing of 10 km with 90 vertical levels in the atmosphere, but in this study we limit the vertical output to 26 levels, focusing on the lower atmosphere. The simulation is started using a prescribed ocean temperature matching Integrated Forecasting System analysis from 01 January 1979, and are run until 31 March 1979. ICON follows the DYAMOND2 protocol (Stevens et al., 2019) as applied during the collaborative European project NextGEMS (Next Generation Earth Modelling Systems, https://nextgems-h2020.eu/).

We compare our results from ICON with ERA5 data (Hersbach et al., 2020) which were provided by the European Centre for Medium-Range Weather Forecasts (ECMWF) and accessed via the Copernicus Climate Change Service (C3S) Climate Data Store. The used ERA5 data comes at a spatial resolution of 0.25° x 0.25°.

We extract from ICON and ERA5 output the pressure, p, the zonal, meridional and vertical wind, u, v and w, the surface drag, $\tau(0)$, the sensible heat, H, the air temperature, T, the air density ρ, and the specific humidity, q. The three-dimensional and two-dimensional fields are available as snapshots with a daily temporal resolution. For the following calculations, we use monthly time averages to conduct our analyses.

B.4 WEAK SURFACE PRESSURE GRADIENTS RESULT IN WEAK SURFACE WINDS

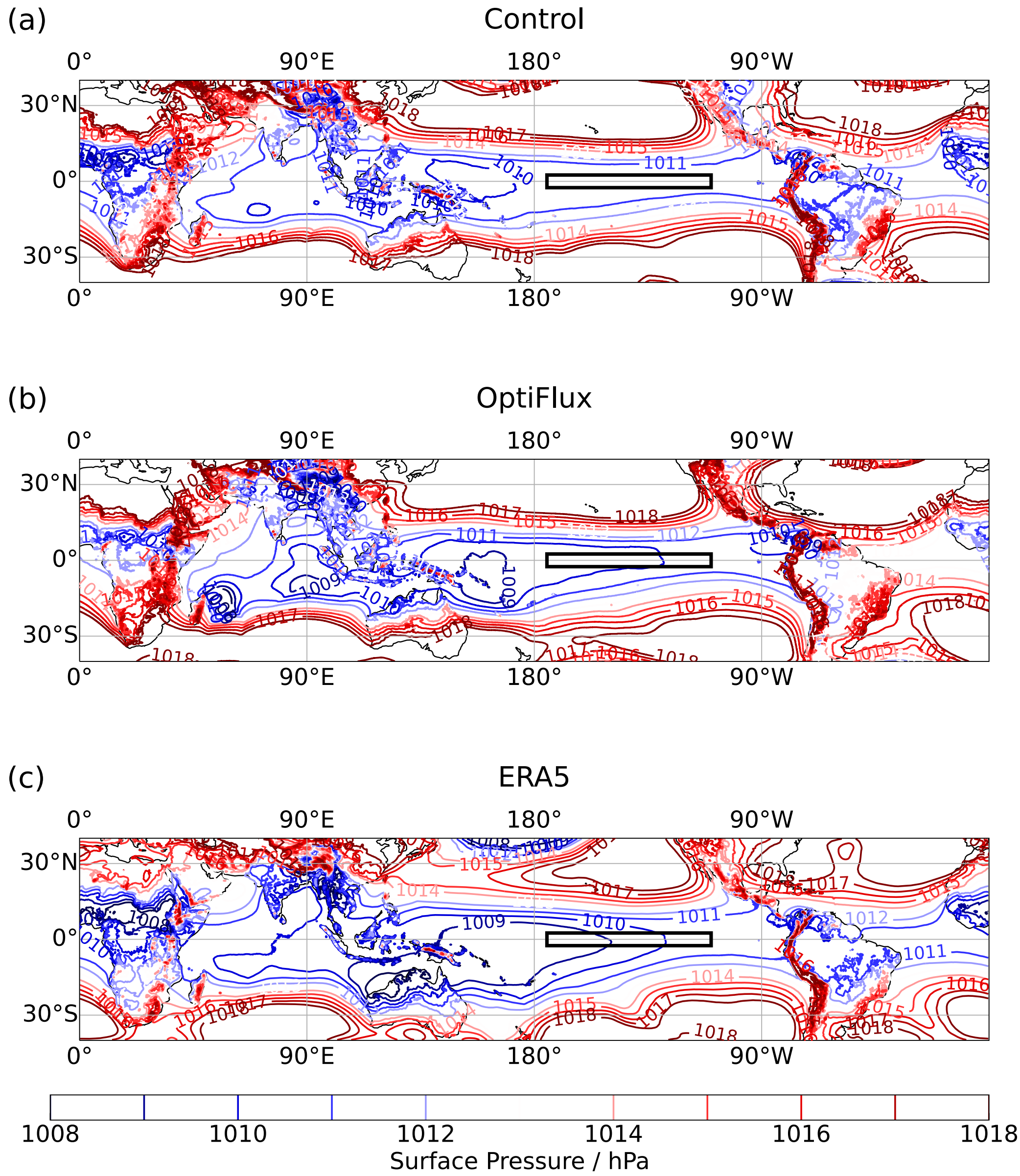

Figure B.1: **Tropical Surface Pressure.** Surface pressure for March 1979 shown as contour lines from the ICON atmosphere-land-only (a) Control simulation, (b) OptiFlux simulation, and (c) ERA5 reanalysis. The black boxes frame a region of interest for further analysis in Figure B.2.

Pressure gradients throughout the entire atmospheric column, particularly in the free troposphere, determine the direction and strength of surface and boundary layer winds, which are key drivers of atmospheric circulation. While SST influences these gradients and therefore the surface winds (Lindzen and Nigam, 1987; Deser, 1993; Stevens et al., 2002), the relationship is multifaceted and not solely defined by SST variations (Winkler et al., 2024, in review). Accurate representa-

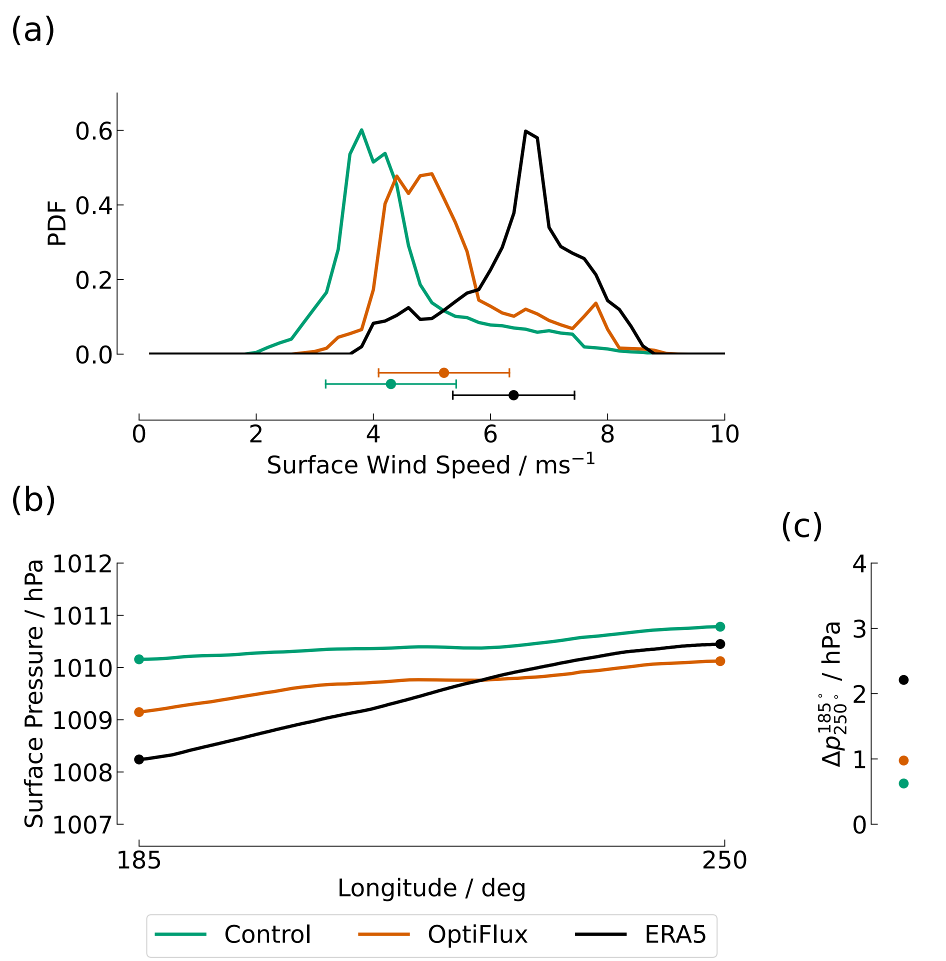

Figure B.2: **Winds, Pressure and Pressure Gradient.** Comparison of Control, OptiFlux, and ERA5 data for (a) PDF of spatial mean surface wind speed together with the mean value and the corresponding standard deviation below each distribution, (b) meridional mean of surface pressure, and (c) zonal pressure gradients along 5°S to 5°N, and 185°E to 250°E indicated by the black box in Figure B.1) for March 1979.

tion of atmospheric pressure gradients is thus vital for capturing the dynamics of wind phenomena (Richter et al., 2014).

Figure B.1 shows the surface pressure as contour lines for March 1979, with an atmosphere-land-only ICON simulation (Control) in panel (a) and the ERA5 reanalysis in panel (c). In both panels, red lines indicate high-pressure areas, while blue lines denote low-pressure regions. At first glance, we notice that both Control and ERA5 show a pressure gradient towards the equator, leading to convergence of the surface winds there. Focusing on the black box in the equatorial Pacific, the atmosphere-land-only simulation Control (a) shows a notably weaker zonal pressure gradient compared to ERA5 (c). For Control (a), the pressure contours are less tightly packed along the equator, indicating a smaller pressure difference across this region. Conversely, ERA5 (c) displays a more pronounced zonal pressure gradient, with closer contour lines suggesting a steeper pressure difference from east to west.

Figure B.2 (a) shows the probability density function (PDF) of the surface wind speed for the area in the equatorial Pacific outlined by the black boxes in Figure B.1. The mean value along with the standard deviation for the corresponding distributions is shown between the plotted distributions and the x-axis. The mean values reveal that the surface wind speed in the Control simulation is approximately $2\,\mathrm{m\,s^{-1}}$ slower than in ERA5, while the standard deviations are comparable, indicating that variability is independent of the ICON simulations or ERA5. Comparing the Control simulation with the ERA5 reanalysis reveals that surface wind speeds below $5\,\mathrm{m\,s^{-1}}$ are more frequent in the Control simulation than in ERA5. The Control simulation exhibits positive skewness, indicating a higher frequency of lower wind speeds with occasional higher values. Conversely, ERA5 is negatively skewed, suggesting that higher wind speeds are more common.

Figure B.2 (b) illustrates the surface pressure profiles along the equatorial Pacific outlined by the black box in Figure B.1 comparing the atmosphere-land-only simulations with ERA5 reanalysis. While the Control simulation shows higher pressure along the longitudes compared to ERA5, it also exhibits a weaker gradient. Figure B.2 (c) shows that the zonal pressure gradient in ERA5 is $3.5\times$ larger than in the Control run. Even though Bernoulli's equation is not directly applicable in the turbulent boundary layer, it can still provide a rough estimate of the relationship between pressure and wind speed. Based on this, we would expect ERA5 to have winds that are $1.9\times$ stronger than those in the Control run. In reality, the mean surface wind speed in ERA5 is $1.5\times$ greater than in the Control simulation. Although this observed increase is slightly less than the $1.9\times$ estimate, it still indicates a coherent relationship between differences in surface pressure gradient and wind speed, aligning with general expectations.

Although the atmosphere-land-only simulation Control is run with an idealized SST distribution virtually identical to that of ERA5, we experience large differences in the surface pressure distribution and surface winds. The weak pressure gradient along the equator in the Control run suggests that the simulation may underestimate the strength of the surface winds, as shown in Figure B.2 (a). An underestimation of surface pressure gradients directly correlates with reduced surface wind velocities. Robust zonal pressure gradients contribute to strong easterly trade winds, essential for ocean-atmosphere interactions. Inaccurate representation of these gradients introduces biases in surface wind simulations, ultimately affecting the model's capacity to predict large-scale climate phenomena reliably.

B.5 FACTORS SHAPING THE SURFACE PRESSURE DISTRIBUTION

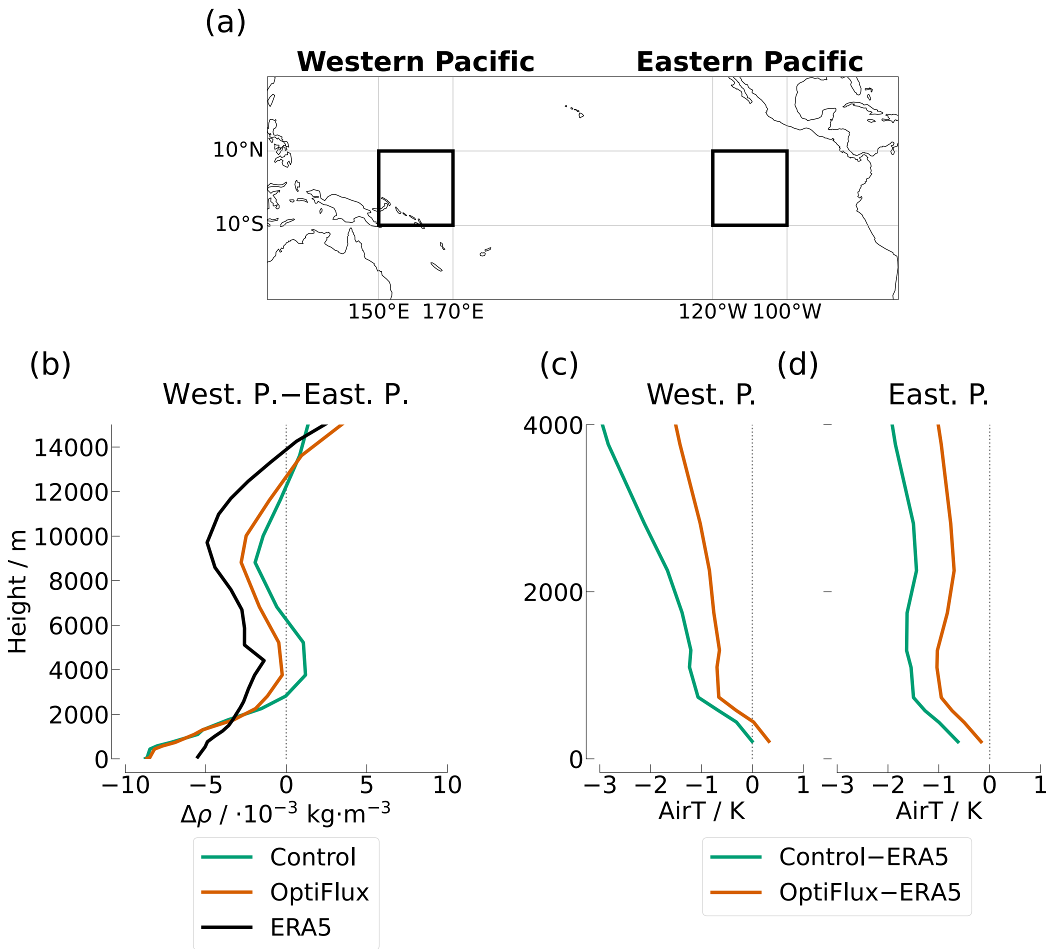

Figure B.3: **Vertical Structure of Density and Temperature.** Comparison of Control, OptiFlux, and ERA5 data for (a) western and eastern Pacific regions, (b) vertical profile showing density differences between the Western and eastern Pacific, and (c) and (d) vertical profiles over the lower 4000 m displaying the differences between Control and OptiFlux relative to ERA5 for the western Pacific (c) and eastern Pacific (d) in March 1979.

In the previous section, we observed that the surface pressure distribution in Control and OptiFlux, despite having an ideal SST distribution, differs from ERA5, especially along the equator. This raises the central question of what shapes these weak zonal pressure gradients in ICON. We propose two hypotheses: first, that weak air-sea coupling in ICON restricts the influence of SST on atmospheric dynamics, thereby limiting the development of SST-driven pressure gradients and resulting in weak surface winds (Lindzen and Nigam, 1987). The second hypothesis is that weak pressure gradients arise from limited convection and weak temperature gradients in the free troposphere, resulting in minimal air movement and a weak surface pressure response.

Figure B.3 compares vertical profiles for the western and eastern Pacific regions outlined in panel (a). Panel (b) shows the vertical density difference between the western and eastern Pacific, giving insight into the altitudes where surface pressure gradients may originate. While ERA5 shows smaller density differences up to around 2000 m, both Control and OptiFlux reveal larger differences in the troposphere above this height. In the boundary layer, Control and OptiFlux exhibit a stronger density difference than ERA5, indicating a substantial SST influence. However, this influence diminishes above approximately 3000 m, suggesting that the density and pressure gradients primarily arise from variations within the lower troposphere and boundary layer.

What explains ICON's greater sensitivity to SST variability compared to ERA5? Are temperatures in ICON warmer over warm oceans (e.g., the western Pacific) and cooler over colder oceans (e.g., the eastern Pacific)? Panels (c) and (d) in Figure B.3 show the difference between ERA5's vertical air temperature profiles and those of Control and OptiFlux from the surface up to 4000 m. Over the western Pacific (panel c), ERA5 shows a warmer temperature profile, while over the eastern Pacific (panel d), Control and OptiFlux are cooler. Though generally colder than ERA5 in both regions, Control and OptiFlux maintain a more pronounced boundary layer density difference below 2000 m.

Our first hypothesis—that weak air-sea coupling in ICON limits the impact of SST variability on pressure gradients—is not supported by these findings, as shown by the density differences in ICON's boundary layer in Figure B.3 (b). SST variations notably influence the boundary layer in both Control and OptiFlux, shaping surface pressure gradients. In contrast, ERA5 shows a more muted SST response in the boundary layer, indicating a weaker direct effect of SST-driven gradients.

The second hypothesis, however, is supported for ERA5 and not for ICON. ERA5, with its convective parameterization, maintains density differences well above the boundary layer deep into the free troposphere, where gravity waves help redistribute mass and energy, enabling a greater zonal pressure gradient at the surface between convective and non-convective areas. In contrast, ICON lacks sufficient convectively driven density differences, restricting such variations to the boundary layer and hindering the development of robust surface pressure gradients which accelerate surface winds poorly.

B.6 IMPROVING THE SURFACE FLUX FORMULATION

To address ICON's limitations in representing convection and accurately capturing surface pressure gradients, we draw on the Wind-Induced Surface Heat Exchange (WISHE) concept introduced by Emanuel (1987). WISHE describes a feedback mechanism in which surface winds enhance atmospheric convection by increasing heat and moisture fluxes at the ocean interface. Faster winds intensify this exchange, fueling deeper convection. This is an elementary feedback cycle for tropical cyclones, but its principles help for improving surface fluxes in ICON, which supply energy to convective processes.

Turbulent processes driven by wind, surface roughness, and temperature and humidity gradients control air-sea interactions at the ocean-atmosphere interface. The surface exchange coefficients, such as the drag coefficient (c_D) for momentum and the heat exchange coefficient (c_H), quantify these exchanges and are fundamental for reliable climate models. These coefficients govern the effectiveness of momentum, heat, and moisture transfer across the interface, impacting atmospheric stability, ocean currents, and energy balances. Typically, parameterizations incorporating these coefficients involve Monin-Obukhov similarity theory, which accounts for boundary layer stability, along with empirical relationships from observational data to capture small-scale turbulent processes within larger-scale models. By enhancing surface fluxes, we enable additional sensible and latent heat release, providing the necessary energy for convection to develop and sustain.

The subroutine `sfc_exchange_coefficients`, a component of the turbulent mixing scheme in ICON, calculates the surface exchange coefficients for momentum (c_D) and heat (c_H). The inputs to this subroutine include height, potential temperature, specific humidity at both the surface and the first model level, mean wind speed, and roughness length for momentum. The outputs are c_D, c_H, and their neutral values, which are not relevant here. Given the challenges climate models encounter in accurately representing surface fluxes under low-wind conditions, a low-wind threshold filter is applied: for wind speeds below $1\,\mathrm{m\,s^{-1}}$, a minimum wind speed of $1\,\mathrm{m\,s^{-1}}$ is assumed. Initially, the subroutine adjusts wind speed and roughness length, then estimates the Richardson number to generate initial guesses for the coefficients using stability functions. It iteratively refines these estimates by recalculating local fluxes of sensible and latent heat, buoyancy flux, friction velocity, and the Obukhov length, adjusting the coefficients based on stability corrections for momentum and heat. This iterative process ensures that c_D and c_H, which are interdependent, converge to stable values. The subroutine then sets the output variables, providing exchange coefficients that reflect atmospheric stability and surface roughness.

The mean wind input to the `sfc_exchange_coefficients` subroutine (Appendix B.11) influences both c_D and c_H. Within this framework, we identify two primary ways to adjust surface wind speed using these exchange coefficients: first, by modifying the drag coefficient (c_D), which directly impacts surface wind speed by altering surface drag at the ocean-atmosphere interface; and second, by changing the heat exchange coefficient (c_H), which affects atmospheric stability and can initiate convection. Adjusting c_H acts at the surface but is hypothesized to influence the entire vertical column by modifying convective heating. Through gravity waves, convection affects temperature profiles throughout the troposphere, ultimately initiating circulation that enhances surface winds by transferring momentum from the descending branch. Given the weak distribution of thermodynamic variables, such as pressure gradients observed in Section B.4, we hypothesize that an overly low heat exchange coefficient c_H restricts effective heat transfer between the ocean and atmosphere, making c_H the primary focus of our adjustments.

These considerations lead us to an experiment in which we increase c_H while keeping c_D unchanged. We modify the `sfc_exchange_coefficients` subroutine in ICON so that c_H, at the end of the subroutine, is uniformly increased up to three times its original value for wind speeds below $6\,\mathrm{m\,s^{-1}}$. To achieve this, we use a scaling function (`m_function` in Appendix B.10) that scales c_H, applying a factor close to 1 for wind speeds just below $6\,\mathrm{m\,s^{-1}}$ and up to 3 as wind speed decreases further. This scaling ensures a smooth transition in c_H as wind speeds

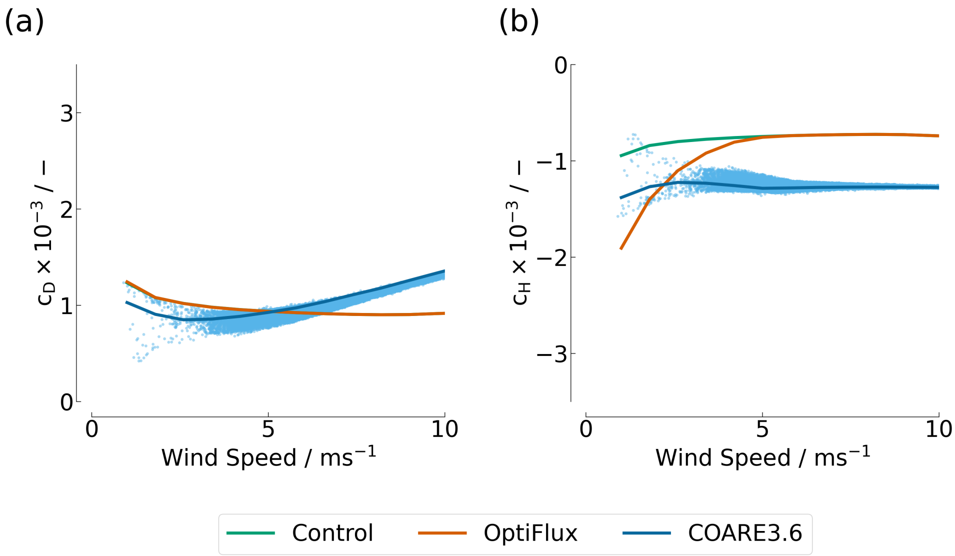

Figure B.4: **Momentum and Heat Exchange Coefficients.** Comparison of drag exchange coefficient c_D in panel (a) and heat exchange coefficient c_H in panel (b) against wind speed from Control, OptiFlux, and the COARE3.6 algorithm.

move above and below $6\,\mathrm{m\,s^{-1}}$. We refer to this modified setup as "OptiFlux" and discuss its effects in the following sections.

Figure B.4 shows the exchange coefficients c_D and c_H as functions of wind speed, comparing the Control and OptiFlux simulations with the COARE3.6 algorithm, developed by Fairall et al. (1996a), Fairall et al. (1996b), Fairall et al. (1997), Fairall et al. (2003), and Fairall et al. (2011) and Edson et al. (2013) based on the TOGA-COARE field program in the western Pacific warm pool (Webster and Lukas, 1992). COARE3.6 (NOAA-PSL, 2022) provides momentum, sensible heat, and latent heat flux estimates using inputs like wind speed, SST, air temperature, and humidity.

We selected a region over the tropical Pacific Ocean for all three data sources. For the ICON atmosphere-land-only simulations, Control and OptiFlux, we back-calculated c_D from wind stress τ and c_H from sensible heat flux H. For the COARE3.6 algorithm, we generated input data based on ICON output from the same region and processed it through the algorithm, obtaining estimates that show what ICON would produce using the COARE3.6 algorithm. We filtered all data sources for unstable conditions, selecting values where surface temperature is $0.2\,°\mathrm{C}$ to $1.0\,°\mathrm{C}$ warmer than the first atmospheric model level temperature. This filter yielded c_D and c_H values as scatter points, exemplified by blue dots for COARE3.6 in Figure B.4. Binning these values produced smooth functions, represented by lines.

In Figure B.4 (a), the blue line shows c_D as a function of wind speed for COARE3.6, with the OptiFlux and Control simulations nearly overlapping (orange and green lines, respectively). The COARE3.6 line shows that c_D increases with wind speed, reaching a minimum at around $3\,\mathrm{m\,s^{-1}}$ before rising again at lower speeds. In contrast, OptiFlux and Control exhibit an almost constant c_D with increasing wind speed, with larger values only at very low speeds. Compared to

COARE3.6, c_D for Control and OptiFlux is approximately $1.17\times$ higher at wind speeds below $5\,\mathrm{m\,s^{-1}}$ and $0.67\times$ lower at higher speeds.

Panel (b) in Figure B.4 shows c_H as a function of wind speed, where COARE3.6, displayed in blue, has higher c_H values across all wind speeds compared to ICON. OptiFlux surpasses Control in c_H values only for wind speeds below $6\,\mathrm{m\,s^{-1}}$, enhancing heat exchange under low-wind conditions. The Control simulation reveals a rather flat and low profile for c_H highlighting the weaker surface fluxes in ICON compared to COARE3.6. The more pronounced discrepancy between ICON's c_H and COARE3.6 validates our decision to focus on c_H over c_D.

While the `sfc_exchange_coefficients` subroutine's calculation of c_D remains unchanged, ICON's c_D values do not match those from COARE3.6. However, the discrepancy in c_H indicates that ICON underestimates heat exchange at all wind speeds. With OptiFlux, we partially correct for this by enhancing heat exchange, especially under low-wind conditions that frequently occur over the Pacific warm pool. Our objective is not to exactly replicate COARE3.6 but to demonstrate the tight connection between small-scale surface flux parameterizations and large-scale atmospheric dynamics.

B.7 POSITIVE EFFECT ON SURFACE WINDS AND PRESSURE GRADIENT

The orange lines in all subplots in Figure B.2 compares the setup with the changes in the subroutine `sfc_exchange_coefficients` called OptiFlux, with the Control simulation and ERA5. In panel (a) we can see that the distribution of the surface wind has shifted towards higher wind speeds. The spatial mean wind of OptiFlux, has almost halved the gap to ERA5 with $6.3\,\mathrm{m\,s^{-1}}$; instead of $4.3\,\mathrm{m\,s^{-1}}$ for Control we observe mean surface winds of $5.2\,\mathrm{m\,s^{-1}}$ for OptiFlux. If we look at panel (b), we notice that the meridional mean of surface pressure has decreased by about 1 hPa along the longitudes. Panel (c) reveals that the pressure gradient between east and west of the respective box has increased, but the difference to ERA5 is still 1.2 hPa. It may seem surprising that such a small increase in the surface pressure gradient has such a large effect on the surface wind. Winkler et al. (2024, in review) demonstrated that surface winds are a result of the surface pressure and the winds aloft, which are themselves driven by pressure gradients in the corresponding atmospheric layer. The acceleration of the surface winds in panel (a) indicates that the modified c_H in OptiFlux has influenced the deeper atmosphere, particularly above the boundary layer.

B.7.1 *Greater Heat Exchange Triggers Convection*

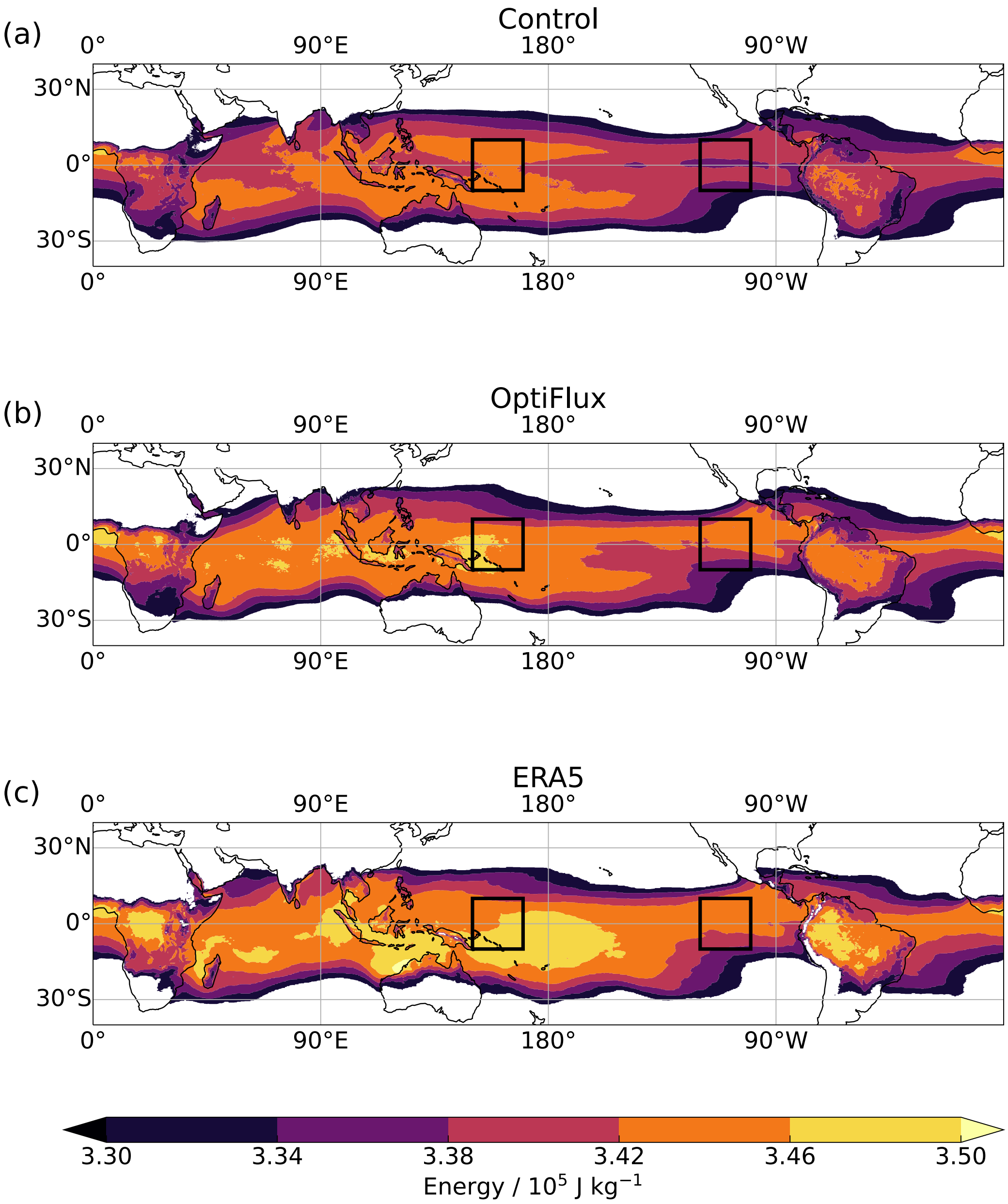

Figure B.5: **Surface Moist Static Energy.** Comparison of the spatial distribution of the moist static energy at the surface of (a) Control, (b) OptiFlux and (c) ERA5 for March 1979. The black boxes frame regions of interest for Figure B.6.

Figure B.4 (b) discloses what the difference is between the two ICON atmosphere-land-only simulations Control and OptiFlux; we get a larger absolute c_H value for winds below $6\,\mathrm{m\,s^{-1}}$. Going back to Figure B.2 (a), we see that the majority of the wind speeds present in the Control run are below the $6\,\mathrm{m\,s^{-1}}$ threshold, which is a first indicator of why the changes in pressure distribution and surface wind speed are so large. Our hypothesis is that the increased heat exchange promotes more convection, which in turn warms the troposphere and strengthens large-scale circulation, ultimately impacting the distribution of surface pressure.

To link surface processes with convective responses, we calculate moist static energy (h):

$$h = c_p T + L_v q + gz, \tag{B.1}$$

where c_p is the heat capacity of dry air, T is temperature, L_v is the latent heat of vaporization, q is specific humidity, g is gravitational acceleration, and z is geometric height.

Figure B.5 shows the spatial distribution of moist static energy at the surface for Control (a), OptiFlux (b), and ERA5 (c). In the Control simulation, values just exceed $3.42 \times 10^5\,\mathrm{J\,kg^{-1}}$ over the Indian Ocean, maritime continents, and the western Pacific, while OptiFlux shows a clear improvement toward ERA5. Despite a remaining difference, the increase in moist static energy across the tropics in OptiFlux, due to the changes in heat exchange (Section B.6), aligns better with ERA5.

The rise in moist static energy in OptiFlux likely results from increased heat transfer between ocean and atmosphere, leading to a shift in the vertical temperature profile and enhancing atmospheric moisture content. High moist static energy at the air-sea interface provides potential energy for convection, driven by warmer, moister air. This is particularly notable in the tropics, especially the western Pacific, where convection becomes more likely.

Figure B.6 displays vertical profiles for the western Pacific (left column) and the eastern Pacific (center column), outlined by the black boxes in Figure B.5. Both regions show an increase in moist static energy throughout the entire vertical profile, from Control to OptiFlux, although ERA5 still exhibits higher values. This increase indicates that the improved heat exchange in OptiFlux influences not only the surface and boundary layer but also extends through the free troposphere to the tropopause, supporting our hypothesis.

Examining the vertical wind speed in Figure B.6 (c) and (d), we observe upward motion in all three simulations in the western Pacific, with ERA5 showing the highest speeds, while OptiFlux diverges from Control above 10 000 m. In the eastern Pacific, the profiles show subsidence (negative values) above 3000 m with upward motion in the lower troposphere. These patterns suggest that increased heat exchange has a moderate effect on vertical wind speeds in OptiFlux.

The zonal wind profiles in Figure B.6 (e) and (f) reveal a layering of easterly winds below approximately 9000 m and westerly winds aloft. In the western Pacific, OptiFlux nearly doubles the zonal wind speed below 7500 m compared to Control, reaching even higher values than ERA5 in the lower troposphere up to about 5000 m. In the eastern Pacific, both OptiFlux and ERA5 show a distinct sign change around 7500 m, while this transition is delayed to higher altitudes in Control, along with a general weakening of zonal wind speed.

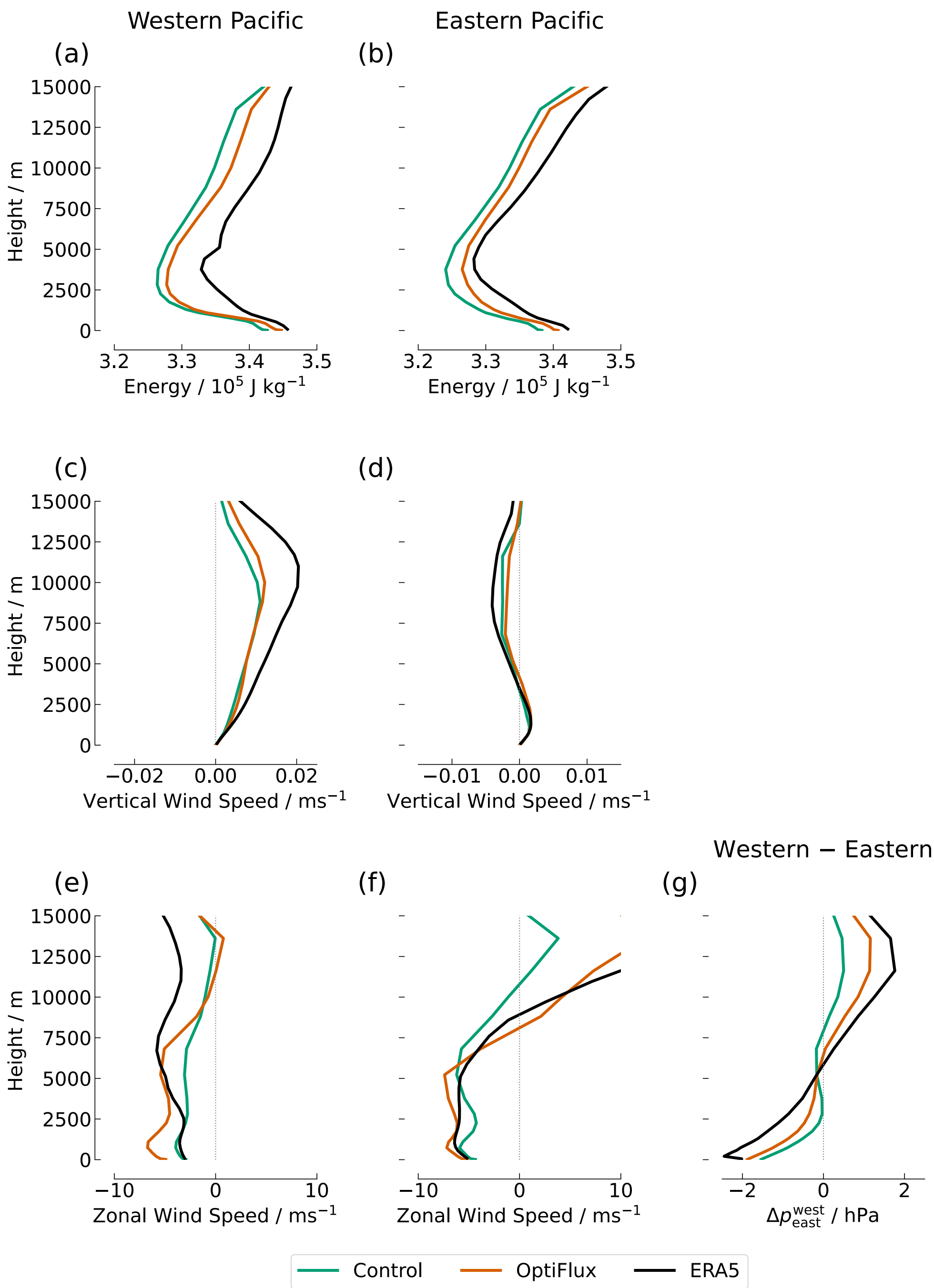

Figure B.6: **Vertical Profiles.** (a) and (b) depict vertical profiles of the moist static energy. (c) and (d) show the vertical wind speed; note the different x axis limits. (e) and (f) indicate the zonal wind speed. (g) the pressure difference between the spatial mean pressure of the western minus eastern Pacific. The left column shows profiles from the western Pacific and the center column from the eastern Pacific outlined by the black boxes in Figure B.5 for March 1979.

Panel (g) in Figure B.6 shows the vertical profile of the spatial mean pressure difference between the western and eastern Pacific boxes. High pressure dominates the eastern Pacific in the lower atmosphere, while high pressure appears over the western Pacific at higher altitudes. The vertical pressure anomaly (Figure B.7) along the longitudes connecting these regions shows a transition: pressure decreases from east to west in the lower troposphere, while increasing from east to west in the upper troposphere. This pattern is most pronounced in ERA5 and is weaker in the Control simulation. These zonal pressure differences drive the zonal wind profiles in (e) and (f), supporting our hypothesis that modifying c_H at the air-sea interface influences the vertical pressure gradient, aligning OptiFlux more closely with ERA5.

B.7.2 *A Conceptual Model: from Small Scale Heat Exchange to Large Scale Motion*

Increasing the heat exchange coefficient c_H has far-reaching effects, influencing the entire vertical temperature profile and triggering convection. Using the warm western Pacific as an example, we observe that the dry adiabatic temperature profile below the lifting condensation level (LCL) shifts toward higher temperatures in OptiFlux, raising the LCL slightly and allowing condensation to occur at a higher altitude. The warmer air parcel in OptiFlux can hold more moisture, making it rise more readily and follow a shifted moist adiabatic temperature profile compared to Control. This increases the contrast with the cooler surrounding environment, enhancing the likelihood of convection in warmer regions.

Once convection is initiated over the western Pacific, large temperature gradients across the tropical troposphere cannot be sustained (Bao et al., 2022). Convection induces gravity waves that propagate horizontally across the tropics, communicating warmer vertical temperature profiles to cooler regions like the eastern Pacific (Bretherton and Smolarkiewicz, 1989; Emanuel et al., 1994). This process creates a dynamic tension: gravity waves drive the temperature profile in the eastern Pacific toward higher values, while the air-sea interface, influenced by the cooler SST, pulls the vertical profile back down. This interaction reinforces or establishes an inversion layer, sustaining an east-west temperature gradient. This temperature gradient induces a corresponding pressure gradient, moving air masses from west to east in the free troposphere, which increases surface pressure in the east, as shown by Figure B.1 (b), Figure B.6 (g), and Figure B.7. Higher surface pressure in the east supports easterly winds in the boundary layer and lower free troposphere, contributing to the surface wind increase observed in Figure B.2 (a).

This process demonstrates how small-scale heat exchange at the ocean-atmosphere interface can set off more vigorous convection and a large-scale overturning circulation in the Pacific. Winds crossing the air-sea interface create friction, facilitating momentum transfer with the ocean through wind stress. Similar to the role of c_H in heat exchange, the momentum exchange coefficient c_D is essential for accurately parameterizing this process. If too much momentum is transferred to the ocean—causing excessive friction and slowing the wind—the reduction in wind speed weakens the calculation of the heat exchange coefficient. The interdependence of c_H and c_D, linked through the Obukhov length (see code in S2, line 51), means that improper calibration, as seen in Control, can disrupt the overturning circulation and reduce surface wind speeds. Our results show that aligning c_H and c_D for improved surface flux calculations, as seen in COARE3.6, strengthens tropical atmospheric dynamics, underscoring the importance of both coefficients in capturing the connection between small-scale surface processes and large-scale motion.

B.8 DISCUSSION AND CONCLUSIONS

This study highlights the effectiveness of surface flux formulation in shaping atmospheric dynamics within tropical climates, especially under low wind speed conditions. By increasing the heat exchange coefficient c_H by 11 % for wind speeds below $6\,\mathrm{m\,s^{-1}}$, we observe a 21 % rise in surface wind speed compared to the Control simulation, driven by an enhanced zonal pressure gradient in the equatorial Pacific vertical column. Although values closer to those of ERA5 have not yet been achieved, it is remarkable to see the improvement by the OptiFlux simulation. Winkler et al. (2024, in review) demonstrated that surface winds are influenced by both the ocean surface and the winds in the free troposphere, with faster (slower) free-tropospheric winds accelerating (decelerating) boundary layer winds through vertical momentum transfer. Our results show that modifications at the air-sea interface have far-reaching effects on the higher atmosphere, altering thermodynamic properties and intensifying deep pressure gradients that are critical for driving surface winds.

The main contribution of this work lies in elucidating the sensitive link between surface fluxes and large-scale atmospheric dynamics, specifically in shaping surface pressure distribution. Our findings confirm that the ICON parameterization underestimates heat exchange in low wind regimes, a recurring issue in climate modeling (Zeng et al., 2002). Additionally, we demonstrate the sensitivity of a storm-resolving model to variations in air-sea heat exchange. In the OptiFlux experiment, the modified surface flux formulation strengthens the coupling between the ocean and atmosphere, facilitating stronger convection that drives changes in the vertical temperature profile. These changes, in turn, intensify pressure gradients throughout the troposphere, directly influencing surface pressure distribution and amplifying winds, particularly in tropical regions. These results advance our understanding of how surface flux processes shape large-scale atmospheric patterns and provide valuable insights into the mechanisms that establish and sustain tropical surface pressure gradients.

Looking ahead, advancing the representation of small-scale processes and integrating comprehensive observational data will be essential as climate models progress toward higher resolutions. Ideally, as models reach finer scales, they may eventually resolve small-scale fluxes, such as those at the air-sea interface, through the model dynamics alone, reducing the reliance on parameterizations. However, if even higher-resolution models still struggle to capture these processes, precise parameterizations will remain important, as these small-scale fluxes can accumulate to become significant driving forces. Refining these aspects is crucial for accurately coupling surface fluxes with larger atmospheric patterns and enhancing the reliability of climate predictions. Future work should prioritize regions like the western Pacific, where strong convection plays a central role, and focus on developing parameterizations that capture the multilayered interactions between the ocean and atmosphere. Addressing these challenges could mitigate persistent biases in tropical climate simulations and deepen our understanding of the processes governing tropical atmospheric dynamics.

Author Contributions

Marius Winkler: conceptualization, data curation, formal analysis, investigation, methodology, software, validation, visualization, writing – original draft, writing – review and editing. **Juan Pedro Mellado:** conceptualization, investigation, methodology, supervision, validation, writing – review and editing. **Bjorn Stevens:** conceptualization, funding acquisition, investigation, methodology, resources, supervision, validation, writing – review and editing

Acknowledgements

We thank the Max Planck Society, funded predominantly from federal and state sources, for creating a scientific environment in which research at this level can be conducted. We thank the leadership and participation of everyone who brought nextGEMS (https://nextgems-h2020.eu/) & WarmWorld (https://warmworld.de/) to where they are today. Both projects contribute substantially to making coupled storm-resolving global climate models usable by a broader scientific community. These simulations were used for the findings on which this paper is based. We would therefore like to thank the German Climate Computing Center DKRZ, on whose supercomputer Levante not only our analyses took place, but also the simulations were generated. We thank Monika Esch for her help in setting up and running the ICON experiments. In addition, we want to express our gratitude to Nina Robbins Blanch and the members of the PrecipPuzzle group for many valuable discussions and helpful comments during the early stages of the manuscript.

Conflict of Interest Statement

The authors declare that they have no conflict of interest.

B.9 Appendix

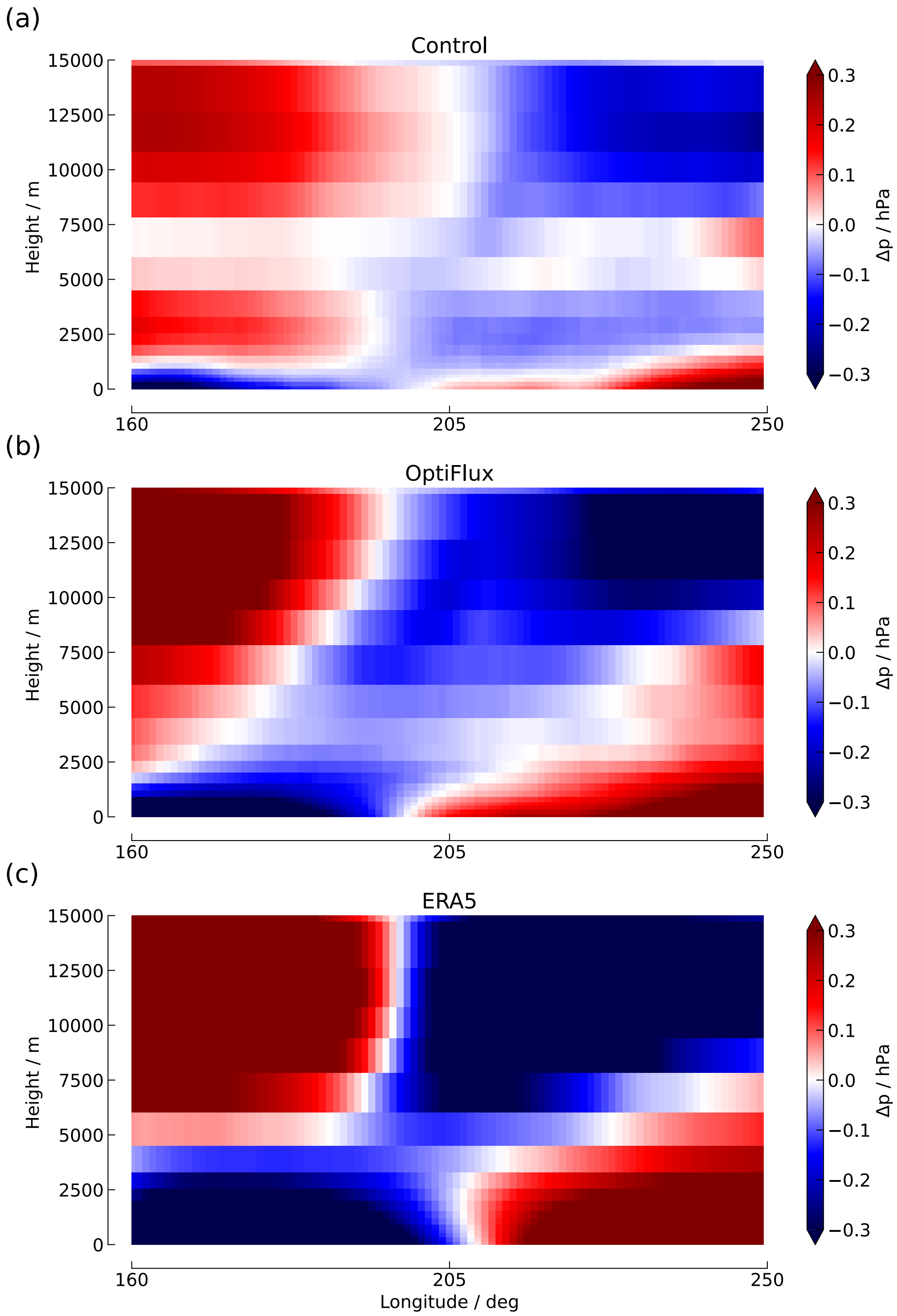

Figure B.7: **Vertical Pressure Anomaly.** The mean of each height level was subtracted from the values along the longitudes at each height level to obtain the anomaly. For the ICON atmosphere-land-only (a) Control simulation, (b) OptiFlux simulation, and (c) ERA5 reanalysis. For March 1979, zonal mean between 5°S to 5°N and stretching from western Pacific box to eastern Pacific box of Figure B.5.

B.10 SCALING FUNCTION

```
PURE FUNCTION m_function(mwind, scaling_factor, threshold_value) RESULT(
    multiplier)
  REAL(wp), INTENT(in) :: mwind, scaling_factor, threshold_value

  REAL(wp) :: multiplier

  IF (0.0_wp <= mwind .AND. mwind <= threshold_value) THEN
    multiplier = 1.0_wp + (scaling_factor - 1.0_wp) * &
                 ((threshold_value - mwind) / threshold_value)**2
  ELSE
    multiplier = 1.0_wp
  END IF

END FUNCTION m_function
```

B.11 SURFACE EXCHANGE COEFFICIENTS

```
PURE SUBROUTINE sfc_exchange_coefficients(                   &
    & dz,                                                   &
    & pqm1, thetam1, mwind, rough_m, theta_sfc, qsat_sfc,   &
    & cD, cH, cD_neutral, cH_neutral                        &
    & )

  REAL(wp), INTENT(in) :: &
    dz,         &
    thetam1,    &
    pqm1,       &
    mwind,      &
    rough_m,    &
    theta_sfc,  &
    qsat_sfc

  REAL(wp), INTENT(out) :: &
    cH,          &
    cD,          &
    cH_neutral,  &
    cD_neutral

  REAL(wp) :: mwind
  REAL(wp) :: rough_m
  REAL(wp) :: z_mc, RIB
  REAL(wp) :: tcn_mom, tcn_heat, shfl_local, lhfl_local
  REAL(wp) :: bflx1, ustar, obukhov_length, inv_bus_mom
  REAL(wp) :: tch
  REAL(wp) :: tcm

  INTEGER  :: itr

  REAL(wp),parameter :: zepsec = 0.028_wp
```

```
  REAL(wp),parameter :: zcons17 = 1._wp / ckap**2

  z_mc = dz
  ! First guess for tch and tcm using bulk approach with adjusted wind
      speeds
  RIB = grav * (thetam1-theta_sfc) * (z_mc-rough_m) / (theta_sfc*mwind**2)
  tcn_mom = (ckap / LOG(z_mc / rough_m))**2
  tcm     = tcn_mom * stability_function_mom(RIB,z_mc/rough_m,tcn_mom)

  tcn_heat = ckap**2 / (LOG(z_mc/rough_m)*LOG(z_mc/rough_m))
  tch      = tcn_heat * stability_function_heat(RIB,z_mc/rough_m,tcn_heat)

  ! Now iterate
  DO itr = 1, 5
    shfl_local = tch * mwind * (theta_sfc - thetam1)
    lhfl_local = tch * mwind * (qsat_sfc - pqm1)
    bflx1 = shfl_local + vtmpc1 * theta_sfc * lhfl_local
    ustar = SQRT(tcm) * mwind

    obukhov_length = -ustar**3 * theta_sfc * rgrav / (ckap * bflx1)

    inv_bus_mom = 1._wp / businger_mom(rough_m,z_mc,obukhov_length)
    tch         = inv_bus_mom / businger_heat(rough_m,z_mc,obukhov_length)
    tcm         = inv_bus_mom * inv_bus_mom
  END DO

  ! Set output variables
  cH  = tch * m_function(mwind, 3.0_wp, 6.0_wp)
  cD  = tcm
  cH_neutral = ckap / MAX(zepsec, SQRT(tcn_heat))
  cD_neutral = ckap / MAX(zepsec, SQRT(tcn_mom))

END SUBROUTINE sfc_exchange_coefficients
```

TOOLS

The work for this dissertation relied on open source software, some of which I would like to acknowledge explicitly:

- Mainly, I employed `Python` (Python Software Foundation, 2020), with extensive use of the `Python`-packages `numpy` (Harris et al., 2020), `xarray` (Hoyer and Hamman, 2017), `cartopy` (Met Office, 2010 - 2015), and `matplotlib` (Hunter, 2007).
- I employed `CDO` (Schulzweida, 2023) to process large amounts of output efficiently, which was especially helpful for working on the ICON native grid.
- This thesis was typeset using the `classicthesis` template developed by André Miede and Ivo Pletikosić (`https://bitbucket.org/amiede/classicthesis/`).
- I used DeepL and ChatGPT (OpenAI, 2021) for translation and refining sentence structures. ChatGPT was not involved in the scientific research presented in this thesis. I did not copy output from ChatGPT, but integrated some of its suggestions into my own writing.

Figures 14 and 15 were created with the help of Yvonne Schrader, MPI-M, based on my conceptualization.

BIBLIOGRAPHY

Albright, Anna Lea et al. (Sept. 2022). "Observed Subcloud-Layer Moisture and Heat Budgets in the Trades." In: *Journal of the Atmospheric Sciences* 79.9, pp. 2363–2385. DOI: 10.1175/JAS-D-21-0337.1.

Albright, Anna Lea et al. (June 2023). "A New Conceptual Picture of the Trade Wind Transition Layer." In: *Journal of the Atmospheric Sciences* 80.6, pp. 1547–1563. DOI: 10.1175/JAS-D-22-0184.1.

Aristotle (350 B.C.E). *Meteorology*. Trans. by E. W. Webster. URL: http://classics.mit.edu/Aristotle/meteorology.html.

Augstein, Ernst, Heiner Schmidt, and Feodor Ostapoff (Mar. 1974). "The vertical structure of the atmospheric planetary boundary layer in undisturbed trade winds over the Atlantic Ocean." In: *Boundary-Layer Meteorology* 6.1, pp. 129–150. DOI: 10.1007/BF00232480.

Augstein, Ernst et al. (Feb. 1973). "Mass and Energy Transports in an Undisturbed Atlantic Trade-Wind Flow." In: *Monthly Weather Review* 101.2, pp. 101–111. DOI: 10.1175/1520-0493(1973)101<0101:MAETIA>2.3.CO;2.

Back, Larissa E. and Christopher S. Bretherton (Aug. 2009). "On the Relationship between SST Gradients, Boundary Layer Winds, and Convergence over the Tropical Oceans." In: *Journal of Climate* 22.15, pp. 4182–4196. DOI: 10.1175/2009JCLI2392.1.

Bao, Jiawei, Vishal Dixit, and Steven C. Sherwood (Nov. 2022). "Zonal Temperature Gradients in the Tropical Free Troposphere." In: *Journal of Climate* 35.24, pp. 7937–7948. DOI: 10.1175/JCLI-D-22-0145.1.

Bjerknes, J. (1966). "A possible response of the atmospheric Hadley circulation to equatorial anomalies of ocean temperature." In: *Tellus* 18.4, pp. 820–829. DOI: 10.1111/j.2153-3490.1966.tb00303.x.

Bourlès, Bernard et al. (Aug. 2008). "THE PIRATA PROGRAM: History, Accomplishments, and Future Directions*." In: *Bulletin of the American Meteorological Society* 89.8, pp. 1111–1126. DOI: 10.1175/2008BAMS2462.1.

Bourlès, Bernard et al. (2019). "PIRATA: A Sustained Observing System for Tropical Atlantic Climate Research and Forecasting." In: *Earth and Space Science* 6.4, pp. 577–616. DOI: 10.1029/2018EA000428.

Bretherton, Christopher S. and Piotr K. Smolarkiewicz (Mar. 1989). "Gravity Waves, Compensating Subsidence and Detrainment around Cumulus Clouds." In: *Journal of the Atmospheric Sciences* 46.6, pp. 740–759. DOI: 10.1175/1520-0469(1989)046<0740:GWCSAD>2.0.CO;2.

Chun, Carl (1902). *Wissenschaftliche Ergebnisse der Deutschen Tiefsee-Expedition auf dem Dampfer "Valdivia" 1898-1899*. Vol. 1. Jena: G. Fischer. URL: https://www.biodiversitylibrary.org/item/18662.

Cromwell, Townsend (Jan. 1953). "Circulation in a meridional plane in the Central Equatorial Pacific." In: *Journal of Marine Research* 12.2. URL: https://elischolar.library.yale.edu/journal_of_marine_research/793.

Deser, Clara (Jan. 1993). "Diagnosis of the Surface Momentum Balance over the Tropical Pacific Ocean." In: *Journal of Climate* 6.1, pp. 64–74. doi: 10.1175/1520-0442(1993)006<0064:DOTSMB>2.0.CO;2.

Edson, James B. et al. (Aug. 2013). "On the Exchange of Momentum over the Open Ocean." In: *Journal of Physical Oceanography* 43.8, pp. 1589–1610. doi: 10.1175/JPO-D-12-0173.1.

Ekman, Vagn Walfrid (1905). "On the influence of the Earth's rotation on ocean-currents." In: *Arkiv för Matematik, Astronomi och Fysik* 2, pp. 1–52.

Emanuel, Kerry A. (Aug. 1987). "An Air-Sea Interaction Model of Intraseasonal Oscillations in the Tropics." In: *Journal of the Atmospheric Sciences* 44.16, pp. 2324–2340. doi: 10.1175/1520-0469(1987)044<2324:AASIMO>2.0.CO;2.

Emanuel, Kerry A., J. David Neelin, and Christopher S. Bretherton (1994). "On large-scale circulations in convecting atmospheres." In: *Quarterly Journal of the Royal Meteorological Society* 120.519, pp. 1111–1143. doi: 10.1002/qj.49712051902.

Fahrbach, E. and E. Bauerfeind (1982). "The variability of equatorial thermocline spreading as an indication of equatorial upwelling in the Atlantic Ocean." In: *Océanographie Tropicale* 17, pp. 121–138. url: https://www.documentation.ird.fr/hor/fdi:02150.

Fairall, C. W. et al. (1996a). "Bulk parameterization of air-sea fluxes for Tropical Ocean-Global Atmosphere Coupled-Ocean Atmosphere Response Experiment." In: *Journal of Geophysical Research: Oceans* 101.C2, pp. 3747–3764. doi: 10.1029/95JC03205.

— (1996b). "Bulk parameterization of air-sea fluxes for Tropical Ocean-Global Atmosphere Coupled-Ocean Atmosphere Response Experiment." In: *Journal of Geophysical Research: Oceans* 101.C2, pp. 3747–3764. doi: 10.1029/95JC03205.

Fairall, C. W. et al. (1996c). "Cool-skin and warm-layer effects on sea surface temperature." In: *Journal of Geophysical Research: Oceans* 101.C1, pp. 1295–1308. doi: 10.1029/95JC03190.

Fairall, C. W. et al. (June 1997). "Integrated Shipboard Measurements of the Marine Boundary Layer." In: *Journal of Atmospheric and Oceanic Technology* 14.3, pp. 338–359. doi: 10.1175/1520-0426(1997)014<0338:ISMOTM>2.0.CO;2.

Fairall, C. W. et al. (Feb. 2003). "Bulk Parameterization of Air–Sea Fluxes: Updates and Verification for the COARE Algorithm." In: *Journal of Climate* 16.4, pp. 571–591. doi: 10.1175/1520-0442(2003)016<0571:BPOASF>2.0.CO;2.

Fairall, C. W. et al. (2011). "Implementation of the Coupled Ocean-Atmosphere Response Experiment flux algorithm with CO2, dimethyl sulfide, and O3." In: *Journal of Geophysical Research: Oceans* 116.C4. doi: 10.1029/2010JC006884.

Ford, Heather L., A. Christina Ravelo, and Steven Hovan (Nov. 2012). "A deep Eastern Equatorial Pacific thermocline during the early Pliocene warm period." In: *Earth and Planetary Science Letters* 355-356, pp. 152–161. doi: 10.1016/j.epsl.2012.08.027.

Halley, Edmond (Sept. 1686). "An historical account of the trade winds, and monsoons, observable in the seas between and near the Tropicks, with an attempt to assign the physical cause of the said winds." In: *Philosophical Transactions of the Royal Society of London* 16.183, pp. 153–168. doi: 10.1098/rstl.1686.0026.

Harris, Charles R. et al. (Sept. 2020). "Array programming with NumPy." In: *Nature* 585.7825, pp. 357–362. doi: 10.1038/s41586-020-2649-2. url: https://doi.org/10.1038/s41586-020-2649-2.

Held, Isaac M. and Arthur Y. Hou (Mar. 1980). "Nonlinear Axially Symmetric Circulations in a Nearly Inviscid Atmosphere." In: *Journal of the Atmospheric Sciences* 37.3, pp. 515–533. doi: 10.1175/1520-0469(1980)037<0515:NASCIA>2.0.CO;2.

Helfer, Kevin C., Louise Nuijens, and Vishal V. Dixit (Apr. 2021). "The role of shallow convection in the momentum budget of the trades from large-eddy-simulation hindcasts." In: *Quarterly Journal of the Royal Meteorological Society* 147.737, pp. 2490–2505. doi: 10.1002/qj.4035.

Hersbach, Hans et al. (2020). "The ERA5 global reanalysis." In: *Quarterly Journal of the Royal Meteorological Society* 146.730, pp. 1999–2049. doi: 10.1002/qj.3803.

Hidaka, Koji (1937). "Equatorial Upwelling and Sinking in a Zonal Ocean with Lateral Mixing." In: *Geophysical Journal International* 4.s1, pp. 359–371. doi: 10.1111/j.1365-246X.1937.tb07125.x.

Hohenegger, Cathy et al. (Jan. 2023). "ICON-Sapphire: simulating the components of the Earth system and their interactions at kilometer and subkilometer scales." In: *Geoscientific Model Development* 16.2, pp. 779–811. doi: 10.5194/gmd-16-779-2023.

Holland, Joshua Z. and Eugene M. Rasmusson (Jan. 1973). "Measurements of the Atmospheric Mass, Energy, and Momentum Budgets Over a 500-Kilometer Square of Tropical Ocean." In: *Monthly Weather Review* 101.1, pp. 44–55. doi: 10.1175/1520-0493(1973)101<0044:MOTAME>2.3.CO;2.

Hou, Arthur Y. and Richard S. Lindzen (July 1992). "The Influence of Concentrated Heating on the Hadley Circulation." In: *Journal of the Atmospheric Sciences* 49.14, pp. 1233–1241. doi: 10.1175/1520-0469(1992)049<1233:TIOCHO>2.0.CO;2.

Hoyer, Stephan and Joe Hamman (Apr. 2017). "xarray: N-D labeled Arrays and Datasets in Python." In: *Journal of Open Research Software*. doi: 10.5334/jors.148.

Hueso, Ricardo et al. (Dec. 2023). "An intense narrow equatorial jet in Jupiter's lower stratosphere observed by JWST." In: *Nature Astronomy* 7.12, pp. 1454–1462. doi: 10.1038/s41550-023-02099-2.

Hunter, J. D. (2007). "Matplotlib: A 2D graphics environment." In: *Computing in Science & Engineering* 9.3, pp. 90–95. doi: 10.1109/MCSE.2007.55.

Kang, Sarah M. et al. (May 2023). "Disentangling the mechanisms of equatorial Pacific climate change." In: *Science Advances* 9.19, eadf5059. doi: 10.1126/sciadv.adf5059.

Kitamura, Yuji and Junshi Ito (Jan. 2016). "Revisiting the Bulk Relation for Heat Flux in the Free Convection Limit." In: *Boundary-Layer Meteorology* 158.1, pp. 93–103. doi: 10.1007/s10546-015-0075-z.

Klocke, Daniel et al. (Dec. 2017). "Rediscovery of the doldrums in storm-resolving simulations over the tropical Atlantic." In: *Nature Geoscience* 10.12, pp. 891–896. doi: 10.1038/s41561-017-0005-4.

Li, Gen et al. (Dec. 2016). "Effects of excessive equatorial cold tongue bias on the projections of tropical Pacific climate change. Part I: the warming pattern in CMIP5 multi-model ensemble." In: *Climate Dynamics* 47.12, pp. 3817–3831. DOI: 10.1007/s00382-016-3043-5.

Lindzen, Richard S. and Sumant Nigam (Sept. 1987). "On the Role of Sea Surface Temperature Gradients in Forcing Low-Level Winds and Convergence in the Tropics." In: *Journal of the Atmospheric Sciences* 44.17, pp. 2418–2436. DOI: 10.1175/1520-0469(1987)044<2418:OTROSS>2.0.CO;2.

Madden, Roland A. and Paul R. Julian (May 1994). "Observations of the 40–50-Day Tropical Oscillation—A Review." In: *Monthly Weather Review* 122.5, pp. 814–837. DOI: 10.1175/1520-0493(1994)122<0814:OOTDTO>2.0.CO;2.

Malkus, Joanne Starr (Aug. 1956). "On the Maintenance of the Trade Winds." In: *Tellus* 8.3, pp. 335–350. DOI: 10.1111/j.2153-3490.1956.tb01231.x.

McPhaden, M. J. et al. (Apr. 2009). "RAMA: The Research Moored Array for African–Asian–Australian Monsoon Analysis and Prediction*." In: *Bulletin of the American Meteorological Society* 90.4, pp. 459–480. DOI: 10.1175/2008BAMS2608.1.

McPhaden, M.J. et al. (Dec. 2010). "The Global Tropical Moored Buoy Array." In: *Proceedings of OceanObs'09: Sustained Ocean Observations and Information for Society*. European Space Agency, pp. 668–682. DOI: 10.5270/OceanObs09.cwp.61.

Met Office (2010 - 2015). *Cartopy: a cartographic python library with a Matplotlib interface*. Exeter, Devon. URL: https://scitools.org.uk/cartopy.

Misra, Vasubandhu et al. (Nov. 2008). "The Equatorial Pacific Cold Tongue Bias in a Coupled Climate Model." In: *Journal of Climate* 21.22, pp. 5852–5869. DOI: 10.1175/2008JCLI2205.1.

Molinari, R. L. et al. (Jan. 1986). "A synthesis of the first GARP Globa Experiment (FGGE) in the equatorial Atlantic Ocean." In: *Progress in Oceanography* 16.2, pp. 91–112. DOI: 10.1016/0079-6611(86)90008-X.

Monin, A.S. and A.M. Obukhov (1954). "Basic laws of turbulent mixing in the surface layer of the atmosphere." In: *Trudy Akademii Nauk SSSR Geophizicheskogo Instituta* 24.151, pp. 163–187.

Neelin, J. David, Isaac M. Held, and Kerry H. Cook (Aug. 1987). "Evaporation-Wind Feedback and Low-Frequency Variability in the Tropical Atmosphere." In: *Journal of the Atmospheric Sciences* 44.16, pp. 2341–2348. DOI: 10.1175/1520-0469(1987)044<2341:EWFALF>2.0.CO;2.

Nitta, Tsuyoshi and Steven Esbensen (Jan. 1974). "Heat and Moisture Budget Analyses Using BOMEX Data." In: *Monthly Weather Review* 102.1, pp. 17–28. DOI: 10.1175/1520-0493(1974)102<0017:HAMBAU>2.0.CO;2.

NOAA-PSL (2022). *COARE-algorithm*. https://github.com/NOAA-PSL/COARE-algorithm.git.

Nuijens, L. et al. (2014). "The distribution and variability of low-level cloud in the North Atlantic trades." In: *Quarterly Journal of the Royal Meteorological Society* 140.684, pp. 2364–2374. DOI: 10.1002/qj.2307.

Nuijens, L. et al. (2022). "The frictional layer in the observed momentum budget of the trades." In: *Quarterly Journal of the Royal Meteorological Society* 148.748, pp. 3343–3365. DOI: 10.1002/qj.4364.

Okumura, Yuko and Shang-Ping Xie (Sept. 2004). "Interaction of the Atlantic Equatorial Cold Tongue and the African Monsoon." In: *Journal of Climate* 17.18, pp. 3589–3602. DOI: 10.1175/1520-0442(2004)017<3589:IOTAEC>2.0.CO;2.

OpenAI (2021). *ChatGPT: A Large-Scale Generative Model for Open-Domain Chat*. Version 3.5. URL: https://github.com/openai/gpt-3.

Philander, S. G. H. (Feb. 1981). "The Response of Equatorial Oceans to a Relaxation of the Trade Winds." In: *Journal of Physical Oceanography* 11.2, pp. 176–189. DOI: 10.1175/1520-0485(1981)011<0176:TROEOT>2.0.CO;2.

Philander, S. G. H. et al. (Dec. 1996). "Why the ITCZ Is Mostly North of the Equator." In: *Journal of Climate* 9.12, pp. 2958–2972. DOI: 10.1175/1520-0442(1996)009<2958:WTIIMN>2.0.CO;2.

Python Software Foundation (2020). *Python*. Version 3.9. URL: python.org.

Randall, David et al. (Nov. 2003). "Breaking the Cloud Parameterization Deadlock." In: *Bulletin of the American Meteorological Society* 84.11, pp. 1547–1564. DOI: 10.1175/BAMS-84-11-1547.

Richter, Ingo and Takeshi Doi (July 2019). "Estimating the Role of SST in Atmospheric Surface Wind Variability over the Tropical Atlantic and Pacific." In: *Journal of Climate* 32.13, pp. 3899–3915. DOI: 10.1175/JCLI-D-18-0468.1.

Richter, Ingo and Shang-Ping Xie (Oct. 2008). "On the origin of equatorial Atlantic biases in coupled general circulation models." In: *Climate Dynamics* 31.5, pp. 587–598. DOI: 10.1007/s00382-008-0364-z.

Richter, Ingo et al. (Dec. 2014). "What controls equatorial Atlantic winds in boreal spring?" In: *Climate Dynamics* 43.11, pp. 3091–3104. DOI: 10.1007/s00382-014-2170-0.

Richter, Ingo et al. (June 2017). "Phase locking of equatorial Atlantic variability through the seasonal migration of the ITCZ." In: *Climate Dynamics* 48.11, pp. 3615–3629. DOI: 10.1007/s00382-016-3289-y.

Riehl, H. et al. (Oct. 1951). "The north-east trade of the Pacific Ocean." In: *Quarterly Journal of the Royal Meteorological Society* 77.334, pp. 598–626. DOI: 10.1002/qj.49707733405.

Riehl, Herbert (1954). *Tropical Meteorology*. New York, NY: McGraw-Hill, p. 392.

Rilke, Rainer Maria (1902). "Herbsttag." In: *Das Buch der Bilder*. Leipzig: Insel Verlag.

Schott, Friedrich A. and Julian P. McCreary (Jan. 2001). "The monsoon circulation of the Indian Ocean." In: *Progress in Oceanography* 51.1, pp. 1–123. DOI: 10.1016/S0079-6611(01)00083-0.

Schulzweida, Uwe (Oct. 19, 2023). "CDO User Guide." In: DOI: 10.5281/zenodo.10020800. (Visited on 03/05/2024).

Seager, Richard et al. (July 2019). "Strengthening tropical Pacific zonal sea surface temperature gradient consistent with rising greenhouse gases." In: *Nature Climate Change* 9.7, pp. 517–522. DOI: 10.1038/s41558-019-0505-x.

Segura, H. et al. (2024). "Global storm-resolving models and the double ITCZ bias: air-surface interaction role for convection in light wind regimes." In: *Journal of Advances in Modeling Earth Systems (JAMES)*. In review.

Siebesma, A. P. (1998). "Shallow Cumulus Convection." In: *Buoyant Convection in Geophysical Flows*. Ed. by E. J. Plate et al. Dordrecht: Springer Netherlands, pp. 441–486. DOI: 10.1007/978-94-011-5058-3_19.

Siebesma, A. Pier et al., eds. (2020). *Clouds and Climate: Climate Science's Greatest Challenge*. Cambridge: Cambridge University Press. DOI: 10.1017/9781107447738. URL: https://www.cambridge.org/core/books/clouds-and-climate/7B47159F7B050B71625111E40795D182.

Stephan, Claudia Christine et al. (Feb. 2021). "Ship- and island-based atmospheric soundings from the 2020 EUREC^{4}A field campaign." In: *Earth System Science Data* 13.2, pp. 491–514. DOI: 10.5194/essd-13-491-2021.

Stevens, Bjorn (May 2005). "ATMOSPHERIC MOIST CONVECTION." In: *Annual Review of Earth and Planetary Sciences* 33.1, pp. 605–643. DOI: 10.1146/annurev.earth.33.092203.122658.

Stevens, Bjorn et al. (July 2001). "Simulations of Trade Wind Cumuli under a Strong Inversion." In: *Journal of the Atmospheric Sciences* 58.14, pp. 1870–1891. DOI: 10.1175/1520-0469(2001)058<1870:SOTWCU>2.0.CO;2.

Stevens, Bjorn et al. (Jan. 2002). "Entrainment, Rayleigh Friction, and Boundary Layer Winds over the Tropical Pacific." In: *Journal of Climate* 15.1, pp. 30–44. DOI: 10.1175/1520-0442(2002)015<0030:ERFABL>2.0.CO;2.

Stevens, Bjorn et al. (May 2016). "The Barbados Cloud Observatory: Anchoring Investigations of Clouds and Circulation on the Edge of the ITCZ." In: *Bulletin of the American Meteorological Society* 97.5, pp. 787–801. DOI: 10.1175/BAMS-D-14-00247.1.

Stevens, Bjorn et al. (Sept. 2019). "DYAMOND: the DYnamics of the Atmospheric general circulation Modeled On Non-hydrostatic Domains." In: *Progress in Earth and Planetary Science* 6.1, p. 61. DOI: 10.1186/s40645-019-0304-z.

Stevens, Bjorn et al. (2020). "The Added Value of Large-eddy and Storm-resolving Models for Simulating Clouds and Precipitation." In: *Journal of the Meteorological Society of Japan. Ser. II* 98.2, pp. 395–435. DOI: 10.2151/jmsj.2020-021.

Stevens, Bjorn et al. (Aug. 2021). "EUREC^{4}A." In: *Earth System Science Data* 13.8, pp. 4067–4119. DOI: 10.5194/essd-13-4067-2021.

Stevens, Bjorn et al. (Apr. 2024). "Earth Virtualization Engines (EVE)." In: *Earth System Science Data* 16.4, pp. 2113–2122. DOI: 10.5194/essd-16-2113-2024.

Voldoire, Aurore et al. (Sept. 2019). "Role of wind stress in driving SST biases in the Tropical Atlantic." In: *Climate Dynamics* 53.5, pp. 3481–3504. DOI: 10.1007/s00382-019-04717-0.

Wallace, J. M., T. P. Mitchell, and C. Deser (1989). "The Influence of Sea-Surface Temperature on Surface Wind in the Eastern Equatorial Pacific: Seasonal and Interannual Variability." In: *Journal of Climate* 2.12, pp. 1492–1499. URL: https://www.jstor.org/stable/26196241.

Wang, Li-Chiao et al. (2017). "Dynamics of upwelling annual cycle in the equatorial Atlantic Ocean." In: *Geophysical Research Letters* 44.8, pp. 3737–3743. DOI: 10.1002/2017GL072588.

Watanabe, Masahiro et al. (June 2024). "Possible shift in controls of the tropical Pacific surface warming pattern." In: *Nature* 630.8016, pp. 315–324. DOI: 10.1038/s41586-024-07452-7.

Webster, Peter J. and Roger Lukas (Sept. 1992). "TOGA COARE: The Coupled Ocean–Atmosphere Response Experiment." In: *Bulletin of the American Meteorological Society* 73.9, pp. 1377–1416. DOI: 10.1175/1520-0477(1992)073<1377:TCTCOR>2.0.CO;2.

Williams, Andrew I. L., Nadir Jeevanjee, and Jonah Bloch-Johnson (2023). "Circus Tents, Convective Thresholds, and the Non-Linear Climate Response to Tropical SSTs." In: *Geophysical Research Letters* 50.6, e2022GL101499. DOI: 10.1029/2022GL101499.

Wills, Robert C. J. et al. (2022). "Systematic Climate Model Biases in the Large-Scale Patterns of Recent Sea-Surface Temperature and Sea-Level Pressure Change." In: *Geophysical Research Letters* 49.17, e2022GL100011. DOI: 10.1029/2022GL100011.

Windmiller, J. M. (2024). "The Calm and Variable Inner Life of the Atlantic Intertropical Convergence Zone: The Relationship Between the Doldrums and Surface Convergence." In: *Geophysical Research Letters* 51.16, e2024GL109460. DOI: 10.1029/2024GL109460.

Windmiller, Julia M. and Bjorn Stevens (2024). "The inner life of the Atlantic Intertropical Convergence Zone." In: *Quarterly Journal of the Royal Meteorological Society* 150.758, pp. 523–543. DOI: 10.1002/qj.4610.

Winkler, Marius et al. (2024, in review). "Uncovering the Drivers of the Equatorial Ocean Surface Winds." en. In: *Quarterly Journal of the Royal Meteorological Society*.

Wu, Xian et al. (June 2022). "The Equatorial Pacific Cold Tongue Bias in CESM1 and Its Influence on ENSO Forecasts." In: *Journal of Climate* 35.11, pp. 3261–3277. DOI: 10.1175/JCLI-D-21-0470.1.

Wyrtki, Klaus (Sept. 1981). "An Estimate of Equatorial Upwelling in the Pacific." In: *Journal of Physical Oceanography* 11.9, pp. 1205–1214. DOI: 10.1175/1520-0485(1981)011<1205:AEOEUI>2.0.CO;2.

Xie, Liusen and William W. Hsieh (Mar. 1995). "The global distribution of wind-induced upwelling." In: *Fisheries Oceanography* 4.1, pp. 52–67. DOI: 10.1111/j.1365-2419.1995.tb00060.x.

Xie, Shang-Ping (2004). "Satellite Observations of Cool Ocean–Atmosphere Interaction." In: *Bulletin of the American Meteorological Society* 85.2, pp. 195–208. URL: https://www.jstor.org/stable/26216942.

Xie, Shang-Ping and S. George H. Philander (Jan. 1994). "A coupled ocean-atmosphere model of relevance to the ITCZ in the eastern Pacific." In: *Tellus A: Dynamic Meteorology and Oceanography* 46.4, pp. 340–350. DOI: 10.3402/tellusa.v46i4.15484.

Yang, Haijun and Fuyao Wang (July 2009). "Revisiting the Thermocline Depth in the Equatorial Pacific." In: *Journal of Climate* 22.13, pp. 3856–3863. DOI: 10.1175/2009JCLI2836.1.

Zebiak, Stephen E. and Mark A. Cane (Oct. 1987). "A Model El Niño–Southern Oscillation." In: *Monthly Weather Review* 115.10, pp. 2262–2278. DOI: 10.1175/1520-0493(1987)115<2262:AMENO>2.0.CO;2.

Zeng, Xubin et al. (Aug. 2002). "Parameterization of Wind Gustiness for the Computation of Ocean Surface Fluxes at Different Spatial Scales." In: *Monthly Weather Review* 130.8, pp. 2125–2133. DOI: 10.1175/1520-0493(2002)130<2125:POWGFT>2.0.CO;2.

EIDESSTATTLICHE VERSICHERUNG | DECLARATION ON OATH

Ich erkläre und versichere hiermit, dass diese Dissertation meine eigene Arbeit ist und dass ich keine anderen als die angegebenen Hilfsmittel und Quellen benutzt habe.

Sofern im Rahmen der Erstellung dieser Dissertation elektronische Ressourcen auf der Basis generativer künstlicher Intelligenz (gKI) genutzt wurden, bestätige ich, dass meine eigene Arbeit der wesentliche und wertschöpfende Beitrag war und dass eine vollständige Dokumentation aller genutzten Ressourcen gemäß guter wissenschaftlicher Praxis vorliegt. Für fehlerhafte oder entstellte Inhalte, falsche Verweise, Verletzungen des Datenschutzes und des Urheberrechts oder Plagiate, die durch die gKI erzeugt wurden, bin ich selbst verantwortlich.

I hereby declare and affirm that this doctoral dissertation is my own work and that I have not used aids and sources other than those indicated.

If electronic resources based on generative artifical intelligence (gAI) were used in the course of writing this dissertation, I confirm that my own work was the main and value-adding contribution and that complete documentation of all resources used is available in accordance with good scientific practice. I am responsible for any erroneous or distorted content, incorrect references, violations of data protection and copyright law or plagiarsim that may have been generated by the gAI.

Hamburg, November 24, 2024

Marius Winkler

ÜBEREINSTIMMUNGSERKLÄRUNG | DECLARATION OF CONFORMITY

Ich versichere, dass dieses gebundene Exemplar der Dissertation und das in elektronischer Form eingereichte Dissertationsexemplar (über den Docata-Upload) und das bei der Fakultät zur Archivierung eingereichte gedruckte gebundene Exemplar der Dissertationsschrift identisch sind.

I, the undersigned, declare that this bound copy of the dissertation and the dissertation submitted in electronic form (via the Docata upload) and the printed bound copy of the dissertation submitted to the faculty (responsible Academic Office or the Doctoral Office Physics) for archiving are identical.

Hamburg, November 24, 2024

Marius Winkler

Hinweis / Reference

Die gesamten Veröffentlichungen in der Publikationsreihe des MPI-M
„Berichte zur Erdsystemforschung / Reports on Earth System Science",
ISSN 1614-1199

sind über die Internetseiten des Max-Planck-Instituts für Meteorologie erhältlich:
https://mpimet.mpg.de/forschung/publikationen

All the publications in the series of the MPI -M
„Berichte zur Erdsystemforschung / Reports on Earth System Science",
ISSN 1614-1199

are available on the website of the Max Planck Institute for Meteorology:
https://mpimet.mpg.de/en/research/publications